ABSTRACT

Title of Dissertation: **NANO STRUCTURED MATERIALS FOR ENERGY APPLICATIONS**

Lu Liu, Doctor of Philosophy, 2017

Dissertation directed by: Michael R. Zachariah, Professor
Department of Chemical and Biomolecular Engineering and Department of Chemistry and Biochemistry

This dissertation addressed the applications of nanostructured materials as oxygen carriers (OCs) and catalysts in poly lactic acid (PLA) thermal decomposition. In chapter 1~4, the stability and cyclibility of metal oxides and supported metal oxides as OCs were evaluated in an isothermal fixed bed reactor at different temperatures for 50 cycles with methane as fuel, up to 15h while their structural, physical and chemical properties were identified using XRD, SEM, TEM, BET, XPS and Ar/H_2-TPR. In chapter 5, aerosol synthesized Bi_2O_3 was found to be a useful catalyst in thermal PLA decomposition, which could lower the on-set decomposition temperature by ~75 T. The developed study protocol could be applied to various metal oxides and polymers to study their catalytic thermal decompositions as well.

NANO STRUCTURED MATERIAL FOR ENERGY APPLICATIONS

by

Lu Liu

Dissertation submitted to the Faculty of the Graduate School of the
University of Maryland, College Park, in partial fulfillment
of the requirements for the degree of
Doctor of Philosophy
2017

Advisory Committee:
Professor Michael R. Zachariah, Chair
Professor Sheryl Ehrman, Dean's representative
Professor Bryan Eichhorn
Professor Zhihong Nie
Professor Efrain Rodriguez

Dedication

To

My parents

Junhui Liu (刘俊辉) and Ping Li（李平）,

And my husband

Peng Zhao （赵鹏）.

Thank you for your unconditional love and support. Thank you for your unwavering faith and absolute belief in my abilities. You have sacrificed so much and waited so long for this moment to come true and I dedicate this dissertation to you.

Acknowledgements

I owe my gratitude to all those who have guided and helped me along this journey.

First and foremost, I would like to express my sincere thanks and respect to my advisor, Professor Michael Zachariah, for guiding me throughout the years of my graduate study, who is the most brilliant person I have met. It is my honor for me to work with him, with his invaluable ideas, experience, eternal passion and rigorous attitude for research and life.

I thank my advisory committees, Professor Efrain Rodriguez, Professor Zhihong Nie, Professor Bryan Eichhorn and Professor Sheryl Ehrman for their time, input and help in reading my dissertation and providing valuable comments. Moreover, I would like to thank Dr. Rodriguez for insightful discussions on my perovskite OC work. I would like to thank Dr. Dongxia Liu for advice and suggestions on the zeolite work. I would like to thank Dr. Stanislav Stoliarov for reading and editing my catalytic Poly Lactic-acid (PLA) thermal decomposition work.

I would like to thank Dr. Xiaofei Ma, who mentored me in my first two years of PhD study. I learned much from his knowledge and experience in combustion and aerosol synthesis & measurement techniques. I would like to thank Yiqing Wu and Dr. Jing Li, with whom I collaborated with zeolite and PLA work respectively. Yiqing did the material synthesis, elemental analysis and BET in zeolite work and Jing finished the kinetic analysis in the PLA work. I learned a lot from them.

Also, I would like to thank all Zachariah group members (Dr. Guoqiang Jian, Dr. Xiaofei Ma, Xizheng Wang, Tao Wu, Dr. Mingdong Li, Dr. Lei Zhou, Dr. Wenbo Zhou, Yong Yang, Rian You, Jiaojie Tan, Philip Guerieri, Jeffery DeLisio, Scott Holdren Garth Egan, Nichloas Piekiel and Rohit Jacob) for their help for make my Ph.D. journey real and enjoyable.

Last but definitely not least, I owe my thanks to my family for all their love and support. I am indebted to my parents for raising me and supporting me in all my pursuits. Most importantly, I am very grateful to my husband, Peng Zhao, for his love and support on my way to finish my Ph.D.

Lu Liu
刘璐

Table of Contents

List of Tables

List of Figures

List of Abbreviations

CLC	Chemical Looping Combustion
OC	Oxygen Carrier
SEM	Scanning Electron Microscopy
TEM	Transmission Electron Microscopy
XRD	X-Ray Diffraction
XPS	X-Ray Photoelectron Spectroscopy
ICP-OES	Coupled Plasma-Optical Emission Spectroscopy
BET	Brunauer, Emmett and Teller Theory
TG	Thermogravimetry
TPR	Temperature Programed Reduction
DTA	Differential Thermal Analysis
DSC	Digital Scanning Calorimetry
DMA	Differential Mobility Analyzer
CPC	Condensation Particle Counter
PLA	Poly Lactic Acid

Chapter 1: Introduction

1.1 Energy utilization and nanostructures

1.1.1 Energy utilization and climate change

Since the industrial revolution two or three hundred years ago, daily life style of human society has been changed in all aspects, including increased amount of food and consumer goods produced, significantly elongated distances travelled, as well as drastically increased human population. All of these aspects are based on the growing energy consumption to maintain the enhanced quality of human life. As shown in Figure 1.1[1], the energy consumption has grown by more than 20 times in the 20th century, which was caused by both the population explosion and the energy consumed per pita.

As indicated by Figure 1.2, which is the energy flow chart in the U. S in 2015, the major energy resources are fossil fuels, including coal, natural gas, petroleum, which cover more than 80% of the total energy resource. Also, combustion is still the major approach for energy conversion, including more than 85% (fossil fuel & biomass) of the total world energy, which is the sum of the 95% in transportation, 67% in electricity generation and approximately 50% in all other sectors.

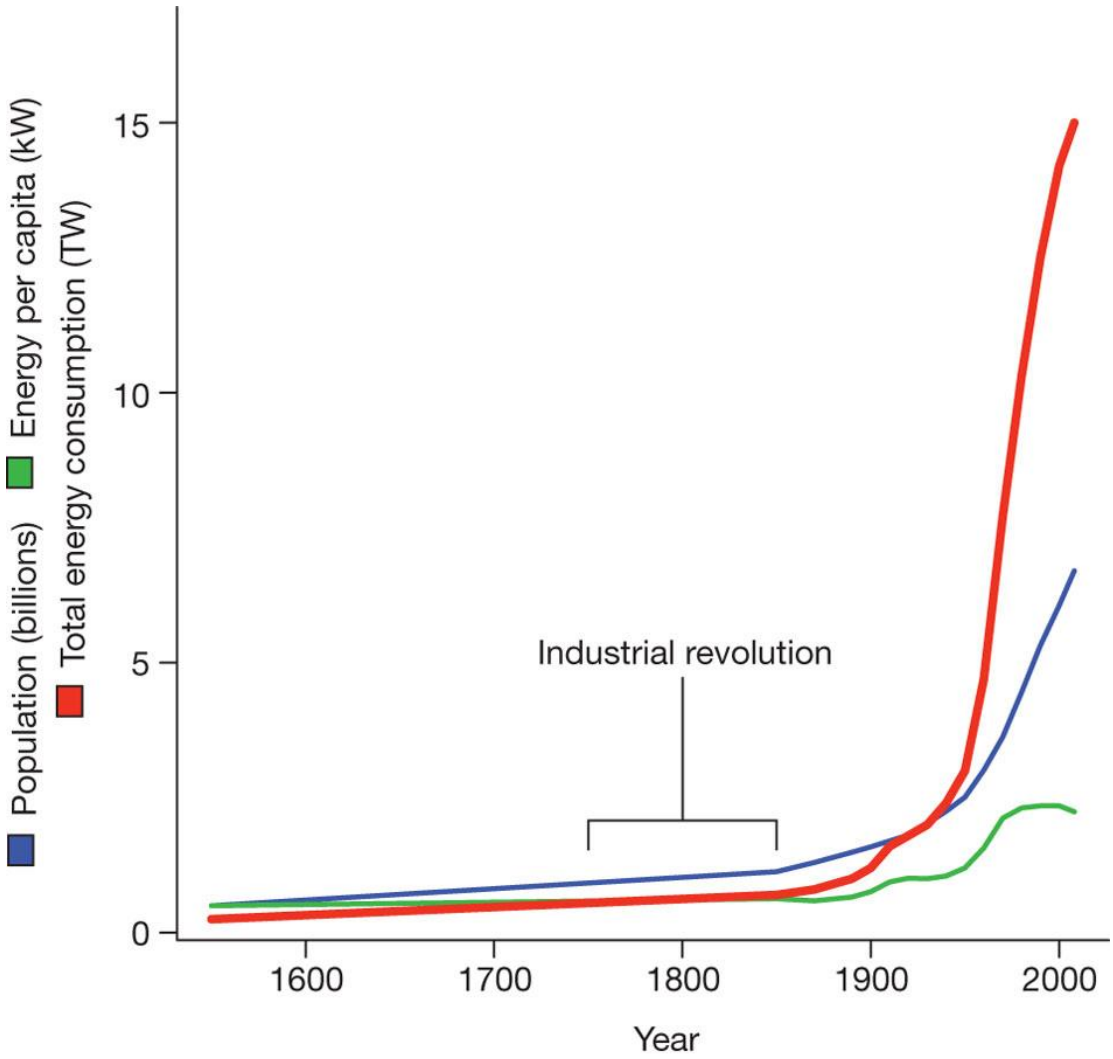

Figure 1.1. History of total and per capita human energy use and world population.

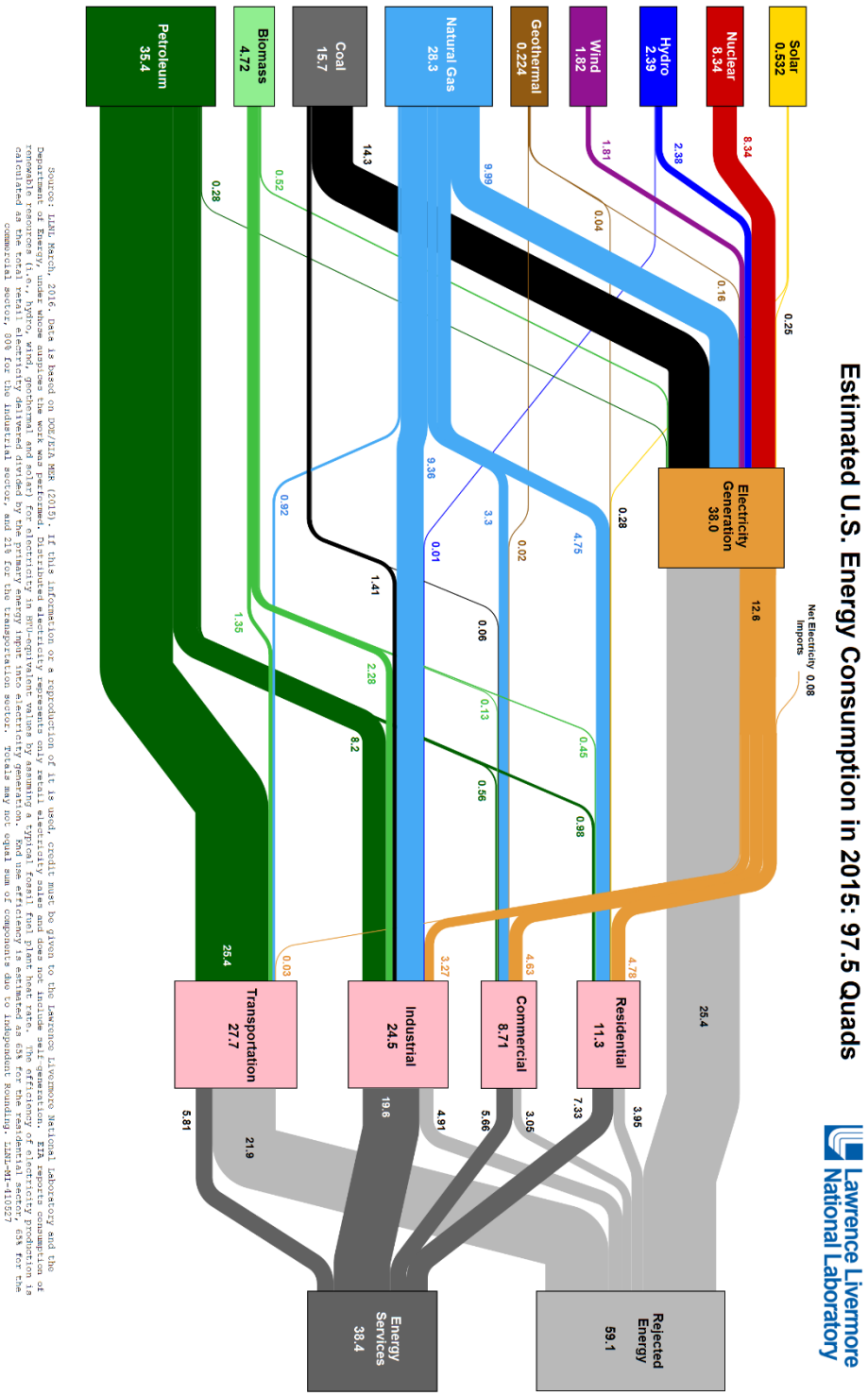

Figure 1.2. Energy flow charts of the relative size of primary energy resources and end uses in the United States in 2015, with fuels compared on a common energy unit basis. The chart is produced by Lawrence Livermore National Lab. (https://flowcharts.llnl.gov/).

Increased energy consumption has been widely acknowledged as the reason for global climate change. The global temperature has increased ~1 ^{o}C in the past one hundred years, which has exceeded the temperature increase in the previous thousands of years, while nationwide temperature is 0.6 ^{o}C higher than the 1981-2010 average, as shown in Figure 1.3. It has been widely acknowledged that CO_2 is the major greenhouse gas, shown in Figure 1.4, accounting for half the greenhouse gas effect, causing global warming.[2] It mainly comes from fossil fuel and biomass combustion, which is the major energy source for modern industries, offering more than 80% of the global energy consumption.[3] Although CO_2 emission also comes from lots of natural sources such as decomposition, ocean release and respiration, a lot of evidence has shown that human related CO_2 emission is the major source of CO_2 increase since industrial revolution, indicated by Figure 1.5.[4]

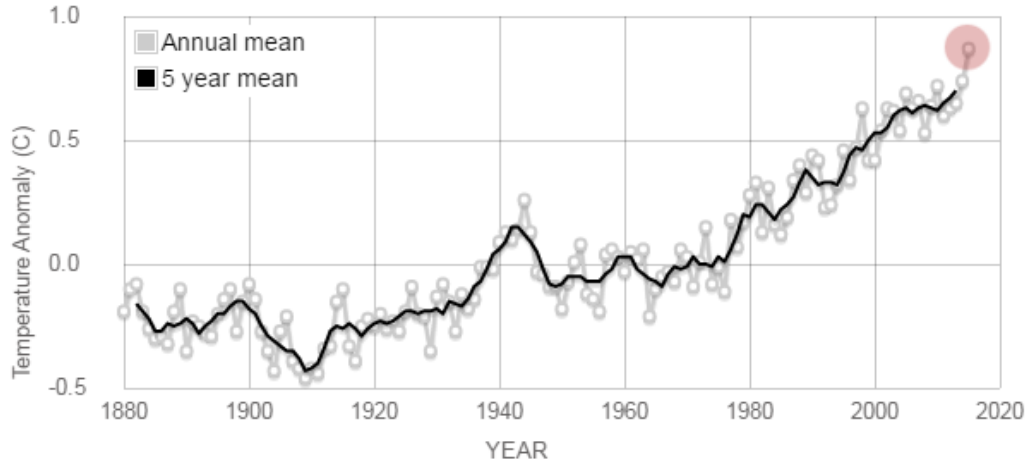

Figure 1.3. Global surface temperature changes from 1880 to 2015, with the year 2015 ranking as the warmest on record (data from NASA/GISS http://climate.nasa.gov/vital-signs/global-temperature/).

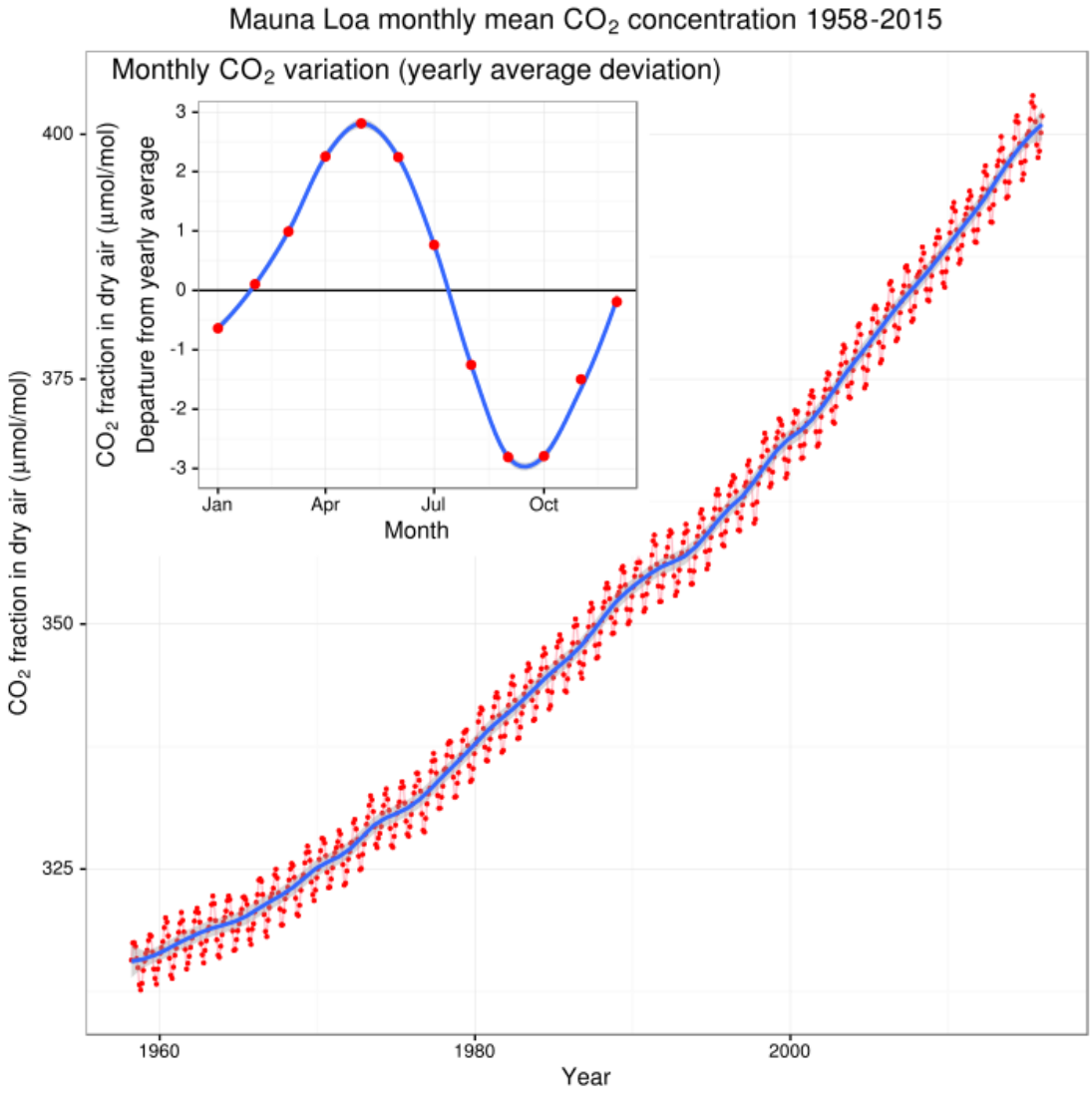

Figure 1.4. Keeling curve of atmospheric carbon dioxide concentration, measured at Mauna Loa Observatory (http://en.wikipedia.org/wiki/Keeling Curve).

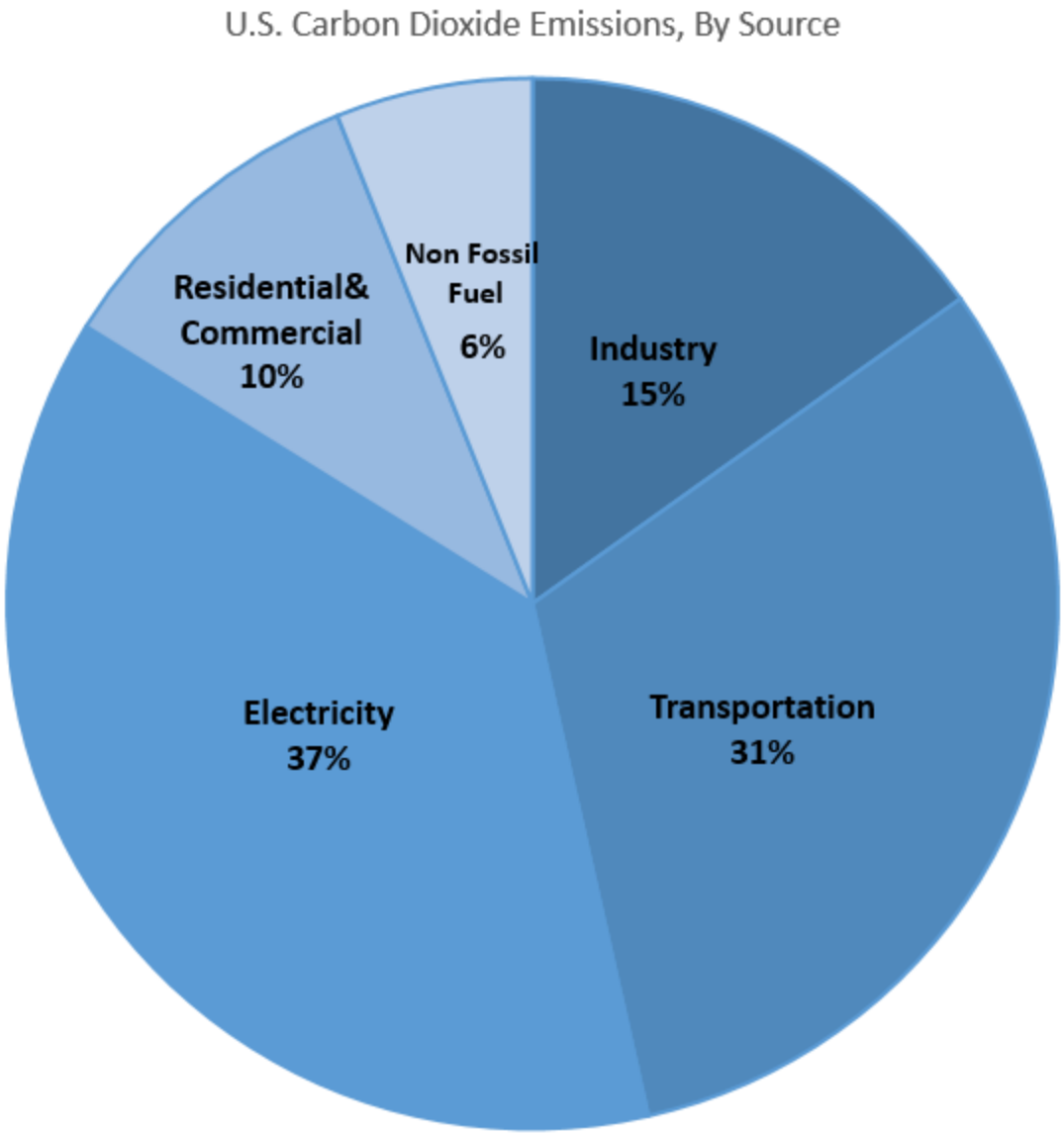

Figure 1.5. All CO_2 emissions in US, by source (from Inventory of U.S. Greenhouse Gas Emissions and Sinks: 1990-1023).

Traditional combustion involves the high temperature redox reaction between hydrocarbon and oxidizer; usually air (80% N_2). Novel combustion techniques for power plant with carbon dioxide capture have been proposed to efficiently reduce major greenhouse gas-CO_2 emission, including pre-combustion[5], post combustion[6], oxy-fuel combustion[7] and chemical looping combustion[8].

Pre-combustion refers to removing of carbon species in the fuel before combustion, shown in Figure 1.6, by gasification process of hydrocarbon at high temperature and pressure to form syngas, and then syngas undergoes water-gas shift reaction to convert CO to CO_2, producing a mixture with H_2 and high concentration CO_2 (more than 50%). The CO_2 could be easily separated and leaves carbon-free fuel content to combust.

In oxyfuel combustion, shown in Figure 1.7, pure oxygen instead of air (80% N_2) is used as oxidizer, and the product from hydrocarbon with pure oxygen will only be steam and CO_2, thus pure CO_2 stream could be obtained by water condensation.

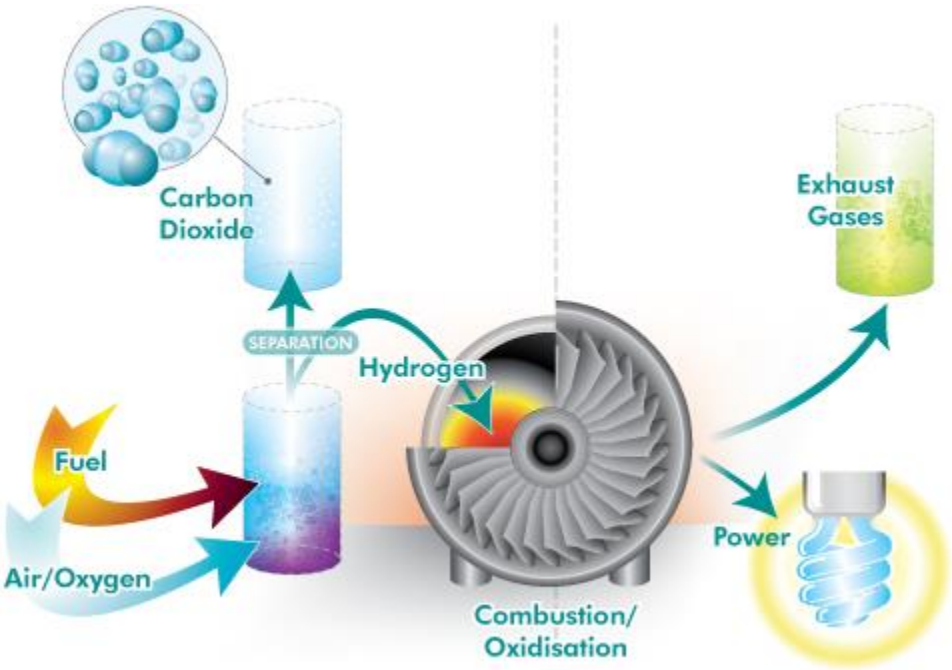

Figure 1.6. Schematic overview of pre-combustion technology.[9]

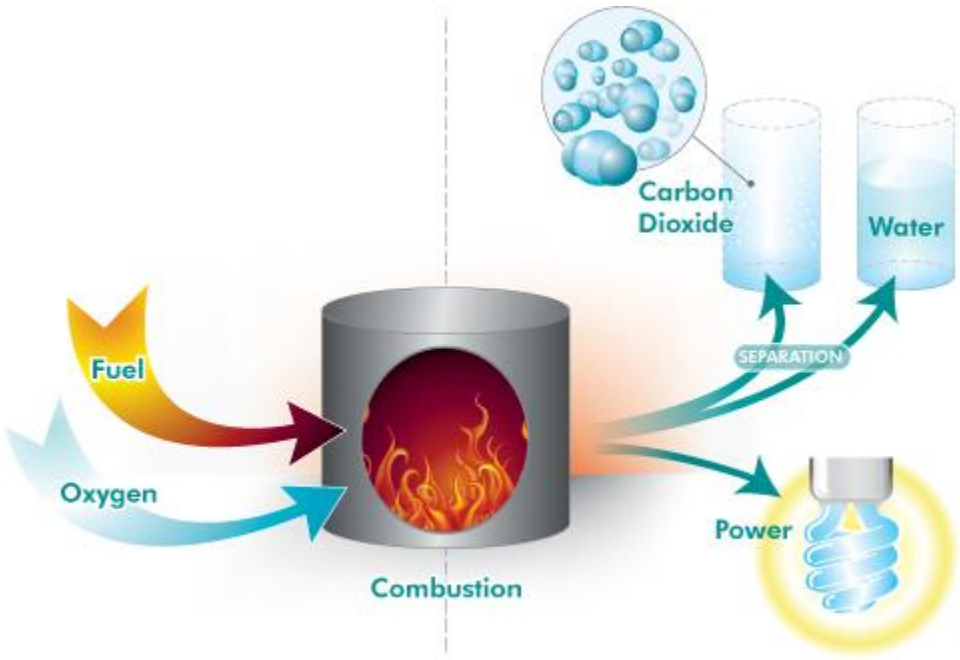

Figure 1.7. Schematic overview of oxyfuel combustion technology.[9]

Chemical looping combustion is a two-step combustion technique, shown in Figure 1.8, and it utilizes metal oxides instead of air (80% N_2) as the oxidizer to burn hydrocarbon fuels such that the separation of CO_2 from N_2 is avoided, and hydrocarbons are converted to carbon dioxide and water while reduced metal oxides are transferred into an air reactor, and further oxidized back to the original form. With both reactions occurs below 1100 ^oC, chemical looping combustion could avoid NO_x formation as well.

The exploration of novel combustion technologies requires the study of novel materials, which make the applications of those technologies possible. One of these approaches involves the use of nanostructured materials.

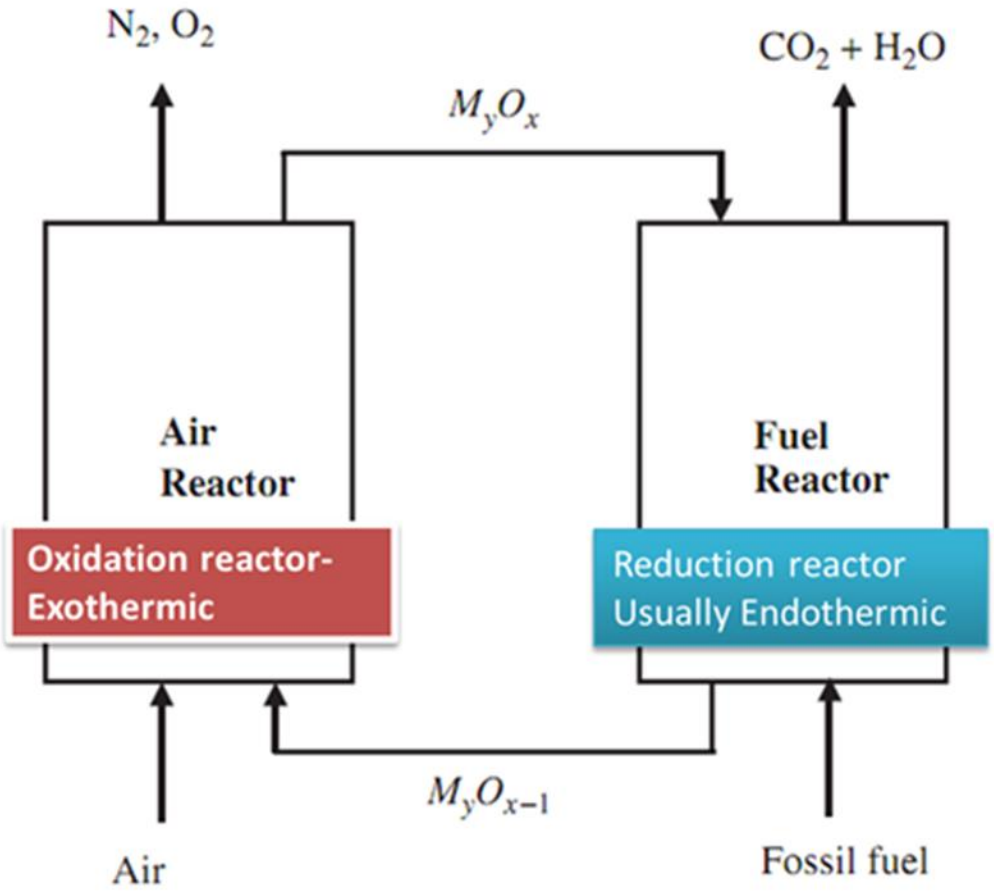

Figure 1.8. General schemes of chemical looping combustion.

1.1.2 Nanostructures

The nanoscale covers from 0.1 nm to 100 nm dimension, and nanomaterials are materials composed of units within this scale range. Single atom and molecule's diameter are several Angstoms (À), while 1 À=0.1 nm. Nanomaterials offer large surface to volume ratio, which are highly related to their synthesis, processing and applications.[10] The smaller the particle size, the higher surface to volume ratio. The existence of high percentage surface to volume ratio helps promote the surface energy, thus the atomic diffusion, leading to many size dependent phenomena [11,12,13,14,15]. Thus, nanomaterials have attracted a lot of interests for more than decades in various applications, because of their superior mechanical, electrical and catalytic performances.[16]

1.1.3 Synthetic methods of nanostructures

Here we utilize the aerosol synthetic method to obtain nano-structured metal oxides.[17] Aerosol includes a suspension of fine liquid droplets or particles, up to 100 μm, in a gas phase, which could be natural, such as fog and cloud, or artificial, such as dust, haze, mist, fume and smoke.[17] A common method for large scale industrial production of nanomaterials is the aerosol based processes because it is simple, highly scalable and continuous, compared to wet chemical synthesis.[17,18] The usage and applications of aerosol has started decades before the basic aerosol science and engineering are well understood. For instance, generation of pigments, including carbon black and titania, is from aerosol method while fumed silica and titania are generated from their chloride precursors by flame pyrolysis.[17] The aerosol synthetic method involves thermal decomposition of aerosols precursors generated by a

nebulizer and carried by a gas flow through a hot zone. When precursors are sprayed onto a hot surface or into hot atmosphere beyond their decomposition temperature, the target particles will be formed in the hot zone. This synthetic method includes flame synthesis, where particles are sprayed into high temperature flame[19], or spray pyrolysis[20] where precursor droplets are sprayed into a flameless high temperature reactor. It follows the droplet-to-droplet mechanism, where each droplet is a microreactor as they are carried by the carrier gas into the hot zone where reaction occurs. The first step in the aerosol-assisted synthesis is breakage of precursor solutions into fine droplets through a nebulizer. A nebulizer utilizes either shear force, ultrasonic energy or electrical force to break precursor solution into fine droplets. A widely used atomizer is the ultrasonic nebulizer type because of energy efficiency, affordability and inherent low velocity of the initial precursors, which breaks up the precursors into droplets through vibrations from the ultrasonic energy. Another pressure typed nebulizer is widely used in industries due to its stability and economy. It is the one we used in our lab, with its configurations shown in Figure 1.9. According to Bernoulli's Principle and Venturi Effect, $P_1<P_2=P_0=1$ atm, therefore liquid flow will be sucked up from the atomizer and then broke into droplets by shear force from the compressed air flow.

The spray pyrolysis utilized in our lab is described in Figure 1.10, it is a process for preparing particles or films by first generating droplets form a precursor solution, then solvent evaporating and decomposing precursors in a reactor. Briefly, particles are formed through an aerosol “droplet-to-particle” process, and unlike liquid synthetic methods, it could produce particles continuously. This process has

been widely used in the preparation of particles in various applications, including solid oxide fuel cell, lithium ion batteries and catalysts. Various nanomaterials could be prepared through spray pyrolysis, including solid/porous/hollow metal, metal oxides[20] and sulfides[21], nanocomposites[22], highly porous carbons[23] *etc*.

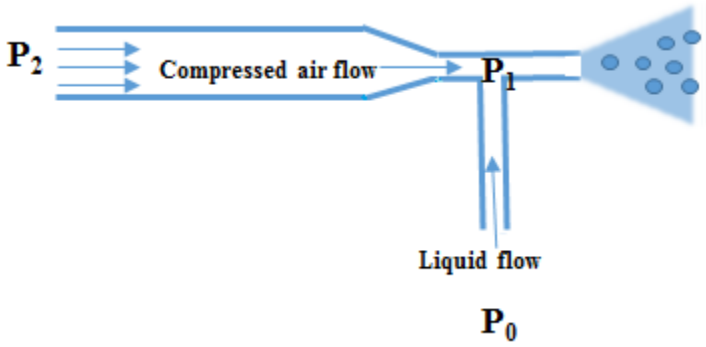

Figure 1.9. Configuration of a pressure typed nebulizer.

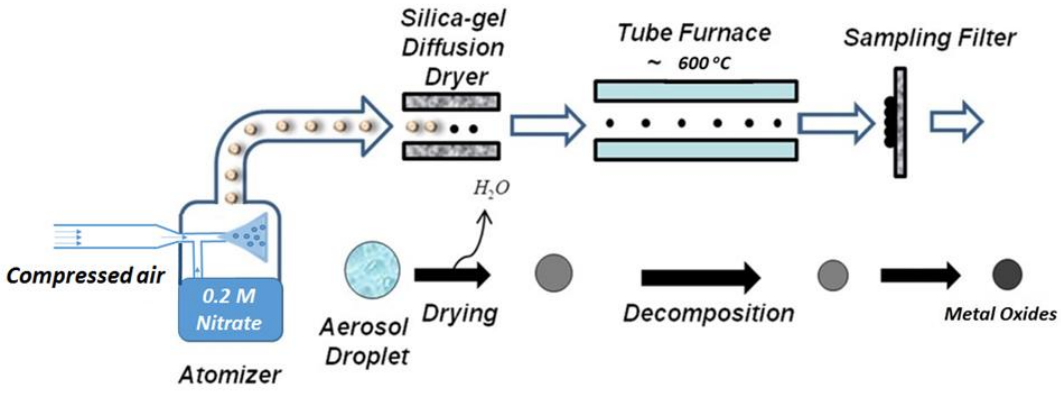

Figure 1.10. Configuration of spray pyrolysis set up.

1.2 Applications

1.2.1 Oxygen Carriers in Chemical Looping Combustion

Chemical looping combustion is a novel combustion technique that offers little carbon footprint with little energy penalties.[24] The wide applications of chemical looping combustion depends on the explorations of proper oxygen carriers, which should 1) be stable under repeated oxidation/reduction cycles; 2) show fast kinetics both at oxidation and reduction steps; 3) little coking formation from hydrocarbon decomposition at reduction step; 4) economically feasible and 5) environmentally benign. Therefore, single or mixed (Cu-, Mn-, Co-, Fe-, Ni-) transition metal based oxides and Ca- based alkaline earth sulfates have been tested as oxygen carriers.[24]

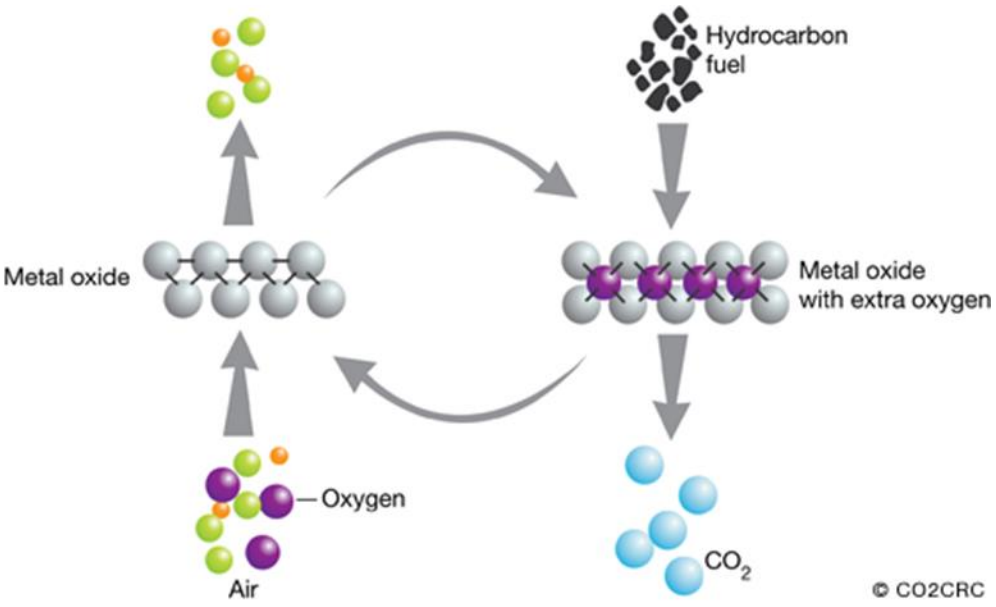

Figure 1.11. Schematic overview of oxygen transport in CLC. (http://theconversation.com/chemical-looping-a-carbon-capture-technology-for-the-future-12435).

Copper oxide has a relatively low melting and decomposition temperature, below 800 ^{o}C, and will go through chemical looping oxygen uncoupling (CLOU) process during the reaction with hydrocarbon, which releases oxygen to react with fuels.[25] Its low melting point leads to a tendency for sintering and defluidization in reactors, therefore, a supporting material is usually utilized to overcome those issues. Manganese oxide and cobalt oxide will follow the CLOU reaction path in the fuel reactor with oxygen releasing occurring before reaction with hydrocarbon.

Nickel and iron oxides are non-CLOU metal oxides, and oxygen will stay in the solids to react with hydrocarbon.[26] Iron oxides are widely studied OC material, since it is inexpensive, environmental benign and earth abundant, with high melting point and mechanical strength.[27] However, it is easy to sinter and shows slow reduction kinetics. After applying proper support materials, improved reactivity and recyclability will make it a good performing OC.

Mixed metal oxides, including Mn-Fe, Mn-Ni, Mn-Mg, and Mn-Cu[28,29] are explored as OCs, showing synergistic effects. Naturally occurring minerals, such as ilmenite, are also potential candidates as OC, which is reduced to Fe_2TiO_5 and oxidized to $FeTiO_3$ in multiple cycles.[30] It exhibits high oxygen storage capability compared to Fe_2O_3 to Fe_3O_4 redox cycle. Perovskites, shown in Figure 1.12, usually with chemical formulated as ABO_3, are known for high oxygen conductivity, thermal stability and fast oxygen-diffusion.[31,31-32] The ideal perovskite structure is cubic symmetry, with B cation in 6-fold coordination and A cation in a 12-fold coordination, shown in Figure 1.12. Perovskite has been proved to be qualified oxygen carriers with long time stability offering fast oxygen transportation.[33,34]

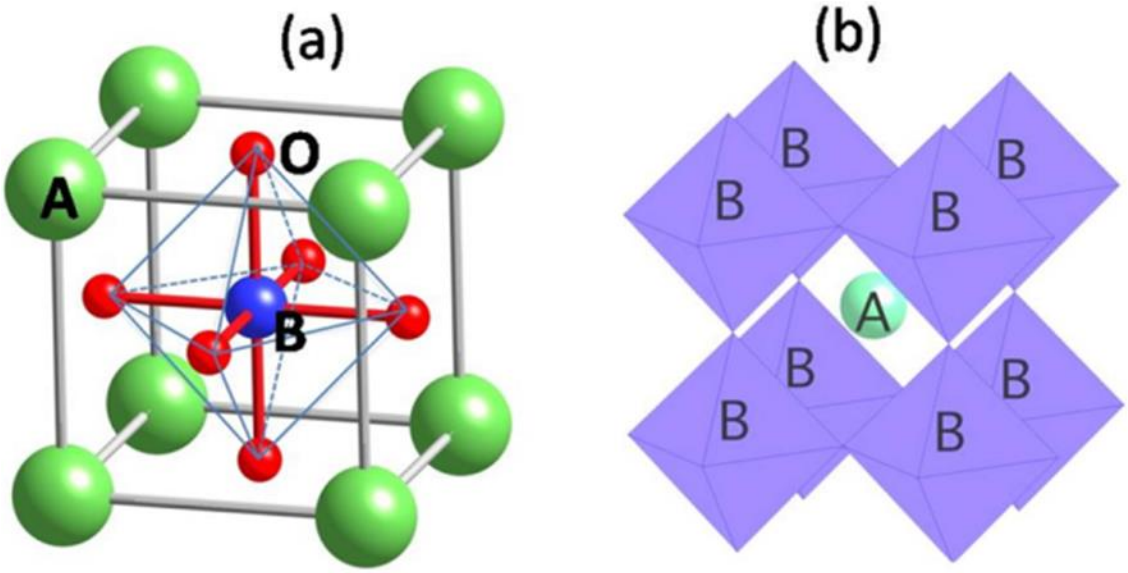

Figure 1.12. Perovskite crystal structure.

1.2.1.3 Supporting Materials

Supporting materials are added to provide enhanced chemical and mechanical stability, recyclability as well as oxygen transport ability to OCs. Inert supports, such as $MgAl_2O_4$[35], Al_2O_3[36], TiO_2[37], SiO_2[38], ZrO_2[24], are used as support materials to offer extra stability and prolong recyclability of mixed and single metal oxide OCs.

For example, Cu-based OCs show high reaction rates and high oxygen transfer capacity with almost complete fuel conversion, however, its proneness to decompose at low temperatures (~950 K) and tendency to sinter makes it impractical to use pure CuO in CLC applications. Therefore, to improve Cu-based OCs, various supports have been utilized, including Al_2O_3, $MgAl_2O_4$, SiO_2, TiO_2, Yttria stabilized zirconia (YSZ) *etc.*[39,40,41,42,43,44,45]

Fe-based OCs attract continuous research interests because of their low cost, environmental benign, and abundance in nature. However, they suffer from weak redox characteristics and sintering; thus various supports are used in Fe-based OCs to improve performance.[38,37,36]

Reducible oxides (CeO_2, La_2O_3) are studied as supports for NiO to ensure complete conversion of fuel to CO2 compared to inert supports (Al_2O_3, SiO_2).[46a] Veser *et al.* has added lanthanum doped ceria as low as 2% to iron based oxygen carriers to double the effective oxygen carrying capacity.[46b]

1.2.1.4 Promoter additives to Oxygen Carriers

Phase separation is another reason for oxygen carrier materials degradation with OCs' phase segregating and sintering. Additives, such as alkali or alkali earth ions[47, 48] are added to prevent phase separation between OC and support and improve oxygen

utilization, with only less than 5% addition. Those ions could assist in binding OC and supports, thus reducing the potential of phase separation. The promoter additives do not work as support to the OCs since they are usually less than 5% and if too much additives are added, there would be negative effects to OCs' reactivity.

Besides the exploration of MOs as OCs, we also studied the MOs as catalytic thermal decomposition catalysts of bio-friendly polymer, Poly Lactic Acid (PLA). PLA has been used as sacrificial polymer in the fabrication of battery separators and can be employed in 0D-3D Vaporization of a Sacrificial Component (VaSC) fabrication.

1.2.2 Catalysts in Thermal Poly Lactic Acid Decomposition

1.2.2.1 Poly Lactic Acid thermal decomposition

Bio-based polymers have attracted much attention due to their economic and ecological benefits.[49] Lactic acid is mainly produced from plants (mainly from starch and sugar) including corn, potatoes and beets, and bacteria could generate its monomers also.[50] The chemistry of the interconversion between lactide and poly lactic acid is shown in Figure 1.13.

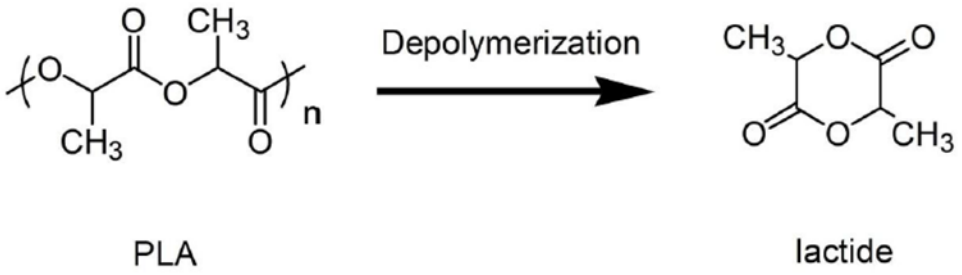

Figure 1.13. Chemistry of the decomposition from PLA to lactide.

PLA is known as the most promising candidate of substituting the petroleum-based polymers in packaging[51] and fiber technology.[52] PLA has been explored as one of the two major 3-D printing inks (the other one being ABS (Acrylonitrile butadiene styrene)) due to its good thermoplasticity.[53] Compared to ABS, PLA offers biodegradability and biocompatibility. Because of its relative low thermal decomposition temperature (more than 200 ^{o}C lower than thermal stable polymers, such as polyimide (PI), epoxies, Poly(vinylidene fluoride-hexafluoropropylene) (PVDF-HFP), *etc.*, PLA has also been explored as a sacrificial component from 0D to 3D to create complex-shaped molds after thermal removal with thermal stable polymer copolymers.[53,54,55,56] Porous materials could not only regulate fluids transport in filtration,[57] but also facilitate ion exchange in battery electrodes[58] and separator films[59].

1.2.2.2 Catalysts for PLA thermal decomposition

To further enlarge the thermal decomposition temperature difference between PLA and stable polymer mold copolymer, catalysts, such as alkali earth metal oxides[60], rare metal (scandium (III) triflates (CF_3SO_3-))[61], and tin containing compounds[62], have been added into PLA to further lower its thermal decomposition temperature. The addition of catalysts into PLA could be achieved through surface treatment[54], solvent evaporation casting[55], or vane extruding[62].

By adding these catalysts, the decomposition of PLA could be further lowered, which could greatly shorten the heat treatment of PLA removal time, thus keeping the thermal stable polymers' integrity and stability.[60,53]

1.3 Scope of the Thesis

In chapter 2, alkaline (K-, Na-, and Cs-) doped iron oxide and alumina supported iron oxides were synthesized from on step aerosol spray pyrolysis and tested as OCs in fixed bed reactor with methane as fuel. In this study alkali metal doped Fe_2O_3 and Fe_2O_3/Al_2O_3 composite oxygen carriers were synthesized from spray pyrolysis, and the reactivity and stability as oxygen carrier materials were evaluated in a fixed bed reactor for 50 isothermal redox cycles using CH_4 as the fuel. We find that both Fe_2O_3 and Fe_2O_3/Al_2O_3 composite showed reactivity degradation over multiple cycles, with clear phase separation between Fe and Al, in the composites. In contrast, alkali metal doping (~ 5 mol%) with Na, K, Cs was found to stabilize the reactivity of the Fe_2O_3 over the 50 redox cycles and prevent phase Fe-Al separation in the composite. Methane to CO_2 selectivity was found to be relevant to dopant type, which decreased in the order of dopant type K, Cs, Na. The best performing alkali metal, K, enhanced long term stability significantly, with no observed degradation in kinetics and total conversion performance in the methane step, as well as reduced coke formation. Adding an alumina matrix to K doped Fe_2O_3 helped promote CO_2 generation as well as minimize coking, and was found to be the best performing material.

In chapter 3, silicalite-1 has been explored as the supporting material for iron oxide as OCs for the first time. We employed a silicalite-1 zeolite support to achieve OCs with high resistance against sintering and coking in CLC. Iron oxides (Fe_2O_3) with methane fuel were employed to demonstrate the approach and to quantify the influence of silicalite-1 support on conversion efficiency, durability, and selectivity of these OCs in CLC cycles. Two iron oxide-zeolite geometrical structures, a core-shell

Fe_2O_3@silicalite-1 and an Fe_2O_3-impregnated silicalite-1 (Fe_2O_3/silicalite-1), were created to improve Fe_2O_3 stability. The CLC tests showed that both structures led to less aggregation of Fe_2O_3 OCs at 1223 K. A comparison between Fe_2O_3/silicalite-1 and Fe_2O_3@silicalite-1 in CLC tests illustrates that Fe_2O_3 impregnated in zeolite had higher durability than in the core-shell structure. The selectivity of CH_4 to CO_2 followed the order of Fe_2O_3/silicalite-1 > Fe_2O_3@silicalite-1 >> bare Fe_2O_3. The high selectivity of Fe_2O_3/silicalite-1 to CO_2 in CLC tests can be attributed to the encapsulation of Fe_2O_3 inside channels of silicalite-1 that provides physical barriers for aggregation of OCs in CLC cycles as well as coke deposition on OCs. In conclusion, our study of the structure-function relation for silicalite-1 supported Fe_2O_3 OCs can form the basis for the development of silicalite-1 as efficient support in chemical looping applications.

Perovskite oxides, chemical formulated as ABO_3, has been studied as novel OCs in CLC due to its thermal stability and faster reaction kinetics. In chapter 4, ten perovskite type OCs, $La_xCa_{1-x}B$(Cr-, Mn-, Fe-, Co-, Ni-)O_3 were synthesized from spray pyrolysis and tested with methane as fuel in the fixed bed reactor at 1023 K. It has been found that the oxygen storage capacity (OSC) has negligible change with changing A site from Ca to La while there exists an inverted volcano shaped relationship between OSC and B site electronegativity. Thus 3*d* transition metal *B* site electronegativity could be used as a powerful descriptor in the OSC of perovskites with CH_4 total combustion thus could provide useful design rule in choosing perovskite type OCs in CLC and might also provide some design insight for other energy related applications of perovskites.

Also we explored Bi_2O_3, CuO and Fe_2O_3 nanoparticles synthesized from spray pyrolysis, as catalysts for PLA thermal decomposition in chapter 5. Poly Lactic Acid (PLA) has been used as sacrificial polymer in the fabrication of battery separators and can be employed in 0D-3D Vaporization of a Sacrificial Component (VaSC) fabrication. In this study, 1wt% PLA/Fe_2O_3, PLA/CuO, PLA/Bi_2O_3 composites are prepared by solvent evaporation casting. Scanning Electron Microscopy (SEM) images indicate that the embedded nanoparticles are well dispersed in the polymer matrix and X-Ray Diffraction (XRD) verifies the crystallinity of these Metal Oxides (MOs). Thermal stability analysis of PLA and PLA/MO composites is performed using a Thermogravimetric Analyzer (TGA) and Differential Scanning Calorimeter (DSC). The overall heat of combustion is measured by Microscale Combustion Calorimetry (MCC) and is found to be insensitive to the presence of nanoparticles. The overall catalytic effects of the three metal oxides trends as: Bi_2O_3>Fe_2O_3>CuO ≈ inert material. PLA/Bi_2O_3 decomposition onset temperature ($T_{5\%}$) and maximum mass loss decomposition temperature (T_{max}) are lowered by approximately 75 K and 100 K respectively compared to the neat PLA. The as-synthesized Bi_2O_3 is identified as the most effective additive among those proposed in the literature to catalyze the PLA thermal decomposition process. A numerical pyrolysis modeling tool, ThermaKin, is utilized to analyze thermogravimetric data of all the PLA/MOs and to produce a description of the decomposition kinetics, which can be utilized for modeling of thermal vaporization of these sacrificial materials.

1.4 List of Publications

[1] **L. Liu,** M. R. Zachariah, Y. Wu, D. Liu, Evaluation of novel support: Silicalite-1 for Fe-based oxygen carriers in chemical looping combustion, submitted to *Energy & Fuels.*

[2] **L. Liu,** E. Rodriguez, M. R. Zachariah, Influence of transition metal electronegativity on the oxygen storage capacity of perovskite oxides, *Chem. Comm.* **2016,** *52,* 10369-10372.

[3] **L. Liu,** M. R. Zachariah, S. I. Stoliarov, J. Li, Enhanced thermal decomposition and kinetics of Poly (Lactic Acid) sacrificial polymer catalyzed by metal oxide nanoparticles, *RSC advances*, **2015,** *5,* 101745-101750.

[4] W. Zhou, J. B. DeLisio, X. Li, **L. Liu**, M. R. Zachariah, Persulfate salt as an oxidizer for biocidal energetic nano-thermites, *J. Mater. Chem. A,* **2015,** *3,* 11838-11846.

[5] **L. Liu**, Michael R. Zachariah, Enhanced performance of alkali metal doped Fe_2O_3 and Fe_2O_3/Al_2O_3 composites as oxygen carrier material in chemical looping combustion, *Energy and Fuels*, **2013,** *27*, 4977-4983.

[6] G. Jian, **L. Liu**, M. R. Zachariah, Facile aerosol route to hollow CuO spheres and its superior performance as an oxidizer in nanoenergetic gas-generators, *Adv. Funct. Mater.* **2013,** *23,* 1341-1346.

[7] X. Ma, **L. Liu**, N. Aronhime, M. R. Zachariah, Ignition catalyzed by unsupported metal nanoparticles, *Energy and Fuels*, **2011,** *25*, 3925-3933.

Chapter 2: Alkali Metal doped Fe_2O_3 and Fe_2O_3/Al_2O_3 Composites as Oxygen Carrier

2.1 Introduction

Chemical Looping Combustion (CLC) involves a two-step process in which metal oxides as the oxygen carrier (OC) replacing air in order to avoid direct contact between fuel and air.[5] Current primary interests in CLC lie in the potential advantages of burning hydrocarbons or coal in a nitrogen-free environment so as to enable more efficient/economical CO_2 sequestering as well as avoid NO_x formation.[63,64] However, finding good oxygen carriers is one of the major challenges in any widespread implementation of CLC.[8] The important properties of oxygen carriers are high reactivity to both reduction and oxidation, as well as high mechanical stability and recyclability over multiple cycles, low cost and environmental benign.[39, 65] Metal oxides including copper-, iron- nickel-, and mixed-oxide have been studied, however, Fe-based oxygen carriers while economical, have shown relatively slow reduction rate and a propensity for physical and chemical degradation over time.[66,67,68] Fe_2O_3 can be sequentially reduced to Fe_3O_4, FeO, and finally Fe, with different CO_2 conversions.[69] The economic advantages of an iron-based material coupled with its high melting point and environmental benign have continued to maintain interest as these materials. In an effort to enhance active surface area, pore volume, sintering resistance, long term stability and recyclability, support materials including Al_2O_3,

SiO_2, MgO, TiO_2, ZrO_2, CeO_2 have been employed.[40b,68,46a,70] The performance improvement with supported OCs was often attributed to enhanced intra-particle gaseous diffusivity, as well as electronic or O^{2-} mobility considering the reactions between OC and fuel are gas-solid or solid-solid reactions.[37,71]

In order to enhance the reactivity of Fe_2O_3, we have referred to the fact that alkali metal doping of catalysts has been known to improve selectivity, activity or prolong lifetime of metal/metal oxide catalysts.[72,73,74,75] Specifically, activity decreases in the order of Cs, K, Na, Li, attributed to the decreasing size, polarization and electronegativity.[75] While strictly speaking the oxygen carrier is considered a reactant and not a catalyst one might expect that some of the same principles that improve catalyst may also improve oxidation performance. With that logic, in this study we demonstrate that K doped Fe_2O_3 offers significant improvement in performance, both cycling and a lower coke formation potential in the reduction step with methane, while other alkali metals are not as effective. Further enhancement is seen when alumina is included to make composite alkali doped particles. In both cases no long-term degradation in performance is observed.

2.2 Experimental Approach

2.2.1 Oxygen Carrier Synthesis

All oxygen carriers studied were in-house synthesized by aerosol spray pyrolysis.[76] Briefly speaking, the system consists of an atomizer (to produce aerosol droplets), silica-gel diffusion drier (to remove solvent), a high temperature furnace, and a sample collector (to collect nanoparticles). The aerosol of precursor solution is

generated using a collision-type nebulizer with an initial droplet diameter is about 1 μm, which is dried by passing through diffusion dryer. The aerosol is then passed through a tube furnace operated at 873 K to create the solid particle with a residence time of ~1 s. Particles exiting the aerosol reactor are then collected on a 0.4 μm DTTP Millipore filter. To thermally decompose all nitrates completely, all particles were annealed at 1023 K for 1 h before the CLC test.

The precursors for the Fe_2O_3, Al_2O_3 and alkali metal components were $Fe(NO_3)_3 \cdot 9H_2O$, $Al(NO_3)_3 \cdot 9H_2O$ and MNO_3 (M= Na, K, Cs) respectively at a total concentration of 0.2 M. For the samples tested in this work, a 5 mole% of alkali metal relative to Fe was added, in each case, such as 4.8mol% K/95.2mol% Fe_2O_3 ($Fe_2O_3 \cdot K$), 4.8mol% Cs/95.2mol% Fe_2O_3 ($Fe_2O_3 \cdot Cs$), 50mol% Fe_2O_3/ 50mol% Al_2O_3 (1Fe1Al), 2.6mol% K 48.7mol% Fe_2O_3/ 48.7mol% Al_2O_3 (1Fe1Al·K), 2.6mol% Na 48.7mol% Fe_2O_3/ 48.7mol% Al_2O_3 (1Fe1Al·Na), 1.3mol% Na 1.3mol% Na 48.7mol% Fe_2O_3/ 48.7mol% Al_2O_3 (1Fe1Al•1K1Na).

2.2.2 Fixed bed reactivity test for CLC OCs

The reactivity of oxygen carriers was tested in a vertically oriented fixed bed reactor placed in an electrically heated isothermal furnace. While industrial practice probably favors the use of fluidized-beds, there are examples of designs for full scale fixed bed reactors for CLC[77,78]. From a laboratory stand-point fixed bed studies are widely used due to the simplicity of operation and the small samples that can be utilized[79, 46a, 80, 81]. This latter point was of particular interest to us since our focus is on materials synthesis and rapid screening. Readers will also note that our materials are nanoscale. Obviously this length scale is not practical in fluidized beds, however particles of the

type described here are easily generated by spray pyrolysis methods at various sizes[17]. Finally it is possible to construct micro-size particles comprised of nanoparticles by spray induced aggregation that offers accessible surface areas that greatly exceed the corresponding external surface area[82].

About 200 mg sample materials were used for each test. The quartz flow reactor has a length of 61 cm, with a 1 cm I.D, as shown in Figure 2.1. The particles were first annealed at 1023 K for 1 hour, and then exposed alternatively to 11% methane for 2 min and 20% oxygen for 5 min simulating the CLC system. Argon is introduced for 300 s after each period, to avoid oxygen and methane mixing during the switch between oxidation and reduction. 50 cycles were achieved in this test.

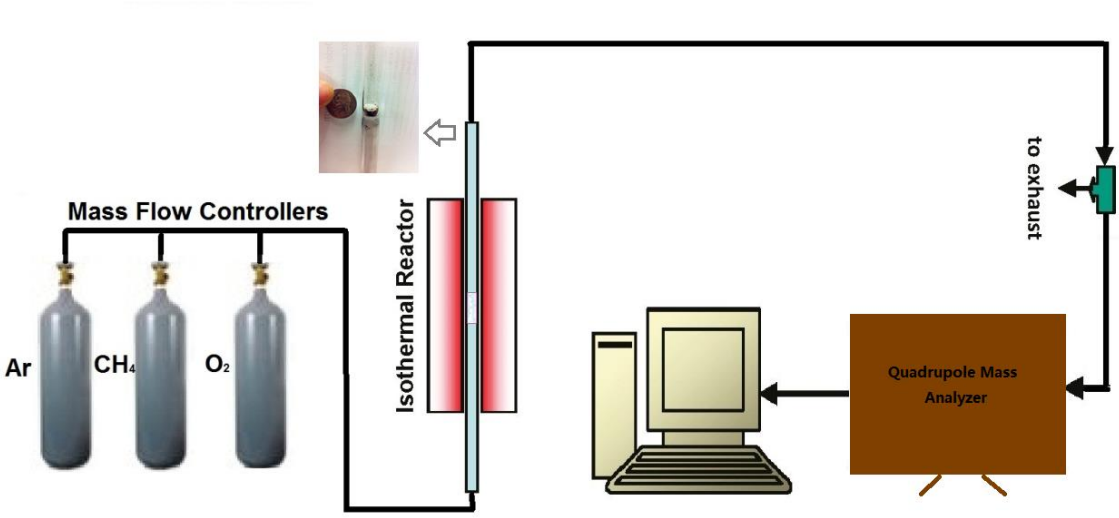

Figure 2.1. Schematic diagram of CLC system.

MKS Mass Flow Controllers (MFCs) for the three gases were regulated by a Labview VI program. The reactor effluent was characterized by a mass spectrometer (Stanford Research UGA 300) operating with a mass resolution <0.5 atomic mass unit (amu) at 10% of peak height and a detection limit <1 ppm. Argon was used as an inert internal standard to determine the volume change of gaseous reactants and products during the reaction so as to assign concentrations. By varying flow rates of CH_4, O_2 with fixed Ar flow rate, calibrations of mass spectrometer for different gases with different concentrations were accomplished. Crystal structures of OCs were characterized by X-Ray Diffraction (XRD) with a Bruker Smart1000 using Cu Kα radiation. Transmission electron microscopy (TEM) and elemental mapping were performed using a field-emission transmission electron microscope (JEOL JEM 2100F). Scanning electron microscopy (SEM) and Energy-Dispersive X-ray (SEM-EDX) results were obtained by Hitachi SU-70 SEM.

2.3 Results and Discussion

A differential mobility analyzer (DMA) coupled with a condensation particle counter (CPC) described in our previous work, was utilized to obtain the size distribution of the as-synthesized particles.[80] As shown in Figure 2.2c, the Fe_2O_3 particle diameter peaks at 84 nm without K and 87 nm with 5mol% K, implying that particle size effects can be ignored in any comparison. Similar results were obtained with other dopants (Na, Cs).

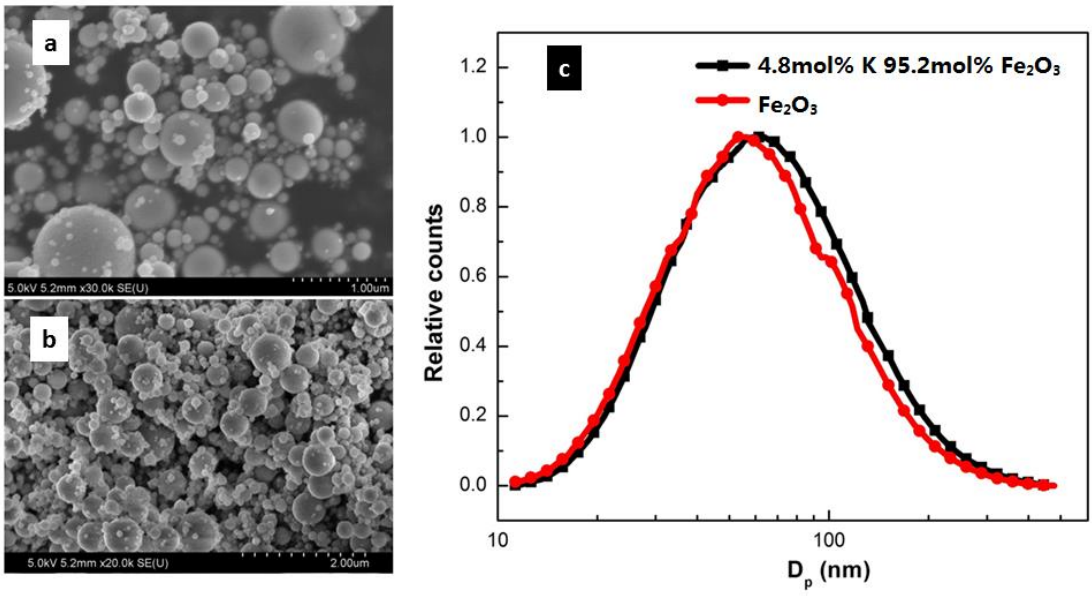

Figure 2.2. SEM images and Particle-size distributions of as-synthesized Fe_2O_3 a), b) 4.8mol% K 95.2mol% Fe_2O_3, c) produced by spray pyrolysis measured using a differential mobility analyzer (DMA) coupled with a condensation particle counter (CPC).

The multiple-cycle test in the fixed bed reactor examines the reactivity and stability of the selected oxygen carriers. Figure 2.3a illustrates the temporal dependence of oxygen carrier reduction with CH_4 reaction to CO_2 of neat Fe_2O_3 sample at the 1^{st} cycles. Normalized time is the real time normalized by the pulse length. The conversion-time plot shows a sigmoidal shape, indicating that the gas-solid reaction may proceed following the JMA model.[83, 84] Since this study primary focuses on total yield, selectivity and cycling stability, the data presented subsequently are under conditions of steady conditions (*i.e.* long times) so that temperature dependence of kinetics cannot be evaluated. Figure 2.3b shows that adding potassium results in a slight improvement in the kinetics without changing final yield. This is important since any long-term stability improvements though the addition of potassium should not ultimately degrade kinetic performance. Assuming that both cases share the same reaction order, the temporal conversion plots yield a reaction rate for the potassium added case roughly twice that for the neat iron oxide.

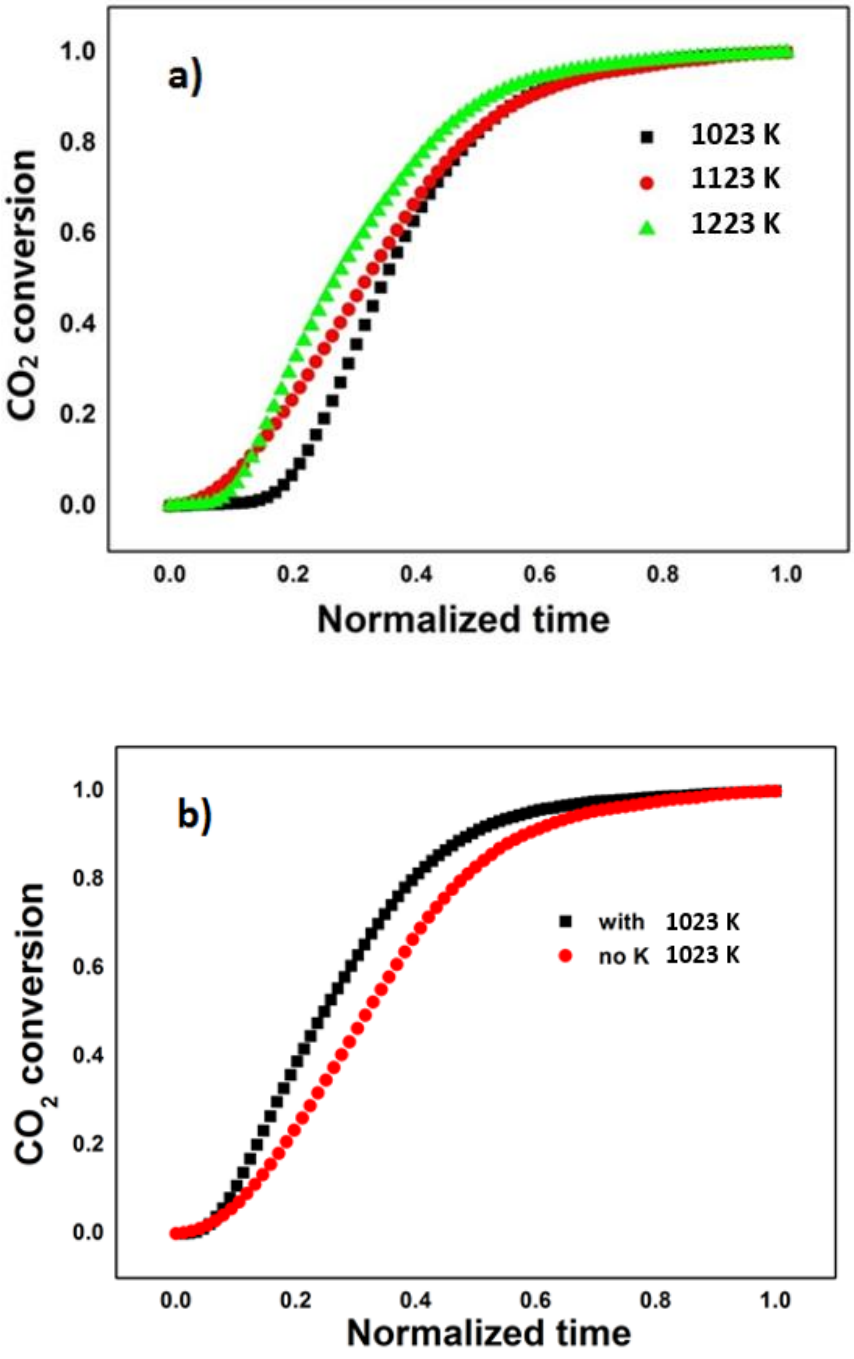

Figure 2.3. a) Effect of temperature on temporal CO_2 conversion for the 1st cycles of Fe_2O_3 in the CH_4 step, b) Comparison of potassium added vs. neat iron oxide CO_2 temporal conversion for the 1st cycle CH_4 step at 1023 K.

Figure 2.4. shows the performance behavior at different temperatures for unmixed (Figure 2.4a, 2.4c), and K added OCs' multicycle performance (Figure 2.4b, 2.4d). Theoretically, the conversion from Fe_2O_3 to Fe_3O_4 should give a CO_2 yield of 0.52 mmol/g from Fe_2O_3 to FeO, 1.56 mmol/g and from Fe_2O_3 to Fe, 4.69 mmol/ g. Equilibrium calculation shows that Fe_2O_3 to Fe_3O_4 under methane leads to 100% CO_2, but that subsequent partial reduction to FeO gives a mixture of CO and CO_2.[70,85] Our experimental results could not reliably quantify this point due to relative high mass 28 (N_2) background in our mass spectrometer. It is clear that for the 1st cycle of the neat Fe_2O_3 (Figure 2.4a) and 50mol% Fe_2O_3/ 50mol% Al_2O_3 (Figure 2.4c) samples, the Fe_2O_3 got converted to Fe_3O_4 after CH_4 step.

Also, it demonstrates that from Figure 2.4a that for pure Fe_2O_3 performance degrades steadily after each cycle, which has also been reported by others and is one of the problems plaguing many OCs.[86] Addition of aluminum nitrate to create an alumina stabilizing matrix (Figure 2.4c) for the Fe_2O_3 exhibited essentially identical behavior to the neat Fe_2O_3 oxide case, implying that at least under the synthetic strategy pursued here, the alumina offered no advantages. For both cases before K^+ addition (Figure 2.4a and 2.4c), CO_2 generation degraded to almost one third its first cycle at the 50th cycle. The addition of K however, shown in Figure 2.4b and Figure 2.4d stabilized the performance even up to 1223 K, with no temperature dependence to the conversion or stability over the 50 cycles studied. At various loadings, 80mol% Fe_2O_3 20mol% Al_2O_3, 67mol% Fe_2O_3 33mol% Al_2O_3 OCs were also tested, with no difference in performance detected. The degradation may be attributed to the decreasing oxygen-ion transport within the lattice or a reduction in the oxygen

binding energy.[87] Meanwhile, adding K^+ to the Fe_2O_3/Al_2O_3 composite also helped modify the degradation problem (Figure 2.4d). To be more specific, 2.6mol% K 48.7 mol%Fe_2O_3 48.7mol% Al_2O_3 OC also gave a steady CO_2 yield of Fe_2O_3 to Fe_3O_4 as the Fe_2O_3 case during those 50 cycles. What is responsible for this effect will be specified later in this work.

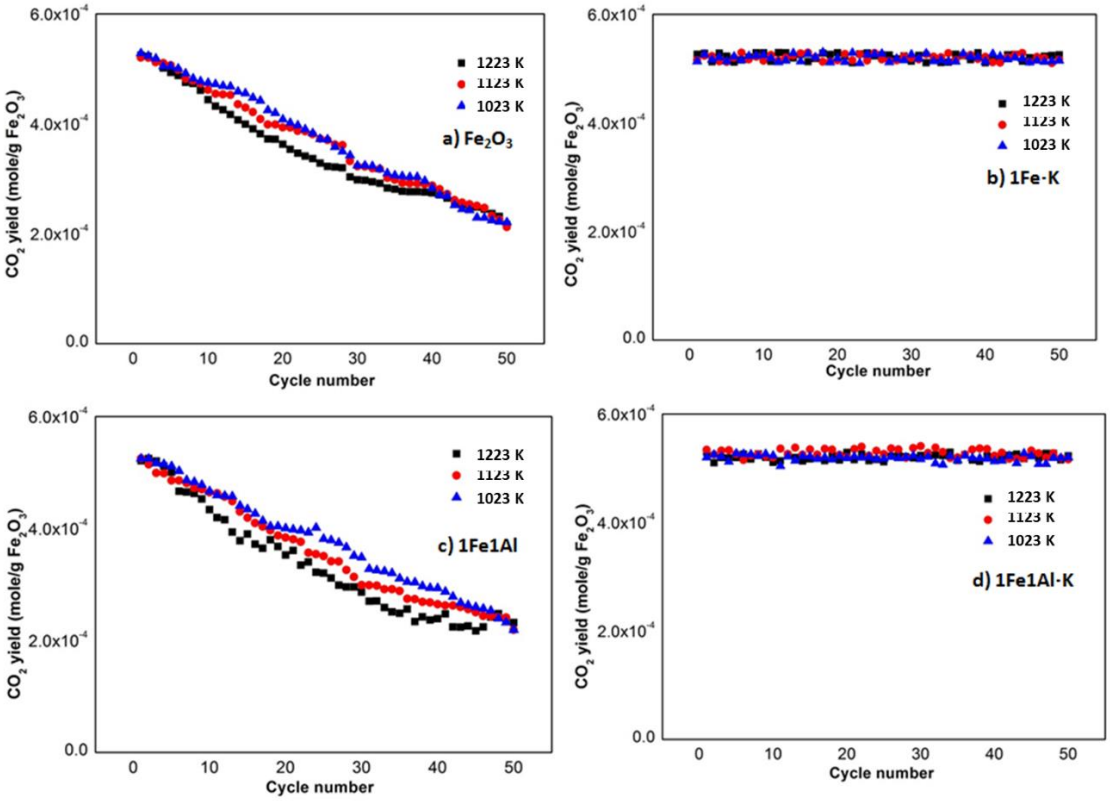

Figure 2.4. CO_2 yield per gram Fe_2O_3 for a) Fe_2O_3, b) Fe_2O_3·K (95.2mol% Fe_2O_3 with 4.8mol% K), c) 1Fe1Al(50 mol% Fe_2O_3/ 50 mol% Al_2O_3) ,d) 1Fe1Al·K (2.6 mol% K 48.7 mol% Fe_2O_3/ 48.7 mol% Al_2O_3) at 750 ^oC, 850 ^oC, 950 ^oC.

Next we turn to the effects of alkali metals as dopants. To compare the effects of different alkali doping, we chose to use Na, K and Cs to vary the size, polarization and electronegativity of the dopant. Plots of the CO_2 yields per gram Fe_2O_3 for different oxygen carriers (OCs) for 50 redox cycles is presented in Figure 2.5. The first thing to note is that addition of the alkali metal dopant clearly stabilizes the long term stability of the CO_2 conversion with no apparent decreases in performance over time, but only K offers high oxygen transport capacity for iron oxide. Usually, alkaline ions are considered as catalysts; however, they only prevent performance degradation instead of improving performance compared to the neat Fe_2O_3 initially in our case. Alkaline metals are thought to act as an electron donor for the iron based materials, and that the synergistic effects are ascribed to the weakening of the Fe-O bond.[88, 87] The Na added OC sample showed the worst performance which can be attributed to its smaller radius, lower electronegativity, consistent with previous work on the role of alkaline metals on catalytic activity.[75]

On that basis, however, Cs should perform better than K, but clearly did not. TEM images of reacted OCs (Figure 2.5 and Figure 2.6) show that Cs was not retained after thermal processing (at least at significant levels within the iron oxide lattice) but phase-separated into small primary particles decorating the surface (TEM-EDX identified that metal elements of the small grains on the bulk Fe_2O_3 surface are mainly Cs), possibly because of the increased atom size. Alkali metals have also been shown to improve selectivity, reduce coking or prolong lifetime of metal/metal oxide catalysts for various reactions.[88,73, 87,88] At least for the conversion addition of

aluminum oxide stabilizer there appears to be no advantage, but it is included here because of a subsequent discussion on selectivity.

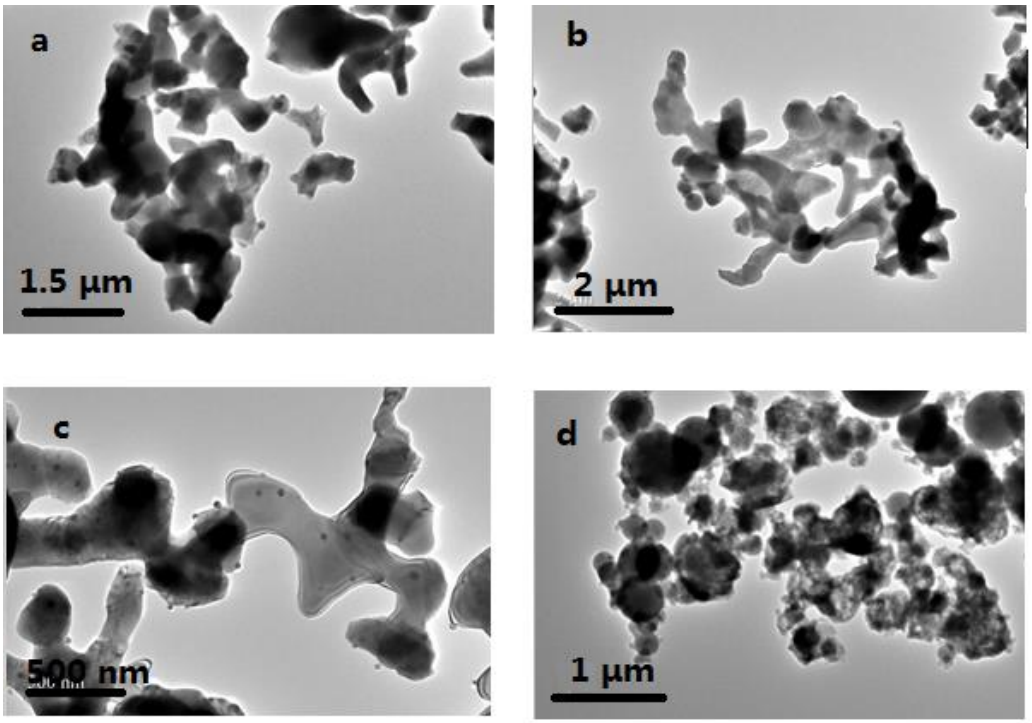

Figure 2.5. TEM images of alkaline doped OCs after 50 cycles CLC test at 1023 K of (a) 4.8mol% Na / 95.2mol% Fe_2O_3 (b) 4.8mol% K / 95.2mol% Fe_2O_3 (c) 2.6 mol% Cs 48.7 mol% Fe_2O_3/48.7 mol% Al_2O_3 (d) 2.6 mol% K 48.7 mol% Fe_2O_3/48.7 mol% Al_2O_3.

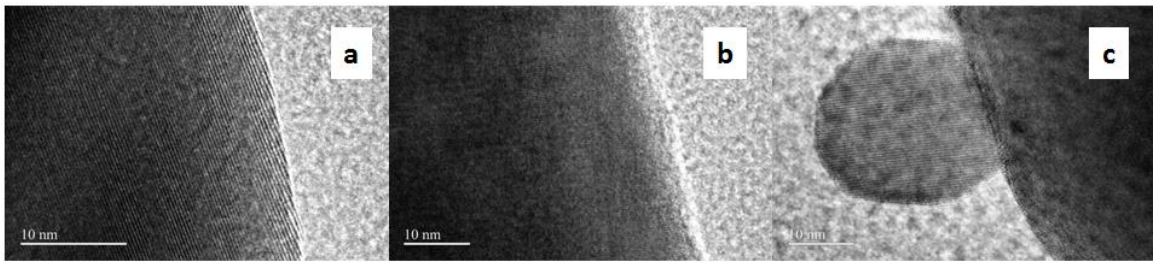

Figure 2.6. HRTEM images of alkaline doped OCs after 50 cycles CLC test at 1023 K of (a) 95.2 mol% Fe_2O_3/4.8 mol% Na (b) 95.2 mol% Fe_2O_3/4.8mol% K (c) 48.7 mol% Fe_2O_3/48.7 mol% Al_2O_3 with 2.6 mol% Cs.

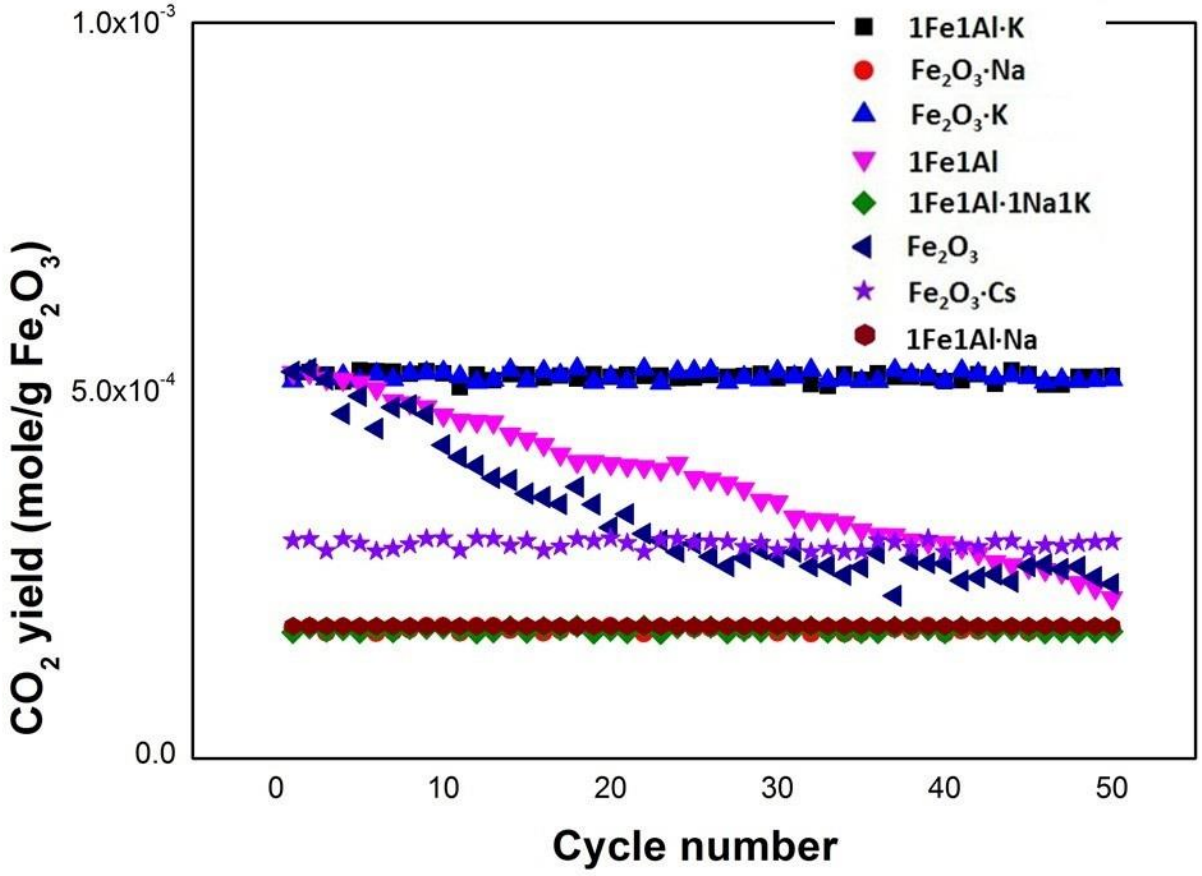

Figure 2.7. CO_2 yield per gram of Fe_2O_3 for different OCs at 1023 K as a function of cycle number.

Because one of the primary motivations of CLC today is CO_2 sequestering, selectivity is extremely important, specifically with respect to coking, which may occur from a number of side reactions including the Boudouard reaction (1) and methane pyrolysis (2).[85,81,89]

$$2CO \rightarrow C + CO_2 \quad (1)$$

$$CH_4 \rightarrow C + 2H_2 \text{ (pyrolysis)} \quad (2)$$

The second reaction is endothermic while the first reaction is exothermic. Furthermore, methane decomposition is thermodynamically preferred at high temperatures while the Boudouard reaction is favored at low temperatures. Carbon formation comes from the two reactions mentioned above, and then burned away in the oxidation step.[81 ,42] Therefore the amount of CO_2 observed in the oxidation step can be directly used to determine the extent of coke formation in the methane step. The two different side reactions can be differentiated by the amount of hydrogen generated during the methane step, as it results only from methane decompostion (reaction (2)). As the amount of hydrogen generated during the methane step was double the amount of CO_2 generated during the oxidation step, we can conclude that methane decompostion is the primary side reaction. We define CO_2 selectivity (based on the amount of CO_2 measuered during the fuel step) as:

$$\gamma_{CO_2} = \frac{n_{CO_2}}{n_C + n_{CO_2}}$$

where n_{CO_2} is determined directly during the fuel step, and n_C is meausred indirectly by the amount of CO_2 measured during the oxidation step.

Thus the selectivity represents the amount of methane that is reacting with the OCs rather than decomposing. γ_{CO_2} of different OCs at 1023 K for 50 cycles is shown in Figure 2.6. It is evident that addition of alkaline metals improves CO_2 selectivity against coking and that potassium works best in the context of selectivity. The addition of the alumina support provides further improvement. This 48.7 mol% Fe_2O_3/48.7 mol% Al_2O_3/2.6 mol% K material clearly offers superior performance in both reactivity stability and CO_2 selectivity. This result implies that alkali metals promote oxidation over pyrolysis although the mechanism is not well understood.

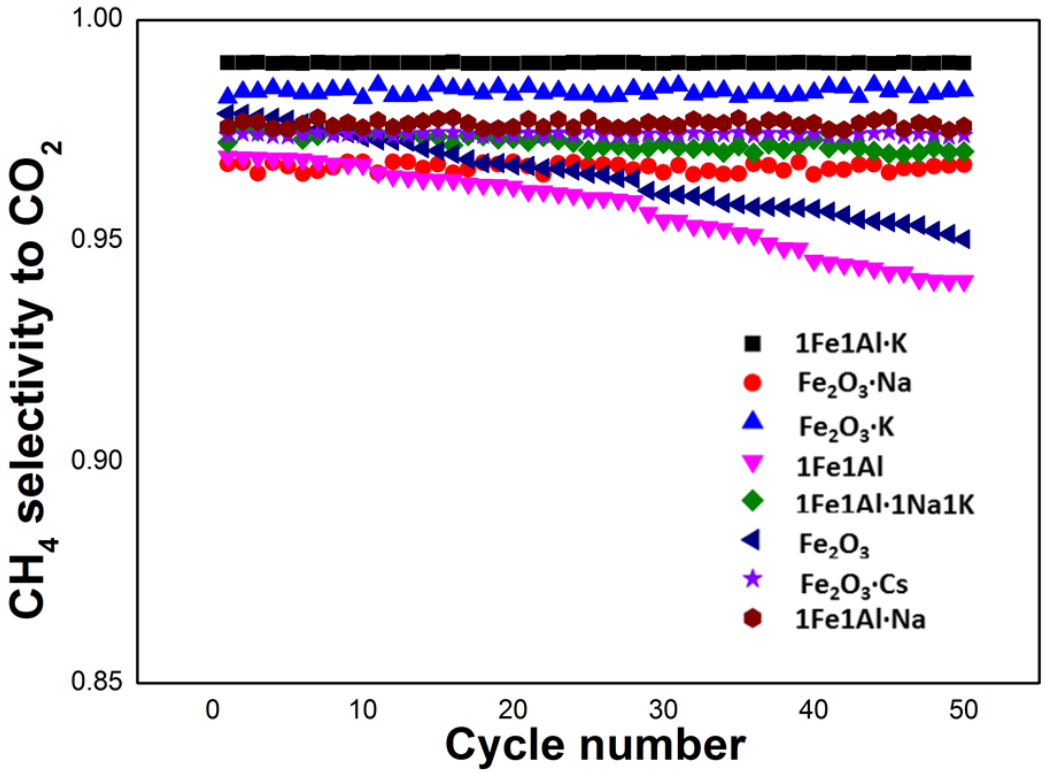

Figure 2.8. CO_2 selectivity- γ_{CO_2} of different OCs at 1023 K.

Phase identification of oxygen carriers was determined using XRD (Table 2.1), indicating that all iron oxides were γ-Fe_2O_3 or Fe_3O_4. Even though the samples were obtained after CH_4 step cooled down to room temperature in Ar, the high temperature reduced phase gets easily oxidized and thus all XRD patterns gave peaks assigned to Fe_2O_3 and four reduced samples (OC samples after CH_4 step) gave peaks of Fe_3O_4. No signals for K-Fe-O may come from two reasons: 1) K-Fe forms very fine particles beyond limit of XRD detection 2) K-Fe forms solid solutions. From HR-TEM results (Figure 2.7 and 2.8), the second one is more reasonable since K-Fe stayed homogeneously distributed in the particle. Also, The XPS and deconvolution results for Fe 2p core-level (Figure 2.9) of 4.8mol% K 95.2mol% Fe_2O_3 sample showed very similar patterns and main peaks of Fe 2p3/2 around 710.8 eV, which demonstrates no chemical bonding between K and Fe, which means that K^+ may move around in Fe_2O_3 crystal as ion interstitials. XRD analysis on the Al_2O_3 supported sample has two major phases: Fe_2O_3 and Al_2O_3, with no mixed Fe-Al-O phase formation and no mixed Fe-K-Al-O phase formation is detected (*e.g.* $KFeO_2$). Moreover, XPS also gave the same information.

Sample	Phase identification
Fe_2O_3 (Maghemite-Q)	Fe_2O_3(Maghemite-Q)
50mol%Fe_2O_3 / 50mol% Al_2O_3	Fe_2O_3 (Maghemite-Q), Al_2O_3
4.8mol% Na 95.2mol% Fe_2O_3	$NaNO_3$, Fe_2O_3 (Maghemite-Q)
4.8mol% K 95.2mol% Fe_2O_3	KNO_3, Fe_2O_3 (Maghemite-Q)
2.4mol% Na 2.4mol% K 95.2mol% Fe_2O_3	$NaNO_3$, KNO_3, Fe_2O_3 (Maghemite-Q)
4.8mol% Cs 95.2mol% Fe_2O_3	Amorphous
Fe_2O_3 after 1 h sinter at 1023 K	Fe_2O_3 (Maghemite-Q)
4.8mol% K 95.2mol% Fe_2O_3 after 1 h sinter at 1023 K	Fe_2O_3 (Maghemite-Q)
50mol% Fe_2O_3 / 50mol% Al_2O_3 after 1 h sinter at 1023 K	Fe_2O_3 (Maghemite-Q), Al_2O_3
4.8mol% Na 95.2mol% Fe_2O_3 after 1 h sinter at 1023 K	Fe_2O_3 (Maghemite-Q)
2.4mol% Na 2.4mol% K 95.2mol% Fe_2O_3 after 1 h sinter at 1023 K	Fe_2O_3 (Maghemite-Q)
4.8mol% Cs 95.2mol% Fe_2O_3 after 1 h sinter at 1023 K	Fe_2O_3 (Maghemite-Q)
Fe_2O_3 after 50 cycles at 1023 K	Fe_3O_4, Fe_2O_3 (Maghemite-Q)
Fe_2O_3 after 50 cycles at 1123 K	Fe_3O_4, Fe_2O_3 (Maghemite-Q)
Fe_2O_3 after 50 cycles at 1223 K	Fe_3O_4, Fe_2O_3 (Maghemite-Q)
4.8mol% K 95.2mol% Fe_2O_3 after 50	Fe_3O_4, Fe_2O_3 (Maghemite-Q)

cycles at 1023 K	
4.8mol% K 95.2mol% Fe_2O_3 after 50 cycles at 1123 K	Fe_3O_4, Fe_2O_3 (Maghemite-Q)
4.8mol% K 95.2mol% Fe_2O_3 after 50 cycles at 1223 K	Fe_3O_4, Fe_2O_3 (Maghemite-Q)
2.6mol% K 48.7mol% Fe_2O_3/ 48.7mol% Al_2O_3 after 50 cycles at 1023 K	Fe_3O_4, Fe_2O_3 (Maghemite-Q), Al_2O_3
2.6mol% K 48.7mol% Fe_2O_3/ 48.7mol% Al_2O_3 after 50 cycles at 1123 K	Fe_3O_4, Fe_2O_3 (Maghemite-Q), Al_2O_3
2.6mol% K 48.7mol% Fe_2O_3/ 48.7mol% Al_2O_3 after 50 cycles at 1223 K	Fe_3O_4, Fe_2O_3 (Maghemite-Q), Al_2O_3
4.8mol% Na 95.2mol% Fe_2O_3 after 50 cycles at 1023 K	Fe_3O_4, Fe_2O_3 (Maghemite-Q)
2.4mol% Na 2.4mol% K 95.2mol% Fe_2O_3 after 50 cycles at 1023 K	Fe_3O_4, Fe_2O_3 (Maghemite-Q)
4.8mol% Cs 95.2mol% Fe_2O_3 after 50 cycles at 1023 K	Fe_3O_4, Fe_2O_3 (Maghemite-Q)

Table 2.1. XRD identifications of different OCs' sample before and after 50-cycle CLC tests.

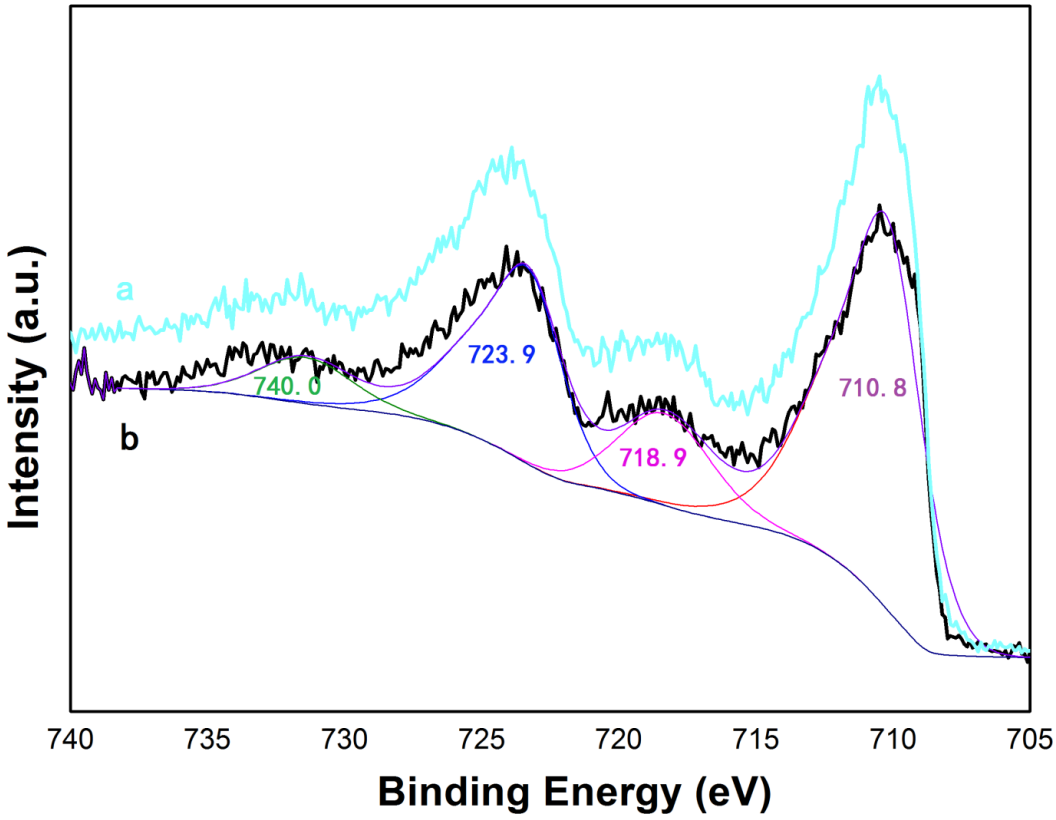

Figure 2.9. XPS and deconvolution results for Fe 2p core-level of a) Fe_2O_3 b) 4.8 mol% K 95.2 mol% Fe_2O_3 after 50 CLC cycles at 1023 K.

The SEM micrographs, of the OCs are shown in Figure 2.10. Consistent with the size distribution measurements in Figure 2.2 the as produced particles from spray pyrolysis were spherical ~0.1-1 μm. After ~ 1 h thermal annealing at 1023 K, particles maintained their spherical shapes. After 50 cycles (15 hours), particles clearly showed evidence of some sintering, although for all but the smallest particles the characteristic length scales are still nominally the same. The Na doped sample (not shown), was essentially indistinguishable from the K counterparts despite the fact that the reactivity was much lower. It is worth noticing that all particles displayed similar amounts of sintering, regardless of alkali metal doping. It can be implied than that sintering does not account for the reactivity differences.

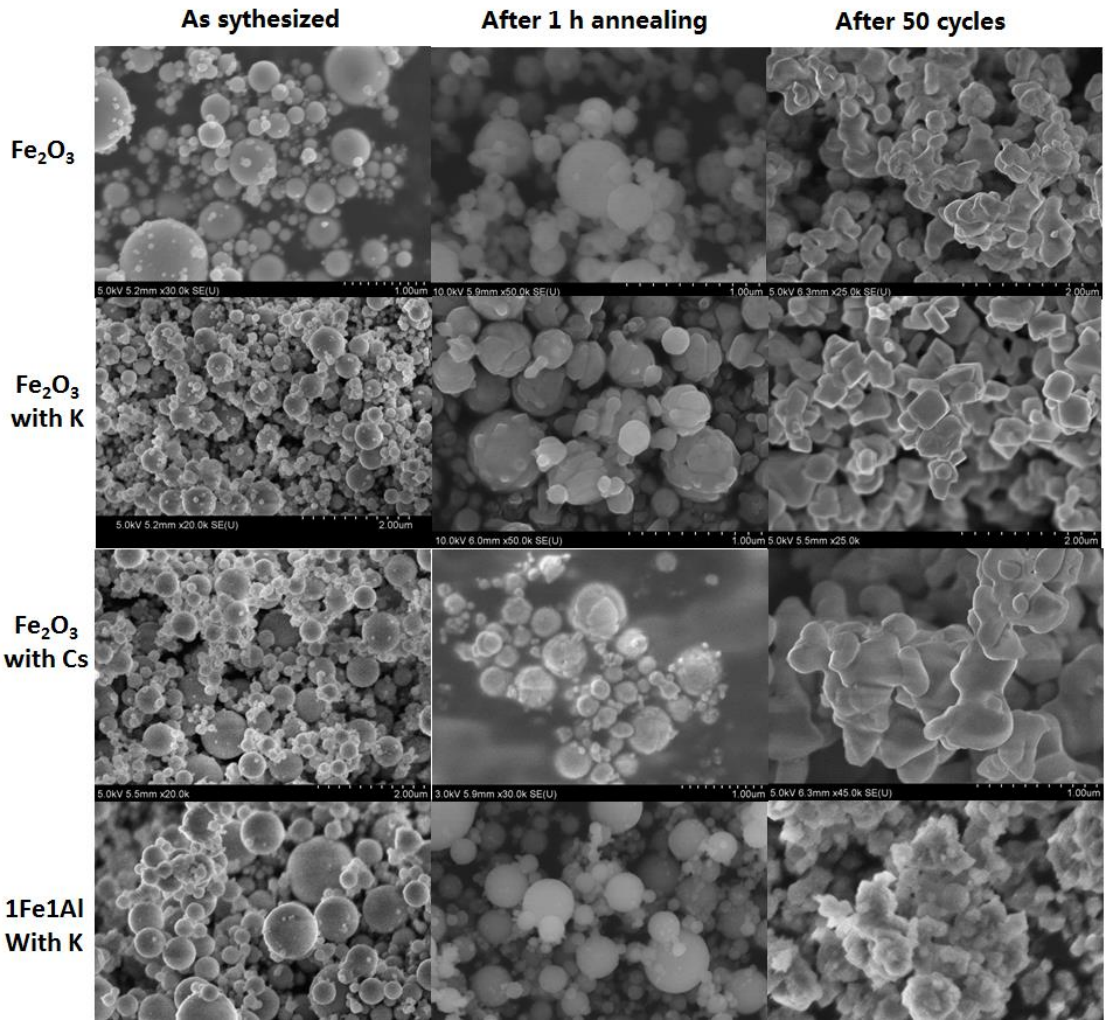

Figure 2.10. SEM images of OCs after direct synthesis, 1 h thermal annealing at 1023 K, and 50 cycles CLC test at 1023 K.

TEM elemental mapping is shown in Figure 2.11 and Figure 2.12, for the as prepared 50 mol% Fe_2O_3/ 50 mol% Al_2O_3 (Figure 2.11a, 2.11c), after multi-cycles at 1023 K (Figure 2.11b, 2.11d) and 2.6 mol% K 48.7 mol% Fe_2O_3/ 48.7 mol% Al_2O_3 after multi-cycle CLC at 1023 K. Figure 2.11a, 2.11c show that the as-produced material the iron is homogeneously dispersed within the alumina matrix, but that after CLC (Figure 2.11b, 2.11d), considerable morphological changes have occurred accompanied with a significant phase separation between Fe and Al. This is also consistent with the fact as shown in Figure 2.4 that the Al additions to iron oxide have minimal performance effects and shows the same general trend of decreasing activity with time. However, 2.6 mol% K 48.7 mol% Fe_2O_3/ 48.7mol% Al_2O_3 composite, as shown in Figure 2.12 clearly stabilizes the structure from both morphological sintering effects but also phase separation between Al and Fe.

Similar results (Figure 2.13) were achieved with the Na sample after 50 cycles, but recall that the Na containing sample did not perform well. The mapping results indicate that the alkaline metal helps to retard phase separation within the alumina support, which may account for the long-term stability of 2.6 mol% K 48.7 mol% Fe_2O_3/ 48.7 mol% Al_2O_3 OC relative to the nascent iron oxide, and little alkaline metal loss. Potassium ions movement may exist as a binder for Fe-Al, thus preventing phase separation between the two. This result indicates that alkaline effect here is more than catalytic surface effect; it is a whole particle effect.[90] Additional TEM images in the supporting information (Figure 2.7, 2.8), indicates that Cs however, did not stay in iron oxide, and was found to phase separate to the surface of the OC surface. This separation may be attributed to the larger size of the Cs^+ (~181 pm) ion

compared to K^+ (~152 pm) and Na^+ (~116 pm), as well its higher ion polarization.[75-86, 91] Previous catalysis studies have seen similar tends in the tendency for Cs phase separation.[72, 73-74]

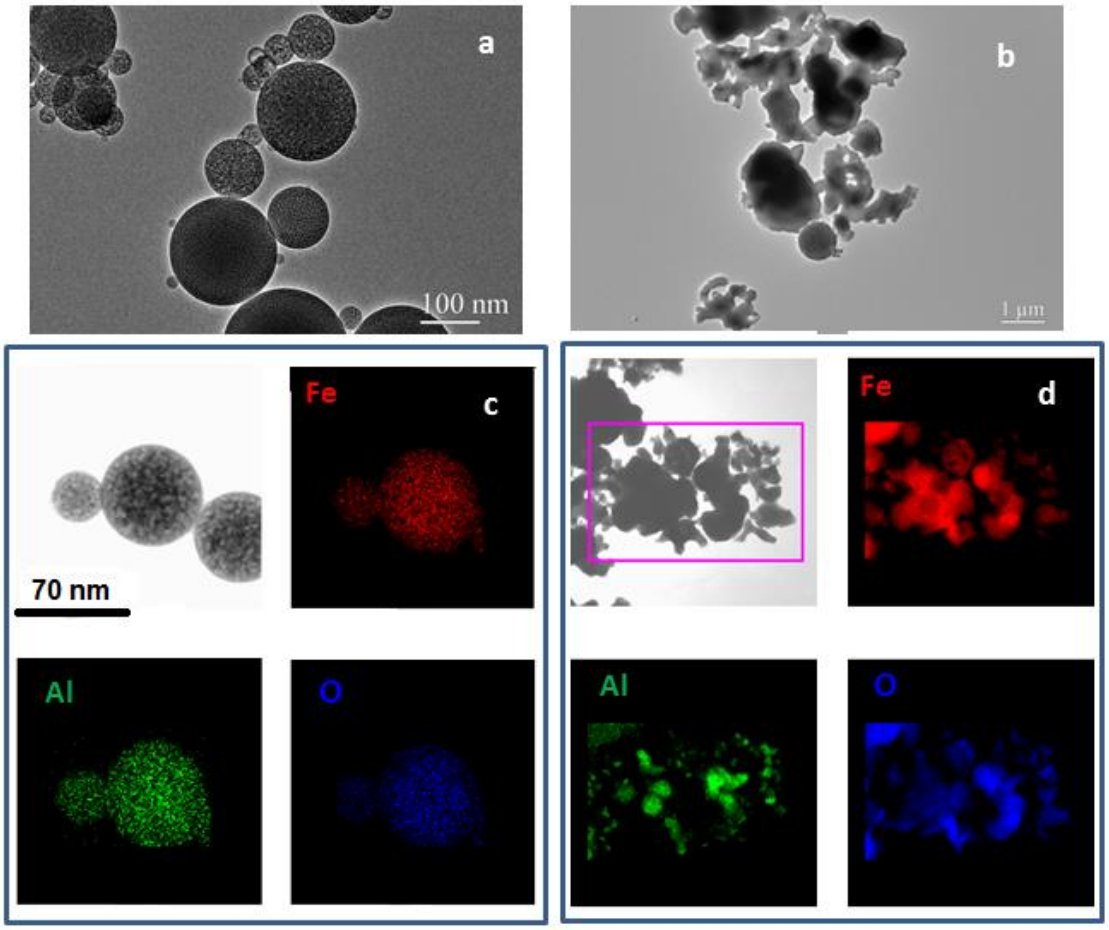

Figure 2.11. TEM and elemental mapping results for 50 mol% Fe_2O_3/50 mol% Al_2O_3: (a, c) As synthesized; (b, d) after 50 CLC cycles at 1023 K.

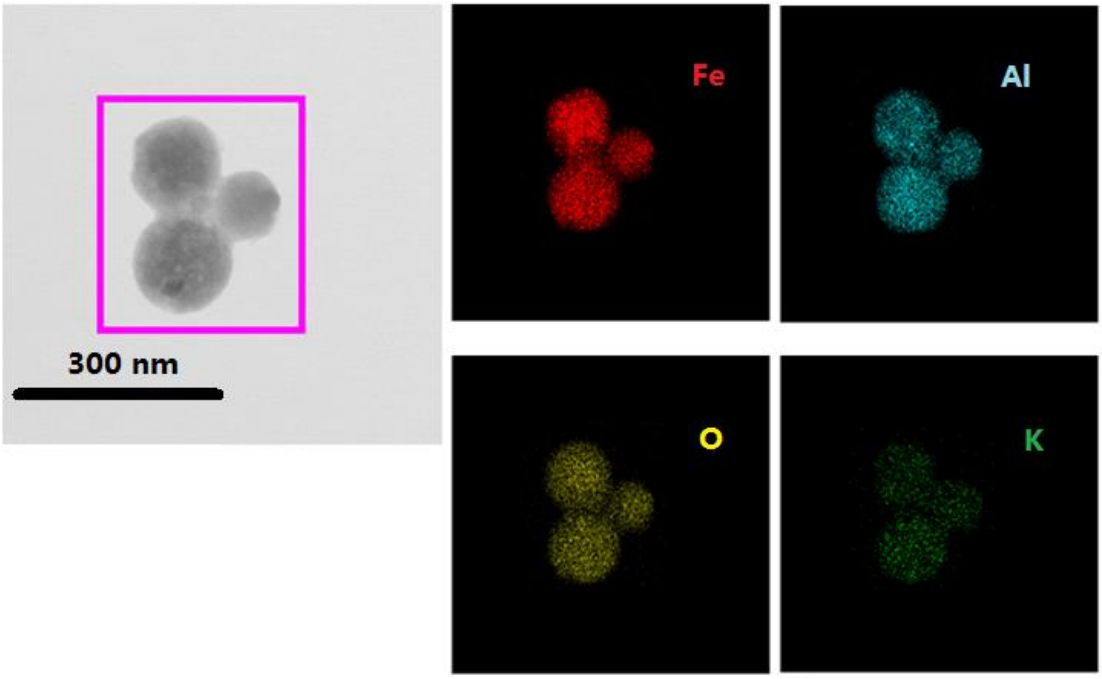

Figure 2.12. TEM and elemental mapping: 48.7 mol% Fe_2O_3/48.7 mol% Al_2O_3 with 2.6 mol% K after 50 CLC cycles at 1023 K.

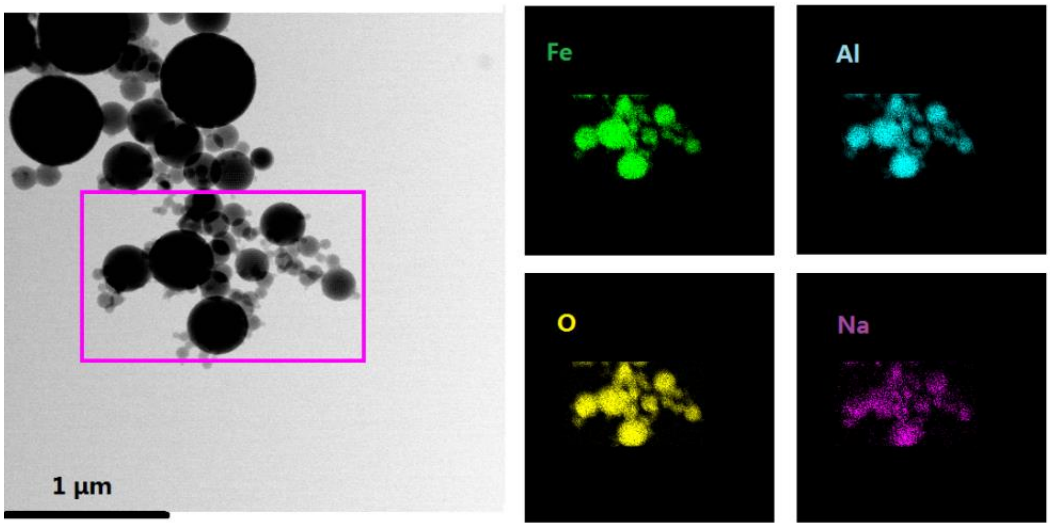

Figure 2.13. TEM Elementary Mapping result 2.6 % Na 48.7mol% Fe_2O_3/ 48.7mol% Al_2O_3 after 50 CLC cycles at 1023 K.

Our experimental approach is not amenable to identify the root cause of the potassium effect, however unlike a catalysis which is a pure surface effect, we are driving the OC within the whole particle, and thus we expect whatever the alkali metal effect it must involve more than surface effects. This may involve changing oxygen-ion transport within the lattice or a reduction in the oxygen binding energy. The fact that Na with its lower electronegativity performs worse is consistent with this, with the Cs, because of its instability within the lattice not providing any useful insights on this point. The stability of iron within the alumina implies that the alkali metal (both K and Na) stiffens the alumina matrix from moving around and offers a stable path for oxygen transport to the surface, which may help to explain the improved selectivity (i.e. reduction in coking).

2.4 Conclusion and Outlook

We demonstrate that addition of potassium to iron oxide nanoparticles during synthesis can significantly enhance its performance in long-term CLC tests of methane oxidation. This was however not true for Na or Cs addition. In the latter Cs addition was not incorporated within the lattice but was found to phase separate into small Cs particles at the surface of the iron oxide. Synthesis of particles with an alumina matrix was found to have minimal effect for nascent iron oxide performance, but when added in combination with potassium yielded the best performance in terms of long-term stability as well as CO_2 selectivity with respect to coking.

Chapter 3: Novel Support: Silicalite-1 zeolite for Fe-based Oxygen Carriers

3.1 Introduction

The capture of CO_2 released from fuel combustion is being actively studied to mitigate the effects of climate change.[4] A number of processes such as pre-combustion[6], oxy-fuel combustion and post-combustion[9] have been explored for CO_2 capture from fossil fuel combustion processes. However, all these techniques are energy intensive, resulting in a decrease of the overall combustion efficiency.

Chemical looping combustion (CLC) is being explored as a next generation combustion technology, since it operates with the same thermodynamic efficiency as air based combustion, but with a potential of near-zero CO_2 emission.[2,92] CLC involves a two-step process, in which metal oxides serve as the oxygen source rather than air so that the direct contact between fuel and air is avoided. Hydrocarbon fuels are oxidized by metal oxides to water steam and CO_2 in the first step, from which a pure CO_2 stream, could be realized by single steam condensation.[63,64] The reduced metal oxide is then regenerated by combustion in air in the second step to complete the combustion cycle. The isolation of hydrocarbon fuels from air in CLC processes achieves a pure CO_2 stream for direct sequestration in an ideal situation, and avoids NO_x formation by recovery of metal oxides at moderate temperature in air. Because of the multi-cycling nature of the process, the choice of metal oxides as oxygen carriers (OCs), with excellent activity, and long-term stability is critical to enabling

implementation of CLC into industrial scale.[8]

Metal oxides based on copper-, iron-, nickel-, manganese- *et al.,* as well as their mixtures are the most promising OC's candidates for CLC cycles because of their earth abundance, low cost, mechanical stability and recyclability.[24,8,68,38] Among them, Fe-based OCs have received intensive research efforts because of its low cost, high melting point and excellent mechanical strength at high temperature.[93] The practical application of iron oxide OCs in CLC, however, has been impeded by serious sintering and low reduction rate by fuels.[38,68,94] Eventually, the iron oxide OCs encounter agglomeration and deactivation and thus durability loss in multiple CLC cycles. The introduction of support materials for iron oxide OCs is being studied to conquer the durability and deactivation issues in CLC cycles. Currently, inert supports including Al_2O_3[95], SiO_2[66], $MgAl_2O_4$[26], TiO_2[37] and ZrO_2[70], CeO_2[96] and active supports such as perovskites[97] have been considered for Fe_2O_3 OCs. The support materials help to promote dispersion of OC particles and provide physical/chemical barriers against OC migration into aggregates. The interaction between support and OC can also facilitate the reduction rate of OCs for fuel combustion.[26] It should be noted that all these support materials are oxides and their mixtures.

In the present work, we report a new type of support, a silicalite-1 zeolite, for Fe_2O_3 OCs in CLC. Silicalite-1 is the aluminum-free form of zeolite, with a mordenite framework inverted (MFI) structure consisting of two intersected 10 member ring (MR) microporous channels, one straight and one sinusoidal, with diameter of ~0.55 nm.[98,99] Silicalite-1 is thermally stable (up to ~1550 K) and mechanically stable, making it a potential desired inert support for Fe_2O_3 to form

durable OCs in CLC, which, to our knowledge, has not yet been explored. In this study, two silicalite-1 supported Fe_2O_3 structures; a) core-shell Fe_2O_3@silicalite-1 and b) Fe_2O_3-impregnated silicalite-1 (Fe_2O_3/silicalite-1) were created for CLC and tested with methane fuel in a fixed bed reactor. The encapsulation of Fe_2O_3 inside silicalite-1 shell or within its channels provides physical barriers for avoiding aggregations of OCs during CLC cycling, while the unique microporous structure of zeolite allows transport of methane in and CO_2 out of Fe_2O_3 OC. An added benefit is we find that these structures reduce coke deposition on Fe_2O_3.

3.2 Experimental Section

3.2.1 Material synthesis

3.2.1.1 Preparation of core-shell Fe_2O_3@silicalite-1 OCs

Fe_2O_3 particles were prepared by dissolving 20.2 g of $Fe(NO_3)_3 \cdot 9H_2O$ (99.99% trace metals basis, Sigma-Aldrich) in 50 mL deionized (DI) water under rigorous stirring, followed by addition of 30 mL KOH ($\geqslant$85%, Sigma-Aldrich) solution (5 $mol \cdot L^{-1}$) to form a $Fe(OH)_3$ suspension.[100] After adjusting pH of the suspension to ~10 by drop wise addition of NH_4OH solution (28.0-30.0%, Sigma-Aldrich), the mixture was stirred for 0.5 h and then transferred to a Teflon-lined stainless steel autoclave and held at 453 K for 5 h. Finally, the sample was then filtrated, washed with DI water and ethanol alternatively four times, and dried at 343 K for 12 h to form Fe_2O_3 particles.

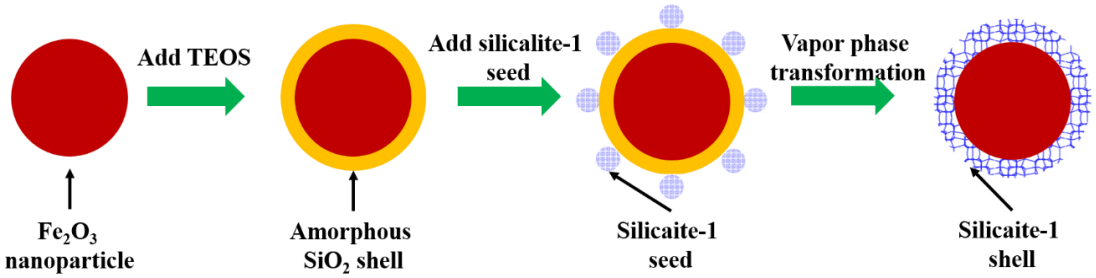

Scheme 3.1. Synthesis procedure to prepare Fe_2O_3@silicalite-1 OC.

Scheme 3.1 shows the procedure to prepare the Fe_2O_3@silicalite-1 core-shell structure with Fe_2O_3 as the core and silicalite-1 as the shell. First, a SiO_2 shell was created on Fe_2O_3 particles to form core-shell Fe_2O_3@SiO_2 structure. In this synthesis, 0.1 g as-synthesized Fe_2O_3 particles were firstly dispersed in a solution of 40 mL 2-propanol (99.5%, Sigma-Aldrich), 1.42 g DI water and 1.1 g NH_4OH solution (28.0-30.0%) by ultra-sonication for 1 h. Secondly, a SiO_2 precursor solution was prepared by mixing 1 g tetraethyl orthosilicate (TEOS) (98%, Sigma-Aldrich) with 2 mL 2-propanol and the resultant mixture was added into Fe_2O_3 suspension at a rate of 0.4 mL h^{-1} via a syringe pump (NE-1000, New Era Pump System). After stirring the mixture for 12 h, the resultant Fe_2O_3@SiO_2 particles were collected by centrifugation, washed with DI water four times, and then dried at 343 K overnight. Thirdly, a vapor phase transformation process was carried out to convert SiO_2 into silicalite-1 under assistance of silicalite-1 seeds to form the core-shell Fe_2O_3@silicalite-1 structure according to a previously reported method.[101,102] In this synthesis step, the as-prepared Fe_2O_3@SiO_2 particles were firstly dispersed in 4 mL DI water by ultrasonication. 2 g poly-(diallydimethylammonium chloride) (PDDA, 20 wt% in H_2O, Sigma-Aldrich) was mixed with 1 mL DI water and the resultant mixture was added into the Fe_2O_3@SiO_2 suspension. After the mixture was stirred for 0.5 h, the particles were centrifuged and washed with diluted NH_4OH (2 wt %) solution four times. The as-obtained wet paste was then dispersed in 10 mL 1 wt% zeolite seed suspension for 0.67 h. The mixture was finally collected by centrifugation, washed with DI water four times and then dried at 343 K overnight. The as-prepared Fe_2O_3@SiO_2 particles coated with PDDA and silicalite-1 seeds were transferred into

a glass vial, which was placed in a Teflon-lined stainless steel autoclave containing 2.0 g trimethylamine (99%, Sigma-Aldrich), 0.2 g ethylene diamine (99.5%, Sigma-Aldrich), and 0.4 mL DI water.[102] The autoclave was heated at 413 K for three days to transform amorphous SiO_2 shell into silicalite-1 shell. Finally, the sample was calcined at 823 K for 4 hours at a ramp rate 1 K min^{-1} under flowing air (100 mL min^{-1}, Airgas). The Fe_2O_3@silicalite-1 sample was designated as Fe_2O_3@Si.

For the synthesis of silicalite-1 seeds,[101] typically, 0.43 g NaOH (99%, Sigma-Aldrich) was dissolved in 15 mL DI water, followed by addition of 15 g tetrapropylammonium hydroxide aqueous solution (TPAOH, 40 wt%, Alfa-Aesar) and 9.5 g of fumed silica (Sigma-Aldrich). The mixture was stirred at room temperature for 0.25 h and then heated at 353 K under stirring until a clear mixture was obtained. The resultant clear mixture was placed in a Teflon-lined stainless steel autoclave, which was rotated at a speed of 30 rpm and under temperature of 403 K for 8h in a convection oven. Finally, the silicalite-1 nanoparticles were centrifuged and washed with DI water for 4 times and then dispersed in DI water to form 1 wt% silicalie-1 seed solution.

3.2.1.2 Preparation of Fe_2O_3/silicalite-1 composite

Silicalite-1 zeolite was synthesized by a hydrothermal method using a recipe of 1TPAOH: 8.5TEOS: 0.17NaOH: 34CH_3CH_2OH: 484H_2O. In a typical synthesis, 0.032 g NaOH was firstly dissolved in 20.2 g DI water, followed by addition of 1.22 g TPAOH (40wt%) aqueous solution. 4.25 g TEOS was added and then the resultant mixture was held under rigorous stirring at room temperature for 24 h. Finally,

crystallization of silicalite-1 zeolite was conducted for 2 days in the autoclaves tumbling vertically in an oven at 423 K. After crystallization, the zeolite product was centrifuged, washed with DI water till pH ~ 9, and dried at 343 K overnight. Afterwards, the zeolite sample was calcined at 823 K for 6 h with a ramp rate at 1 K min^{-1} under flowing air (100 mL min^{-1}).

The synthesis of Fe_2O_3/silicalite-1 composite was done by an impregnation method. Typically, 0.35 g of $Fe(NO_3)_3$ was dissolved in 0.2 g DI water and the resultant aqueous solution was added to 1 g silicalite-1 dropwise under rigorous stirring to form the 12 wt% Fe_2O_3/silicalite-1 sample. The process was repeated to make the 24 wt% Fe_2O_3/silicalite-1, in which 0.70 g of $Fe(NO_3)_3$ was used. The as-prepared 12 wt% Fe_2O_3/silicalite-1 and 24 wt% Fe_2O_3/silicalite-1 were dried at 393 K overnight, followed by calcination at 823 K for 4 h with a ramp rate of 1.67 K min^{-1} under air flow (100 mL min^{-1}). We designate the 12 wt% Fe_2O_3/silicalite-1 and 24 wt% Fe_2O_3/silicalite-1 as Fe_2O_3/Si-12 and Fe_2O_3/Si-24, respectively.

3.2.2 Characterizations

The morphologies of the zeolite supported Fe_2O_3 OC samples were characterized by scanning electron microscopy (SEM, Hitachi SU-70) and transmission electron microscopy (TEM, JEOL JEM 2100 FEG). The porosity, pore size, and surface area of these samples were obtained by argon (Ar) adsorption-desorption isotherms measured at 87 K with an Autosorb-iQ analyzer (Quantachrome Instruments). Crystal structures of OCs were characterized by X-Ray diffraction (XRD) with a Bruker Smart1000 under Cu Kα beam. Fe and Si contents of the samples were determined by

inductively coupled plasma optical emission spectroscopy (ICP-OES, Optima 4300 DV instrument, Perkin-Elmer).

The cyclability and reactivity of OCs with CH_4 as fuel was carried out in a vertically oriented fixed bed reactor in an electrically heated isothermal furnace, as reported in a previous publication.[94] Mass flow controllers (MFC, MKS) regulated by a Labview VI program were utilized for gas reactant flow rate control. The reactor effluent was characterized by an online mass spectrometer (Stanford Research UGA 300) operating with a mass resolution < 0.5, atomic mass unit (a.m.u.), at 10 % of peak height and a detection limit < 1 ppm. Ar was used as an inert internal standard to determine the volume change of gaseous reactants and products during the reaction so as to assign concentrations. By varying the flow rates of CH_4 and O_2 with a fixed Ar flow rate at 200 mL min^{-1}, calibrations for the mass spectrometer were obtained for CO_2, CO, CH_4 and H_2. About 200 mg of OC was used for each test, and for the supported OCs, samples containing this amount of Fe_2O_3 were used. The powders were packed within a quartz reactor tube of 610 mm length, with outer diameter (O.D.) 12.5 mm and inner diameter (I.D.) 10 mm, as described in our previous work.[94] The particles were first annealed at 1023 K for 1 hour, and then exposed alternatively to 11% methane for 2 min, and 20% oxygen for 5 min simulating the CLC reaction cycles with argon as the inert balance gas. Argon was introduced for 5 min during the shift from methane to oxygen to avoid direct contact between oxygen and methane. The CLC tests were run continuously for 50 cycles, up to 15 h.

3.3 Results and discussion

3.3.1 Structural properties of OCs

SEM and TEM images in Figure 3.1 show the morphologies of synthesized core-shell Fe_2O_3@Si and Fe_2O_3/Si composite OCs. Fe_2O_3@Si consists of uniform spherical particles of diameter at ~ 1 μm (Figure 3.1a). The thickness of the silicalite-1 shell is ~ 100 nm and the Fe_2O_3 core has a diameter of ~ 900 nm (Figure 3.1b). Figure 3.1c) and 3.1e) are SEM images of Fe_2O_3/Si-12 and Fe_2O_3/Si-24, respectively, and both samples show a typical coffin-like morphology of silicalite-1, indicating that the loading of Fe_2O_3 and subsequent calcination did not change the morphology of the silicalite-1 support. Moreover, a comparison between the Fe_2O_3/Si-12 and Fe_2O_3/Si-24 samples (as evidenced by TEM images in Figure 3.1d) and 3.1f) indicates that there are more debris-like particle aggregates on the silicalite-1 in Fe_2O_3/Si-24 than Fe_2O_3/Si-12, which can be attributed to the high loading of Fe_2O_3 in Fe_2O_3/Si-24.

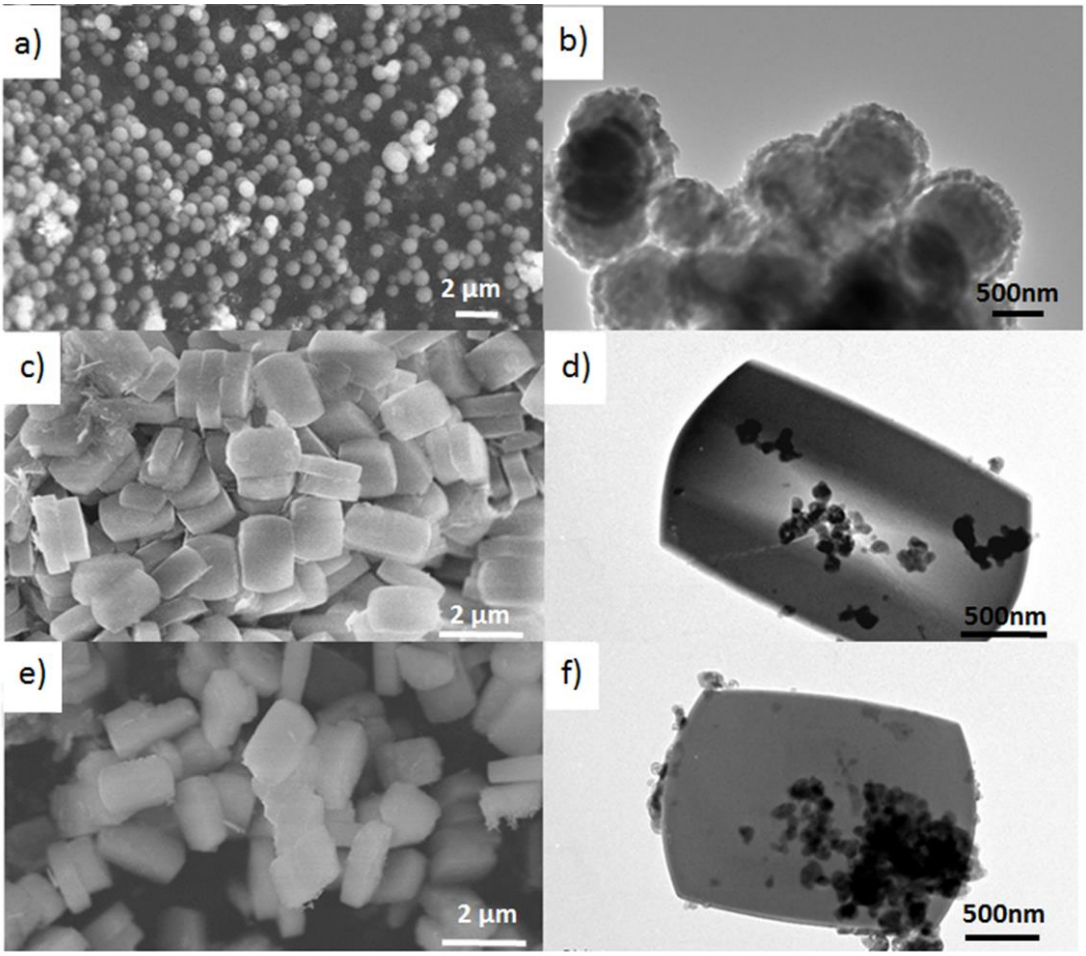

Figure 3.1. Morphology of OC samples viewed by SEM images of a) Fe_2O_3@Si, c) Fe_2O_3e/Si-12, and e) Fe_2O_3/Si-24, and TEM images of b) Fe_2O_3@Si, d) Fe_2O_3/Si-12, and f) Fe_2O_3/Si-24, respectively.

The XRD patterns in Figure 3.2 identify the existence of both Fe_2O_3 and silicalite-1 crystalline phases in these three OC samples. For comparison purpose, the XRD patterns of silicalite-1 and Fe_2O_3, respectively, are included in Figure 3.2. Apparently, Fe_2O_3@Si contains the characteristic peaks of both hematite Fe_2O_3 ($2\theta = 33°$, 35° and 54°) and silicalite-1 ($2\theta = 23°$ and 24°), confirming the existence of silicalite-1 and Fe_2O_3 in this sample, consistent with morphology observation in Figure 3.1. XRD patterns of Fe_2O_3/Si-12 and Fe_2O_3/Si-24 in Figure 3.2 show the characteristic peaks of silicalite-1, consistent with the silicalite-1 crystal viewed in Figure 3.1. The intensity of diffraction peaks corresponding to Fe_2O_3 in Fe_2O_3/Si-12 is much smaller than that in Fe_2O_3/Si-24, which can be ascribed to the lower loading of Fe_2O_3 OCs in the former sample.

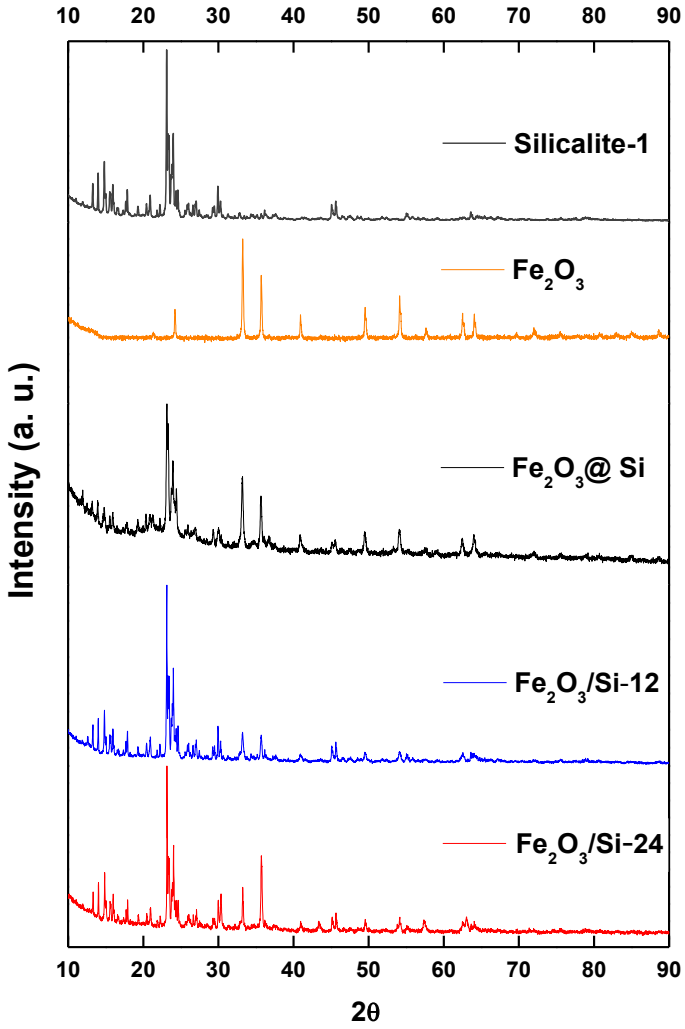

Figure 3.2. XRD patterns of silicalite-1, Fe_2O_3 and silicalite-1 supported OCs.

3.3.2 Composition and porosity of OCs

The concentrations of Fe_2O_3 in the OC samples were measured by ICP-OES, as summarized in Table 3.1. The weight percentage of Fe_2O_3 in Fe_2O_3/Si-12 and Fe_2O_3/Si-24 were 11 wt% and 24 wt%, respectively, same as the Fe_2O_3 concentrations used in the sample preparation recipe. The concentration of Fe_2O_3 in the Fe_2O_3@Si core-shell sample is 22 wt%, comparable to that in Fe_2O_3/Si-24.

Table 3.1. Textual properties and elemental compositions of the OCs.

OC	$f\_Fe_2O_3$[a]	S_{total}[b]	V_{total}[c]	V_{micro}[d]	V_{meso}[e]
	%	(m^2 g^{-1})	(cm^3 g^{-1})	(cm^3 g^{-1})	(cm^3 g^{-1})
Fe_2O_3@Si	21	178	0.107	0.044	0.063
Silicalite-1	NA	396	0.208	0.113	0.093
Fe_2O_3/Si-12	11	360	0.196	0.110	0.086
Fe_2O_3/Si-24	24	309	0.161	0.100	0.061

[a] Determined by ICP-OES; [b] Calculated from multi-point BET method; [c] Calculated from the adsorption branch at P/P_0=0.95; [d] Calculated from *t-plot* method; [e] V_{meso}= V_{total}-V_{micro}.

Ar adsorption-desorption isotherms in Figure 3.3 are used to characterize the porosity of silicalite-1, Fe_2O_3/Si-12, Fe_2O_3/Si-24 and Fe_2O_3@Si samples. At the low relative pressure ($p/p_0 < 0.05$), the Ar uptake follows the order of Fe_2O_3/Si-24 < Fe_2O_3/Si-12< silicalite-1, implying that the microporosity of silicalite-1 decreases with the increase of Fe_2O_3 loading. Fe_2O_3@Si (22 wt%) and Fe_2O_3/Si-24 (24 wt%) have similar Fe_2O_3 loadings, but the former sample has much lower Ar uptake and thus microporosity. The low Ar uptake in Fe_2O_3@Si sample might result from the existence of a portion of amorphous SiO_2 or not-well-crystallized zeolite in the silicalite-1 shell.

The pore size distributions of the OC samples are shown in Figure 3.3b, which are derived from the adsorption branch of the Ar ad-/desorption isotherms using non-local density functional theory (NLDFT) method.[103] The intensity of the micropore peaks, centered at ~5 Å, shows the trend of silicalite-1> Fe_2O_3/Si-12> Fe_2O_3/Si-24, consistent with the Ar isotherm data in Figure 3.3a), indicating that high Fe_2O_3 loading leads to more Fe_2O_3 loading in the microporous channels of silicalite-1. The Fe_2O_3@Si sample has the lowest micropore peak intensity, which might be due to the amorphous SiO_2, or not-well-crystallized silicalite-1, as discussed above. The second peak located at 8 Å might be due to the reminiscence of a phase transition in Ar adsorbate according to previous reports.[104,105,106,107] The intensity of the mesopore peak in all OCs is very low, which suggests the absence of mesoporosity in these zeolite-supported OC samples.

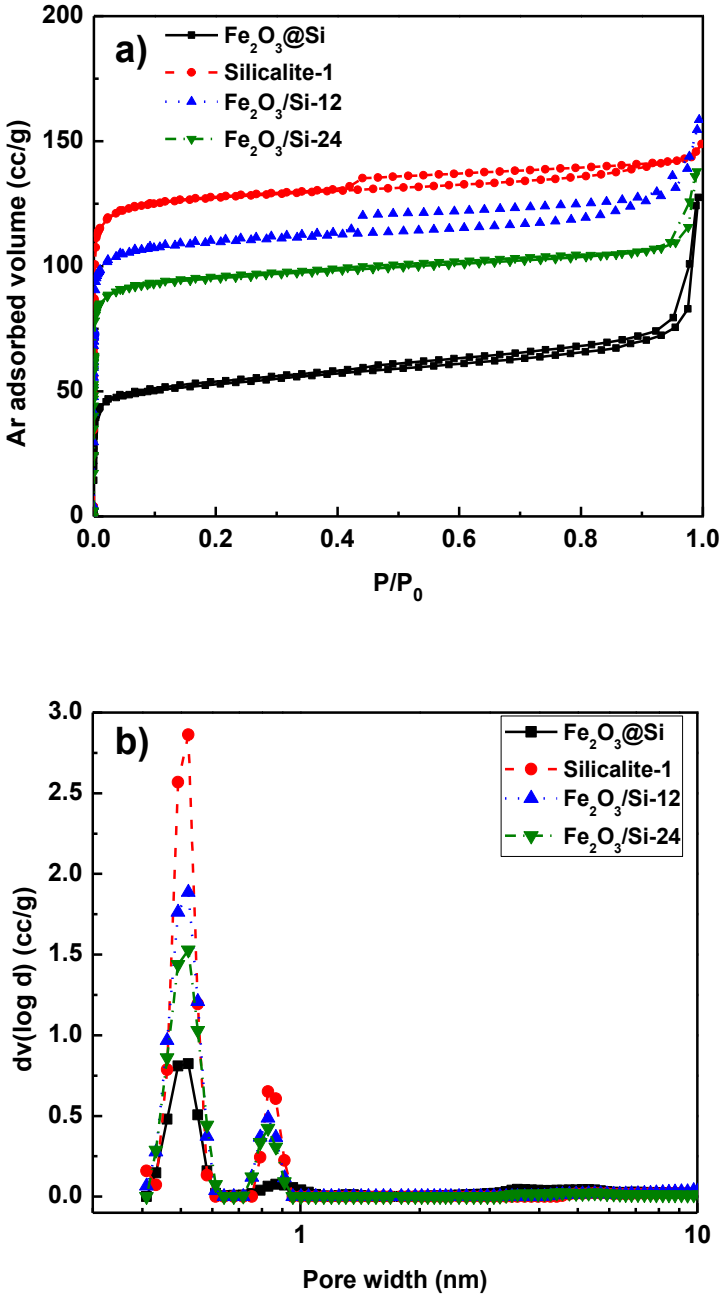

Figure 3.3. a) Ar ad-/desorption isotherms of OCs and b) NLDFT pore size distributions of OCs derived from the adsorption branch of their Ar ad-/desorption isotherms.

3.3.3 OC performance tests in CLC

Table 3.2 lists the possible reactions occurring in different reduction stages of the CLC tests with Fe_2O_3 OCs and methane fuel. The CO_2 yield in each reaction is computed according to the equation stoichiometry.

Table 3.2. Reaction equations in different reduction stages of CLC and corresponding CO_2 yields.

	Reaction Equation	**CO_2 yield (mmol/g_Fe_2O_3)**
(1)	$\frac{1}{4}CH_4 + 3Fe_2O_3 \rightarrow 2Fe_3O_4 + \frac{1}{4}CO_2 + \frac{1}{2}H_2O$	0.52
(2)	$\frac{1}{4}CH_4 + Fe_2O_3 \rightarrow 2FeO + \frac{1}{4}CO_2 + \frac{1}{2}H_2O$	1.56
(3)	$\frac{3}{4}CH_4 + Fe_2O_3 \rightarrow 2Fe + \frac{3}{4}CO_2 + \frac{3}{2}H_2O$	4.69

Our measured CO_2 yield stabilized at 0.52 mmol/g-Fe_2O_3 for all OC samples at both 1023 K and 1223 K for a 50 cycle CLC test, as shown in Figure 3.4. The CO_2 yield suggests that all OC samples did methane conversion preferentially following the first reaction equation in Table 3.2, which means Fe_2O_3 is reduced into Fe_3O_4 phase. The XRD patterns in Figure 3.5 show the existence of Fe_3O_4 in the OC samples after the CLC test, which is consistent with the conclusion that Fe_2O_3 reduced to Fe_3O_4 in the CH_4 reduction step drawn from CO_2 yield data in Figure 3.4. The silicalite-1 support did not influence the reaction nature of Fe_2O_3 OCs in the CLC tests, which is consistent with the chemical and thermal inertness of silicalite-1 zeolite in the CLC conditions. The consistence in CO_2 yield across all these CLC 50 cycles, up to 15 hours, indicates that all OCs were stable and did not experience obvious activity degradation. Additionally, Figure 3.4 shows the reaction temperature does not influence the reaction nature of the Fe_2O_3 OCs in the tested CLC conditions.

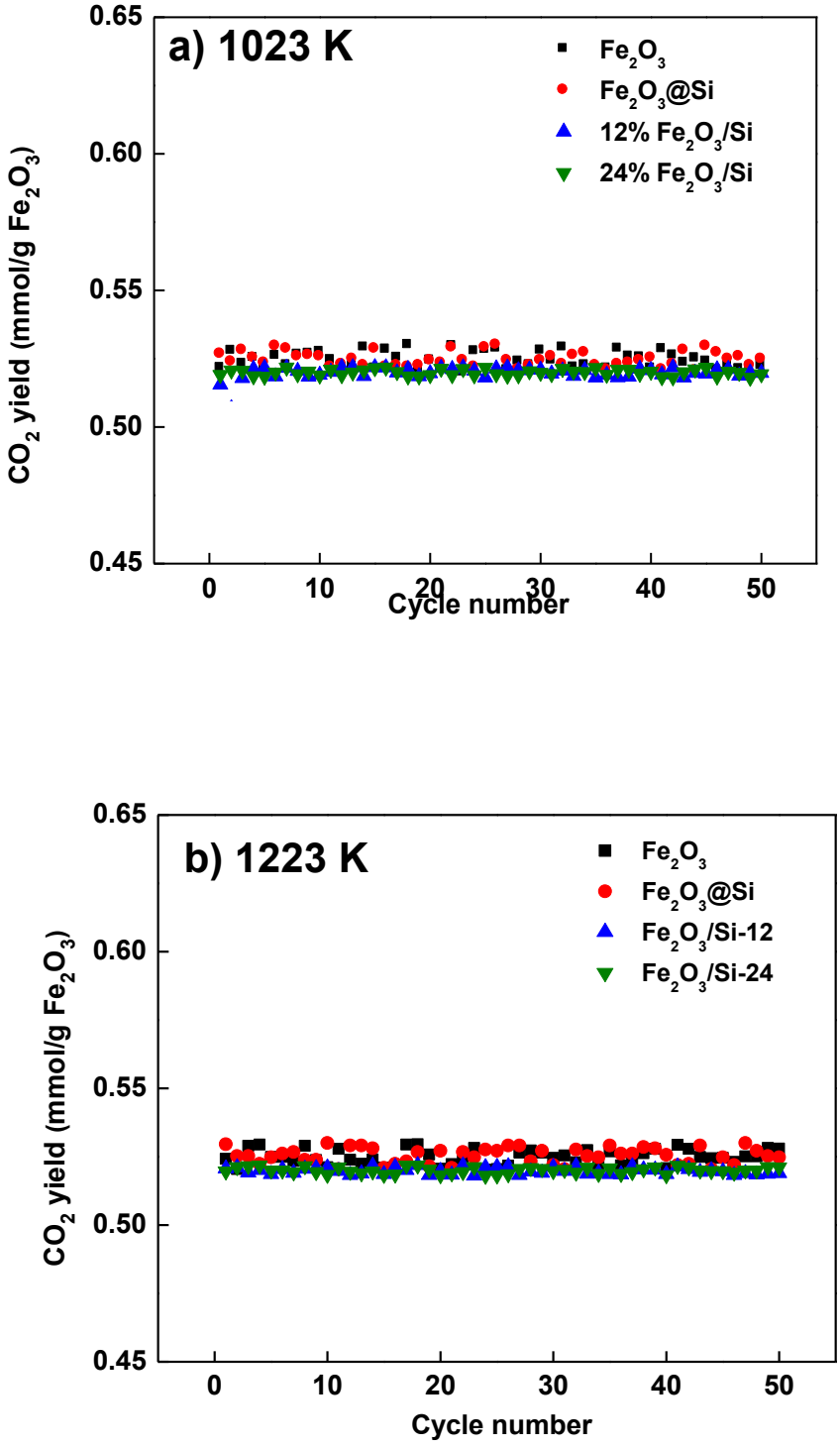

Figure 3.4. CO_2 yield in CH_4 step at a) 1023K and b) 1223K of Fe_2O_3, Fe_2O_3@Si, Fe_2O_3 /Si-12, Fe_2O_3 /Si-24 during 50 cycle CLC reaction.

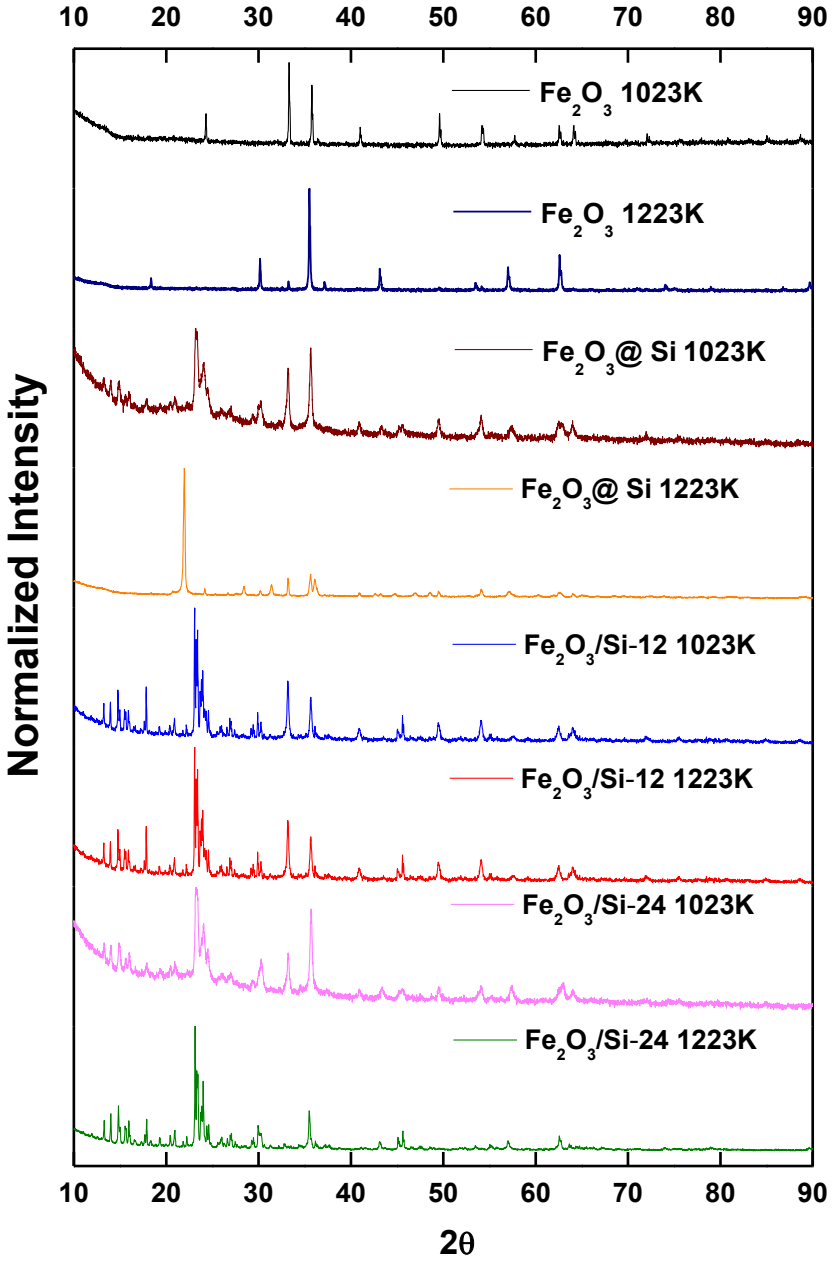

Figure 3.5. XRD patterns of Fe_2O_3 and silicalite-1 supported Fe_2O_3 OCs after 50 cycle CLC reaction tests.

Since the primary motivation of developing CLC process is for CO_2 sequestion, the exclusive formation of CO_2 versus other by-products such as coke (C) from methane fuel over OCs in the reaction is desired. In the present study, we did not observe any other geseous carbon-based product except CO_2 in the reduction stage of OCs. In the regeneration (or oxidation) stage of OCs, CO_2 product was also observed, which results from the combustion of coke species deposited on OCs during the reduction stage in the CLC tests. Addtionaly, H_2 product was detected in the reduction stage of OCs.

It is noted that two nominal side reactions, Boudouard reaction (3.1) and methane decomposition (3.2), could occur in CLC of methane fuel.[85]

$$2CO \rightarrow C + CO_2 \quad (3.1)$$

$$CH_4 \rightarrow C + 2H_2 \quad (3.2)$$

The thermodynamic analysis shows that the methane decomposition reaction is endothermic while the Boudouard reaction is exothermic. Therefore, the methane decomposition reaction is thermodynamically preferred at high temperature reaction conditions while the Boudouard reaction is favored at low temperatures.[39] The absence of CO product and presence of H_2 in the reduction stage of the CLC test indicate that methane decomposition is the side reaction in our study. Thus, the selectivity of CO_2 (γ_{CO2}) is analyzed based on the ratio of CO_2 amount (n_{CO2}) to total carbon-based species (i.e., the summation of n_{CO2} and the amount of C (n_C)) in the reduction stage, as shown in equation (3.3). It should be noted that coke generated from the methane decomposition during the reduction step will subsequently be

oxidized to CO_2 during the OC regeneration step (the O_2 oxidation step). The amount of coke was quantitied based on the CO_2 emission from the oxidation step .

$$\gamma_{CO_2}=\frac{n_{CO_2}}{n_C+n_{CO_2}} \qquad (3.3)$$

Figure 3.6 reveals CO_2 selectivity in CLC tests over Fe_2O_3 and silicalite-1 supported Fe_2O_3 OCs at two different tempreatures. At 1023 K (Figure 3.6a), all the supported OCs (Fe_2O_3@Si, Fe_2O_3/Si-12 and Fe_2O_3/Si-24) showed similar CO_2 selectivity, ~97% and was slightly higher than bare Fe_2O_3 OCs that had a CO_2 selectivity of ~95%. When the temperature was raised to 1223 K (Figure 3.6b), significant differences in CO_2 selectivity across these four OC samples were observed. The bare Fe_2O_3 OC only had a selectivity of ~ 65%. The Fe_2O_3@Si had a better performance than bare Fe_2O_3, showing a selectivity of ~ 87%, but much less than Fe_2O_3/Si-12 and Fe_2O_3 /Si-24 OCs. As shown in Figure 3.6b, both Fe_2O_3/Si-12 and Fe_2O_3 /Si-24 had minimal performance degradation in the reduction stage, with a selectivity ~ 95%. The slight differences in CO_2 selectivity at relatively lower temperature (1023 K) and significant differences at higher temperature (1223 K) across these four OC samples suggest higher reaction temperature may change the structures of the OC samples, and thus alters their selectivity in the CLC reaction. Apparently, the Fe_2O_3-impregnated silicalite-1 samples have the best stability than others in the CLC tests.

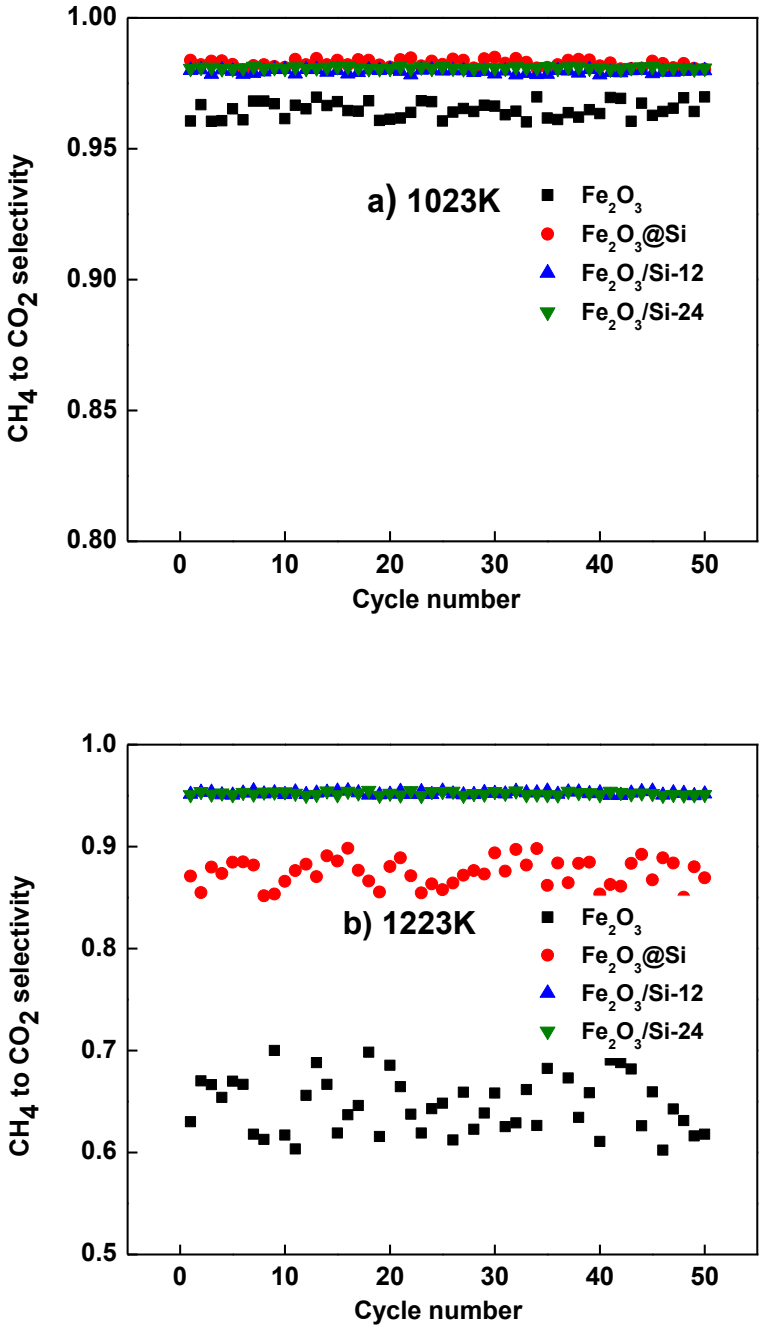

Figure 3.6. CH_4 to CO_2 selectivity, γ_{CO_2}, at a) 1023K and b) 1223K over Fe_2O_3, Fe_2O_3@Si, Fe_2O_3/Si-12 and Fe_2O_3/Si-24 samples during 50 cycle CLC reaction.

To further understand the CO_2 selectivity at different temperatures over these OC samples discussed above, we monitored the temporal evolution of CO_2 and H_2 in

the reduction step of CLC process (shown in Figure 3.7). In the CO_2 evolution profile at 1023 K shown in Figure 3.7a, the CO_2 yield initially increased with the reduction time, reached a maximum, and then decreased. The peaking of CO_2 signal for reaction over the silicalite-1 supported Fe_2O_3 OCs emerged earlier than the bare Fe_2O_3 OC sample. This is due to the large particle size of bare Fe_2O_3 without any zeolite support, which causes sluggish reaction kinetics compared to the reaction over smaller Fe_2O_3 particle sizes in the silicalite-1 supported Fe_2O_3 OCs.[94,95,66] At higher reaction temperature (1223 K), the emergence of the maxima in CO_2 evolution profile over every sample is earlier than that at 1023 K, suggesting the reaction rate is facilitated due to the increase in reaction temperature. But again, the peaking of the CO_2 signal for reaction over the bare Fe_2O_3 lagged behind all other silicalite-1 supported Fe_2O_3 OCs. It should be noted that the CO_2 peak area resulted from reaction over every OC sample or every tested temperature is the same. This is consistent with the total yield of CO_2 was independent of the temperature or OC sample, as evidenced in Figure 3.5 above.

For the evolution profiles of H_2 in the CLC tests (shown in Figure 3.7b), all OCs showed nearly zero H_2 production at 1023 K, indicating the insignificant methane decomposition to form coke during CLC reaction, consistent with the selectivity data presented in Figure 3.6a. At reaction temperature of 1223 K, the H_2 evolution profile of bare Fe_2O_3 exhibited a pronounced H_2 peak, followed by the medium sized peak from Fe_2O_3@Si sample and invisible peak from Fe_2O_3/Si-24 and Fe_2O_3/Si-12. The emergence of H_2 signal in the CLC tests indicates coke was being formed from methane decomposition reaction. Quite clearly, the resistance to coking in the CLC

tests at 1223 K follows the sequence of Fe_2O_3/Si-24 ~ Fe_2O_3/Si-12 > Fe_2O_3@Si >> Fe_2O_3. This analysis fits well with the conclusion drawn from CO_2 selectivity data illustrated in Figure 3.6b. It is worth noting that H_2 production does not occur concurrently with CO_2 evolution, and instead, behind the CO_2 formation. This scenario indicates that the side reaction, methane decomposition, is strongly promoted when the labile framework oxygen in OCs is mostly consumed by the reduction of CH_4 to CO_2 at high temperatures. The zeolite support apparently helps the Fe_2O_3 OCs limit this side reaction, and thus promote the CO_2 selectivity in the CLC process.

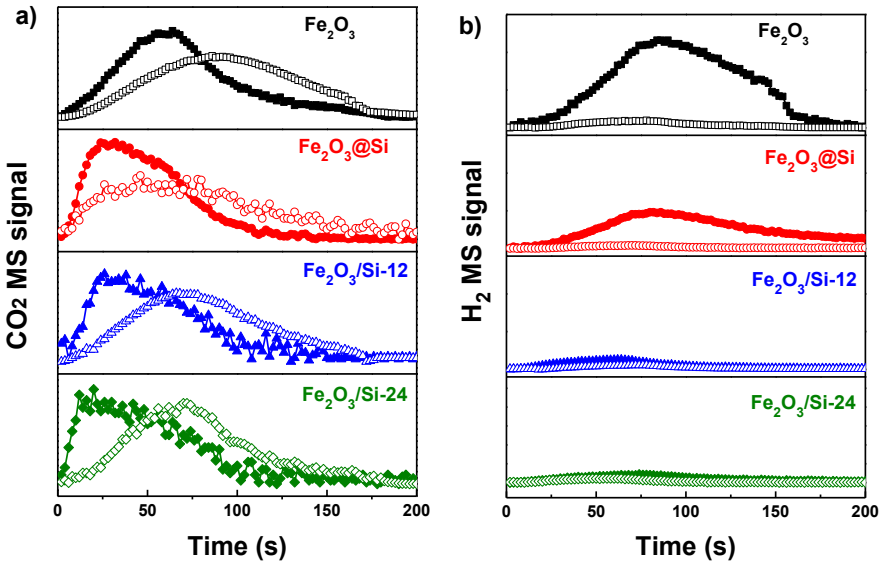

Figure 3.7. The evolution profile of CO_2 a) and H_2 b) in the reduction step during the 30th CLC cycle at 1023 K (open symbol) and 1223 K (filled symbol) for all OCs.

To examine the morphological structure of OCs after high temperature CLC reaction, SEM observation and XRD measurements were conducted on the used OC samples. Figure 3.8a, c, e and g) show SEM images of the four OC samples after 50 cycle CLC at 1023 K. In comparison with the morphology of silicalite-1 supported Fe_2O_3 samples before CLC tests (Figure 3.1), the Fe_2O_3@Si particles lost their smooth surface feature in the core-shell structure, but still kept the spherical morphology. The Fe_2O_3/Si-12 and Fe_2O_3/Si-24 samples, however, have quite similar morphologies to those before CLC tests. The XRD patterns in Figure 3.5 confirmed the crystalline phase integrity of four OCs after reaction at 1023 K, since all of them do not have new peaks in the diffraction patterns. These data confirms that all the OCs can reserve their structural and chemical reactivity features at 1023 K in the CLC reactions.

Figure 3.8b, d, f and h show the morphologies of all investigated OCs after 50 cycle CLC at 1223 K. Both unsupported Fe_2O_3 and Fe_2O_3@Si seem to be sintered together to form large aggregates (Figure 3.8b and d, respectively). Particularly, the XRD patterns in Figure 3.5 indicate the the transofrmation of silicalite-1 into amorphous SiO_2, consistent with the SEM observation on these two OC samples. The sintering of silicalite-1 shell of the Fe_2O_3@Si particles might be due to the low structural crystallinity of the silicalite-1 shell (~ 100 nm thick), which is vulnerable to and prone to collapse at high temperature. Figure 8f and h illustrate that Fe_2O_3/Si-12 and Fe_2O_3/Si-24 have little morphological change after 50 cycles of CLC reaction at 1223 K. The XRD results in Figure 3.5 further confirm the presence of silicalite-1 zeolite phase in the samples after CLC tests. Compared to the thin silicalite-1 shell in

the Fe_2O_3@Si, the excellent structural stability of Fe_2O_3/silicailte-1 OCs should be ascribed to the large (~1 μm) and well-crystallized silicalite-1 crystals. Overall, the stable silicalite-1 zeolite provided physical barriers to avoid aggregation of active Fe_2O_3 OCs in CLC cycles, limited the coke deposition from side methane decomposition reaction, and thus led to high CO_2 selectivity in CLC of methane fuel.

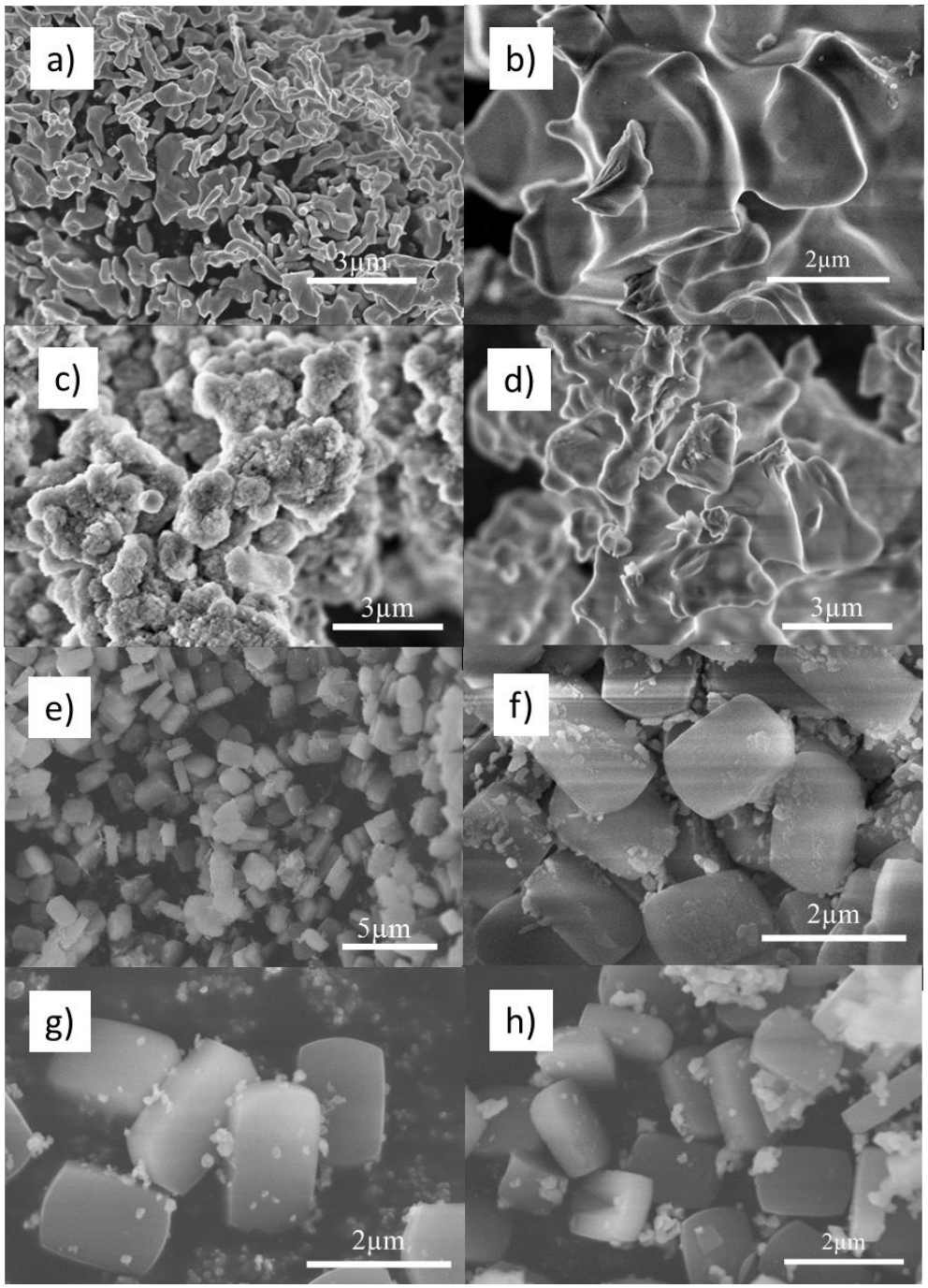

Figure 3.8. SEM images of the OCs (a) and (b): Fe_2O_3, (c) and (d): Fe_2O_3@Si, (e) and (f): Fe_2O_3/Si-12 and (g) and (h): Fe_2O_3/Si-24 after 50 cycle CLC reaction at 1023 and 1223 K, respectively.

3.4 Conclusion

Silicalite-1 is explored as a novel support material for Fe_2O_3 to form supported OCs for CLC reaction with methane as the fuel. Two silicalite-1 supported Fe_2O_3 structures, core-shell Fe_2O_3@silicalite-1 and Fe_2O_3-impregnated silicalite-1 (Fe_2O_3/silicalite-1), were created to study their influences on CLC reaction at 1023 and 1223 K, respectively. After 50 cycles of CLC tests at 1023 K, both Fe_2O_3@silicalite-1 and Fe_2O_3/silicalite-1 OCs showed similar CO_2 yield and slightly higher CO_2 selectivity than bare Fe_2O_3 OCs. All the OC samples were able to preserve their structural integrity at 1023 K. An increase of reaction temperature to 1223 K resulted in significant sintering of bare Fe_2O_3 and Fe_2O_3@silicalite-1 OCs, and thus they showed inferior CO_2 selectivity than that of Fe_2O_3/silicalite-1 OCs. The larger silicalite-1 crystal in Fe_2O_3/silicalite-1 OCs keeps its structural integrity and provides physical barriers for Fe_2O_3 OCs against aggregation and coke deposition in CLC cycles. In conclusion, our study of the structure-function relation for silicalite-1 supported Fe_2O_3 OCs can form the basis for the development of silicalite-1 as an efficient support in chemical looping applications.

Chapter 4: Perovskite Oxides as Oxygen Carriers

4.1 Introduction

Chemical looping combustion (CLC) is a novel approach towards the combustion of fuels that utilizes a two-step redox process to achieve carbonaceous combustion, offering a smaller carbon footprint with no thermodynamic energy penalty.[108,2] Instead of directly burning hydrocarbon in air, metal oxides are used as oxygen carriers (OC's) in the fuel reactor where they are reduced while carbonaceous fuel is converted to carbon dioxide and water. The reduced OC's are regenerated in an air reactor, and through cycling these oxides, a flameless combustion is achieved with the temperature in air reactors often lower than 1300 K, thus avoiding NO_x formation that is generated from traditional combustion with air (~80% N_2).[65] The resultant process under ideal conditions generates a pure CO_2 stream, after steam condensation in the fuel reactor.

One of the significant roadblocks in implementation of CLC is finding the right OC, and the multiple considerations include high phase stability, redox activity, low cost, and being environmentally benign.[24] Potential candidates studied as OC's include binary oxides of first row transition metals, such as iron, copper, nickel, manganese, cobalt, and their mixed metal oxides. Perovskites have also been explored as novel OC's considering their high redox

cyclic stabilities and superior oxygen transport capacities.[32b] Perovskites are generally formularized as ABO_3, with *A* and *B* cations and the O^{2-} anion and are natural candidates for OC's due to their high oxygen conductivity, thermal stability, ease of synthesis, and relatively low cost. In the perovskite structure, the *A* cation is typically an alkali, alkaline earth, or lanthanide metal, and the *B* cation a transition metal. Nevertheless, given the myriad of potential combinations of the *A* and *B* cations, choosing the optimal perovskite for CLC applications is daunting.[33]

The role of the transition metal *B* is more important than that of *A* considering that it is the redox active metal that participates in the CLC reactions. Therefore, we have conducted a systematic study of 9 different $La_{1-x}Ca_xBO_3$ compositions where the *B* site was varied between Cr to Cu. Furthermore, we included $Ba_{0.5}Sr_{0.5}Co_{0.8}Fe_{0.2}O_3$ (BSCF) since it is a commonly used material in oxygen evolution catalysis. In this communication, we report trends of particular materials descriptors such as electronegativity versus our independent variable oxygen storage capacity (OSC) with CH_4 as the fuel. Our goal is to find various descriptors that could be utilized by future studies to select the optimal oxides for various CLC applications.

4.2 Experimental Approach

4.2.1 Perovskite OC synthesis

All perovskites were synthesized in our laboratory using aerosol-assisted spray pyrolysis with metal nitrate aqueous solutions as precursors. All chemicals were

purchased from Sigma-Aldrich, including $La(NO_3)_3 \cdot 6H_2O$ (≥99.0% pure), $Ca(NO_3)_3 \cdot 4H_2O$ (≥99.0% pure), $Mn(NO_3)_2 \cdot 4H_2O$ (≥97.0% pure), $Fe(NO_3)_3 \cdot 9H_2O$ (≥98% pure), $Ni(NO_3)_2 \cdot 6H_2O$ (≥97.0% pure), $Co(NO_3)_2 \cdot 6H_2O$ (≥98% pure), $Cu(NO_3)_2 \cdot 3H_2O$ (≥98% pure), $Cr(NO_3)_3 \cdot 9H_2O$ (≥98% pure), $Ba(NO_3)_2 \cdot 9H_2O$ (≥98% pure) and $Sr(NO_3)_2 \cdot 9H_2O$ (≥99% pure).

The spray pyrolysis system consists of a stainless steel atomizer, silica-gel diffusion dryer, an isothermal tube furnace, and a stainless steel sample collector, as described in details in previous publications.[80] The synthetic process can be described as a droplet-to-particle method, where the precursor droplets are decomposed into perovskite mixed metal oxides in the isothermal furnace during the thermal treatment. For the precursor solution, 0.20 M metal nitrates, 0.10 M citrate acid are dissolved in DI water. The atomizer is a collision-type nebulizer, which generates droplets with diameters approximately 1 μm in size. The precursor droplets were carried by compressed air gas with a flow rate of ~3 L/min into the diffusion dryer, then into the isothermal tube furnace at 1273 K to decompose the precursors into oxide particles with a ~1s residence time. Finally, particles exiting the aerosol reactor are collected on a 0.4 μm DTTP Millipore filter with 10%-20% porosity (purchased from EMD Millipore).

4.2.2 Material Characterizations

Crystal structures of OCs are characterized by X-Ray Diffraction (XRD) with a Bruker Smart1000 detector using Cu Kα radiation. Transmission Electron Microscopy (TEM) and High Resolution Transmission Electron Microscopy (HRTEM) are performed using a Field Emission Transmission Electron Microscope

(JEOL 2100 FE-TEM). Scanning Electron Microscopy (SEM) results are obtained by Hitachi SU-70 SEM. TGA (Thermal Gravimetric Analyzer) coupled MS (Mass spectroscopy) tests were conducted simultaneously in a SDT Q600 coupled with Discovery TM quadruple mass spectrometer from TA instruments, with an alumina sample crucible loaded with ~10 mg samples. Samples were first heated to 150 K to and held for 30 min then ramped at 10 K min^{-1} to 1023 K and held for 30 min.

4.2.3 Fixed bed reactor reactivity test

Total methane oxidation and stability tests of the perovskites were performed in a vertically oriented fixed bed reactor placed in an electrically heated isothermal furnace at 1023 K. The effluent was sampled with a mass spectrometer (Stanford Research UGA 300) with a mass resolution of <0.5 atomic mass units (amu) at 10% of peak height and a detection limit <1 ppm. Argon was also used as an internal mass spectrometer standard for quantitative analysis of the effluent gases, and Ar flow rate were kept at a fixed value. By varying the flow rates of CH_4 and O_2 with a fixed Ar flow rate, calibrations of the mass spectrometer for different gases with different concentrations, including CO_2, CO, CH_4, H_2.

Nominally, a ~200 mg oxygen carrier sample is used for each test. The quartz flow reactor has a length of 61 cm, with a 1 cm inner diameter. The particles are first annealed at the reaction temperature for 1 hour, and then exposed alternatively to 11% methane for 2 min and 20% oxygen for 5 min simulating the CLC reactor. Argon is introduced for 300 s after each period, to purge the reactor and avoid oxygen and

methane mixing between the oxidation and reduction cycles. We achieved 50 cycles in this test as our previous study.

4.3 Results and Discussion

4.3.1 Textual properties of OCs

The Scanning Electron Microscopy (SEM) images of Figure 4.1 a) and 4.1 b) shows the spherical morphology of our spray pyrolysis synthesized $LaCrO_3$, while X-Ray diffraction (XRD) in Figure 4.2 confirms perovskite crystal structure. All samples were pseudocubic perovskites with Le Bail refinement performed in either the cubic (*Pm*-3*m*), orthorhombic (*Pbnm*), or rhombohedral (*R*-3*c*) space groups.

Powder X-ray Diffraction (XRD) experiments, performed on a Bruker D8 diffractometer with Cu Kα radiation, were used to characterize the as-synthesized materials, as shown in Figure 4.2. Table 4.1 presents the refined space group, crystallite size, and lattice parameters resulting from Le Bail fitting for each pattern. All refinements were performed with the TOPAS 4.2 software.[109] While most samples could be adequately fit in the cubic space group and therefore should be considered pseudocubic, final refinements were performed in either cubic (*Pm*-3*m*), orthorhombic (*Pbnm*), or rhombohedral (*R*-3*c*) space groups depending on the presence of peak splitting and satellite peaks. Each sample had a crystallite size smaller than 35 nm, determined by the Scherrer equation, as expected with this synthesis technique. The exceptions were $LaMn_{0.5}Ni_{0.5}O_3$ and $Ba_{0.5}Sr_{0.5}Co_{0.8}Fe_{0.2}O_3$ which had crystallite sizes of 77.8(5) and 66.3(4) nm, respectively. Each sample was phase pure except for $LaMn_{0.5}Cu_{0.5}O_3$, $LaCoO_3$, and $La_{0.5}Ca_{0.5}CoO_3$. $LaCoO_3$ and $La_{0.5}Ca_{0.5}CoO_3$ both had a weak and broad peak at approximately 28.5° 2θ

(approximately 3.0 Å). This peak could be attributed to La_2O_3, however, it is not possible to definitively identify this phase as there are no other impurity peaks present at higher angles in the XRD patterns. For $LaMn_{0.5}Cu_{0.5}O_3$ there are impurity peaks present at approximately 29.5° and 35.5° 2θ (approximately 3.0 and 2.5 Å, respectively). The peak at 29.5° 2θ can possibly be attributed to La_2O_3 or Cu_2O and the peak at 35.5° 2θ to CuO. As with the previous samples, the lack of additional impurity peaks makes the definitive identification of these phases impossible. Other phases considered but ruled out include calcium oxide and carbonate, binary metal oxides, the metallic elements, and all oxygen deficient perovskite based phases present in the ICDD PDF-2 database. More crystallite info could be found in table 4.1.

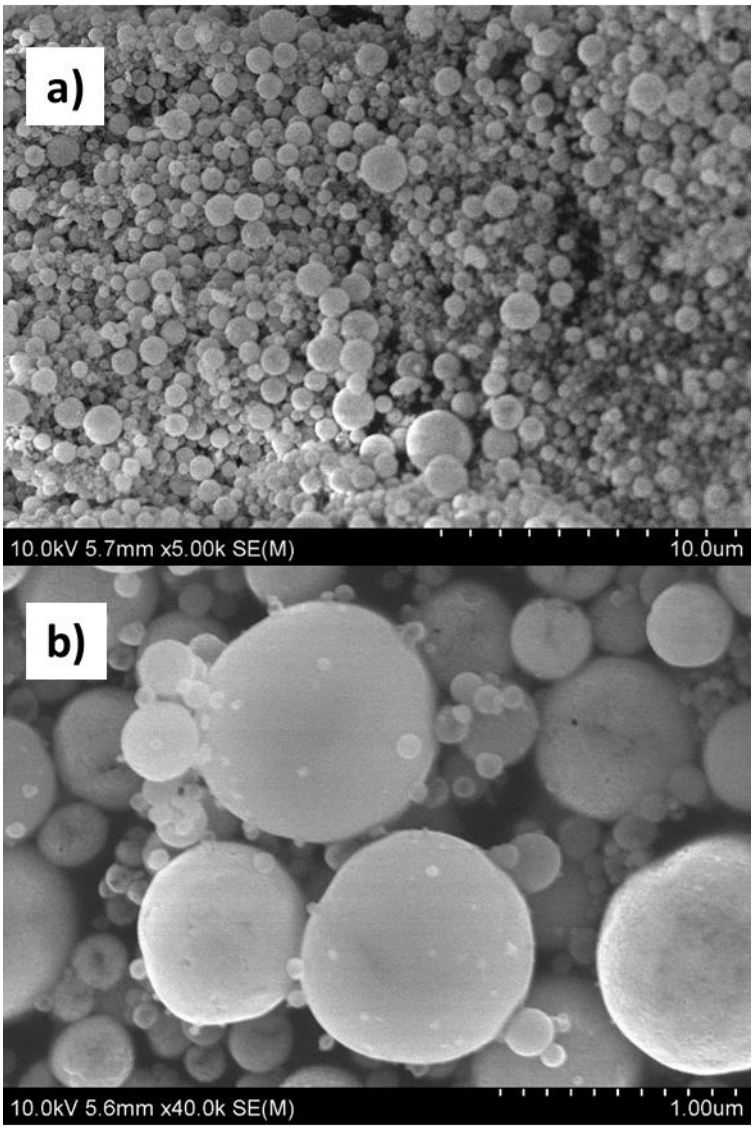

Figure 4.1. SEM of $LaCrO_3$ a) and b) shows the spherical morphology.

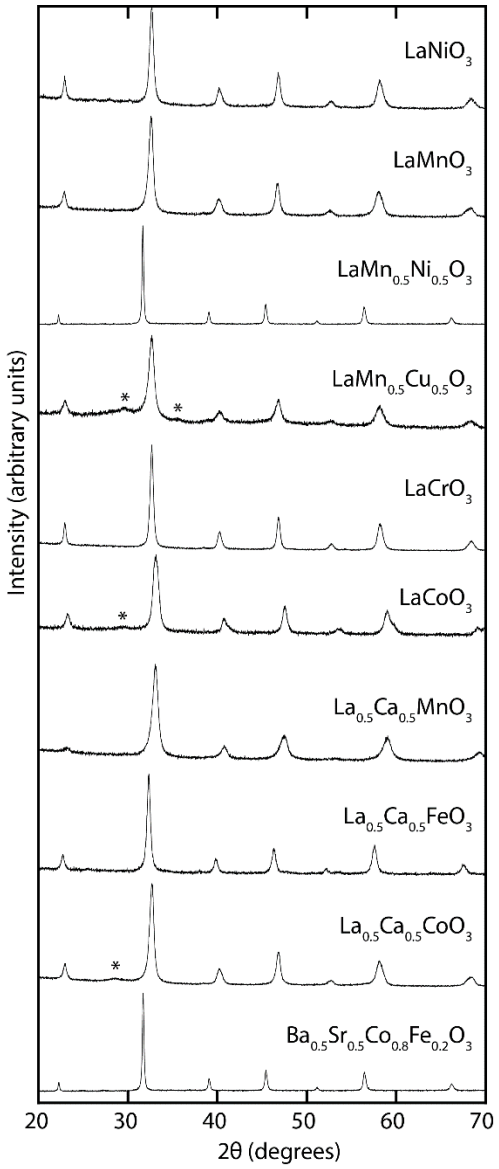

Figure 4.2. Powder XRD patterns for each of the tested samples.

Table 4.1. Le Bail refinement results for as synthesized samples.

			Lattice parameters			
	Phase Symmetry	**Crystallite size (nm)[a]**	**a (Å)**	**b (Å)**	**c (Å)**	**Volume (Å³)**
$LaNiO_3$	rhombohedral (*R*-3*c*)	25.4(2)	5.5058(4)		13.372(1)	351.13(6)
$LaMnO_3$	rhombohedral (*R*-3*c*)	20.1(1)	5.5190(4)		13.396(1)	353.37(7)
$LaMn_{0.5}Ni_{0.5}O_3$	rhombohedral (*R*-3*c*)	77.8(5)	5.6407(2)		13.8478(5)	381.80(3)
$LaMn_{0.5}Cu_{0.5}O_3$	cubic (*Pm*-3*m*)	13.1(1)	3.8888(7)			58.81(3)
$LaCrO_3$	orthorhombic (*Pbnm*)	34.3(2)	5.4695(3)	5.5177(3)	7.7598(5)	234.13(2)
$LaCoO_3$	rhombohedral (*R*-3*c*)	20.4(1)	5.4365(5)		13.130(2)	336.08(8)
$La_{0.5}Ca_{0.5}MnO_3$	cubic (*Pm*-3*m*)	12.7(1)	3.8376(4)			56.52(2)
$La_{0.5}Ca_{0.5}FeO_3$	orthorhombic (*Pbnm*)	25.6(2)	5.537(1)	5.571(1)	7.8556(5)	242.30(7)
$La_{0.5}Ca_{0.5}CoO_3$	rhombohedral (*R*-3*c*)	21.5(1)	5.4816(4)		13.535(1)	352.21(6)
$Ba_{0.5}Sr_{0.5}Co_{0.8}Fe_{0.2}O_3$	cubic (*Pm*-3*m*)	66.3(4)	3.9927(1)			63.652(5)

[a] determined from the Scherrer equation

The post reaction $La_{0.5}Ca_{0.5}CoO_3$ TEM image is shown in Figure 4.3a) and HRTEM in Figure 4.3c). From Figure 4.3c), with a lattice spacing of 0.98 nm, while the selected area electron diffraction (SAED) in Figure 4.3d) verifies the (101) orientation in the cubic perovskite. SEM images in figure 4.3b) of post-reaction material indicates that sintering has taken place, although as will be discussed later this does not seem to impede performance over multiple cycles, consistent also with observation by others.[110] HRTEM lattice image in Figure 4.3c) indicates that due to the 15 hours of high temperature operation, significant crystal growth is occurring as seen by the narrowing of the XRD spectral peaks of post-reaction samples in Figure 4.4.

Each of these XRD patterns is provided in Figure 4.3 of the Le Bailing fitting of each pattern showed that each sample was phase pure with all peaks being indexed in either the cubic (*Pm*-3*m*), orthorhombic (*Pbnm*), or rhombohedral (*R*-3*c*) space groups. Representative Le Bail refinements for $La_{0.5}Ca_{0.5}CoO_3$, $LaCu_{0.5}Mn_{0.5}O_3$, and $LaNiO_3$ are provided in Figures 4.5-4.7. Table 4.2 presents the refined space group, crystallite size, and lattice parameters resulting from the Le Bail fitting of each pattern. Considering impurity phases are no longer present in the post fixed bed experiment samples and that the OSC of these samples is steady over the 50 cycles tested, these impurity phases appear to have a minimal effect on the performance of these samples as oxygen carriers. All peaks were indexed in either the cubic (*Pm*-3*m*), orthorhombic (*Pbnm*), or rhombohedral (*R*-3*c*) space groups. TGA-MS data in Figure 4.8 implies that our perovskites did not release O_2 up to 1023 K, thus the OCs' reaction with CH_4 follows the gas-solid reaction mechanism.

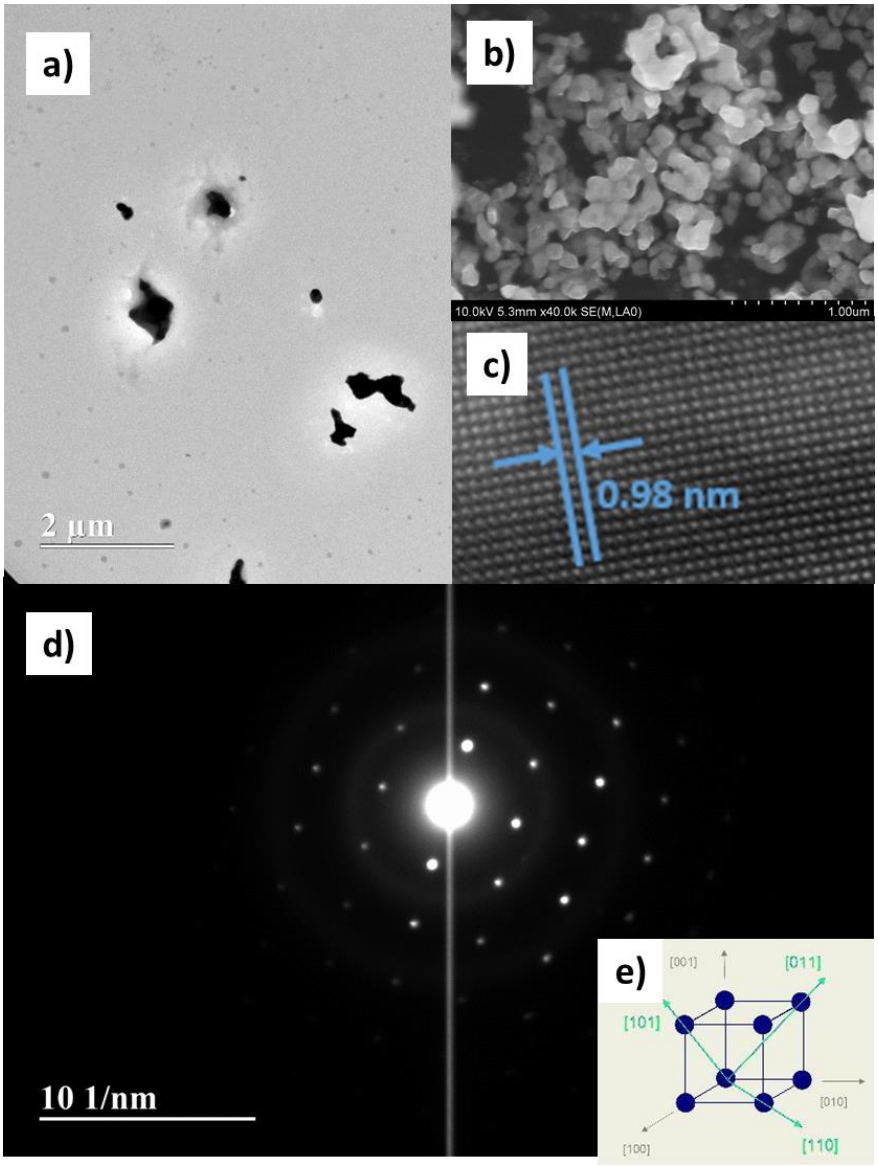

Figure 4.3. a) TEM, b) SEM and c) HRTEM and d) SAED shows the perovskite crystal structure of the post-reaction $La_{0.5}Ca_{0.5}CoO_3$.

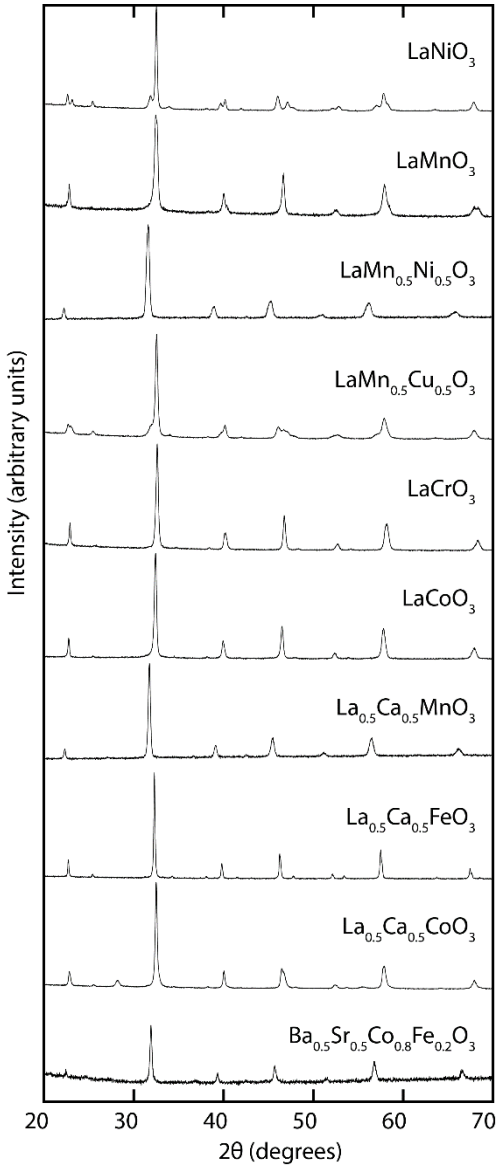

Figure 4.4. Powder XRD of post fixed bed reactor study samples.

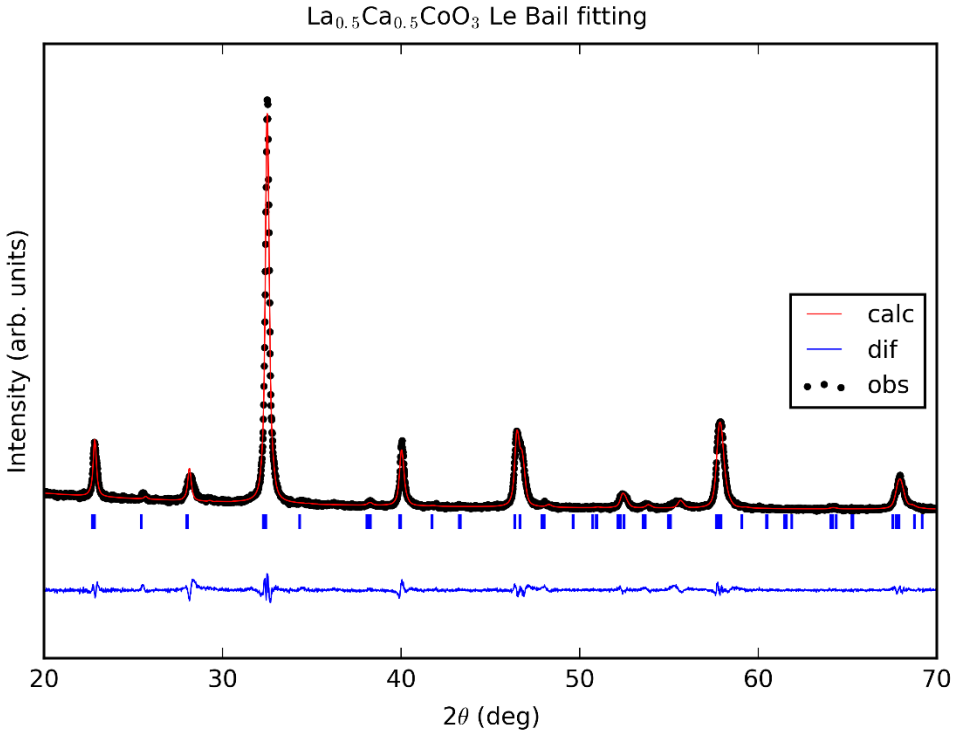

Figure 4.5. Le Bail fitting of $La_{0.5}Ca_{0.5}CoO_3$ in the orthorhombic *Pnma* space group. Shown are the observed (black circles), refined (red line), difference (blue line) and locations of allowed reflections (blue tick marks).

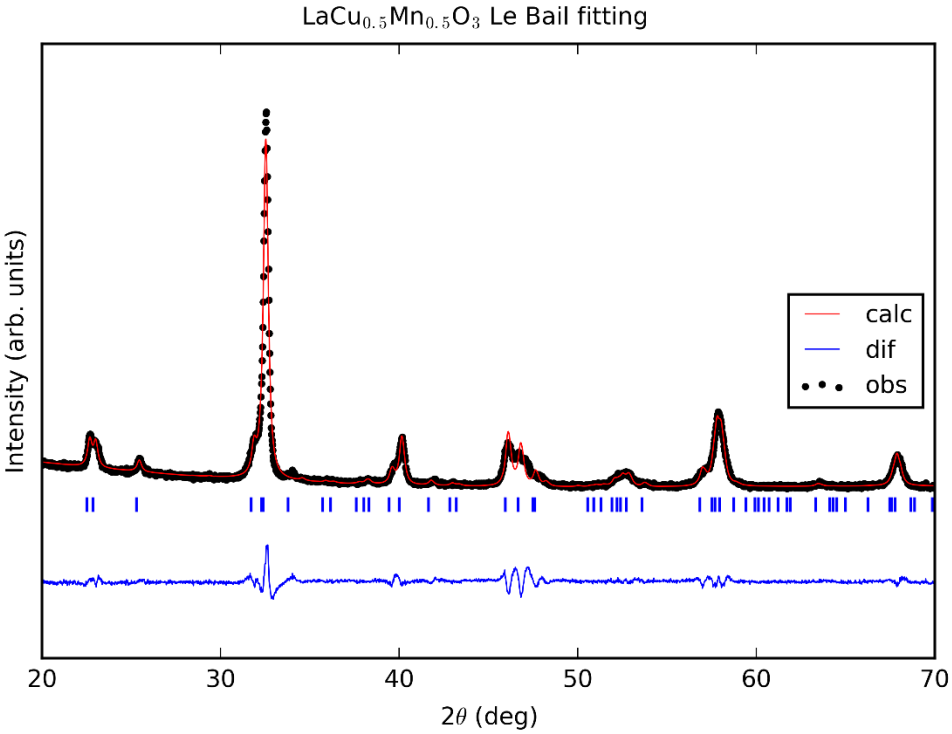

Figure 4.6. Le Bail fitting of $LaCu_{0.5}Mn_{0.5}O_3$ in the orthorhombic *Pbnm* space group. Shown are the observed (black circles), refined (red line), difference (blue line) and locations of allowed reflections (blue tick marks).

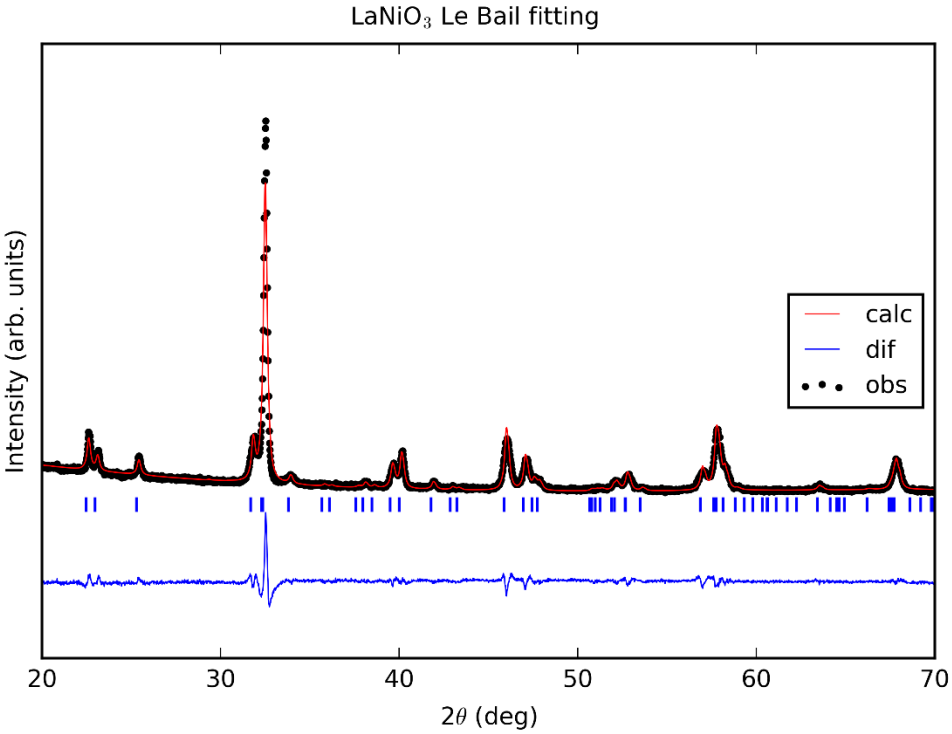

Figure 4.7. Le Bail fitting of $LaNiO_3$ in the orthorhombic *Pbnm* space group. Shown are the observed (black circles), refined (red line), difference (blue line) and locations of allowed reflections (blue tick marks).

Table 4.2. Le Bail refinement results for samples post fixed bed reactor studies.

			Lattice parameters			
	Phase Symmetry	**Crystallite size (nm)[a]**	**a (Å)**	**b (Å)**	**c (Å)**	**Volume (Å³)**
$LaNiO_3$	orthorhombic (*Pbnm*)	57.8(5)	5.5394(4)	5.6513(3)	7.7449(4)	242.45(3)
$LaMnO_3$	rhombohedral (*R*-3*c*)	38.8(4)	5.5193(3)		13.402(1)	353.56(5)
$LaMn_{0.5}Ni_{0.5}O_3$	rhombohedral (*R*-3*c*)	48.1(5)	5.7053(5)		13.870(1)	390.96(7)
$LaMn_{0.5}Cu_{0.5}O_3$	orthorhombic (*Pbnm*)	38.1(3)	5.5260(4)	5.6385(5)	7.7792(6)	242.39(3)
$LaCrO_3$	orthorhombic (*Pbnm*)	67.3(5)	5.5149(2)	5.4776(2)	7.7610(4)	234.45(2)
$LaCoO_3$	orthorhombic (*Pbnm*)	63.6(5)	5.5072(3)	5.5361(2)	7.7941(4)	237.62(2)
$La_{0.5}Ca_{0.5}MnO_3$	orthorhombic (*Pbnm*)	70.6(8)	5.6727(3)	5.6513(4)	7.9691(5)	255.47(3)
$La_{0.5}Ca_{0.5}FeO_3$	orthorhombic (*Pbnm*)	136(1)	5.5646(2)	5.5539(2)	7.8519(2)	242.67(1)
$La_{0.5}Ca_{0.5}CoO_3$	orthorhombic (*Pnma*)	58(1)	5.5384(7)	5.5467(5)	7.7779(5)	238.94(4)
$Ba_{0.5}Sr_{0.5}Co_{0.8}Fe_{0.2}O_3$	cubic (*Pm*-3*m*)	53.7(8)	3.9763(3)			62.87(2)

[a] determined from the Scherrer equation

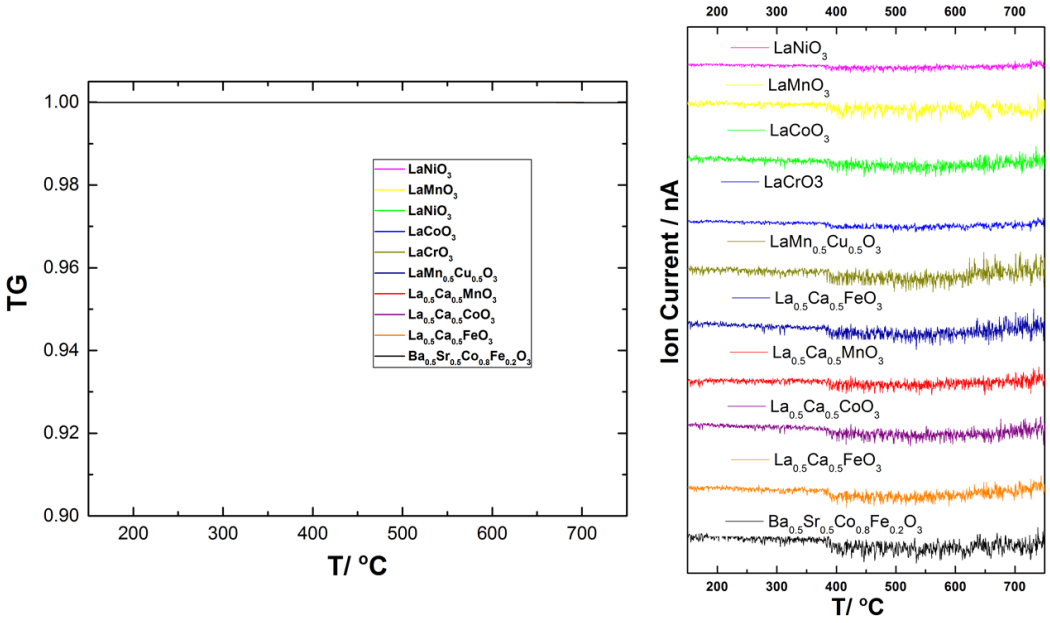

Figure 4.8. TGA-MS of as-synthesized perovskites with m/z=32 ion current displayed (All mass loss curves superimposed on top of one another).

4.3.2 OC performance tests

In this study, we found that *A* cation substitution has a negligible effect on OSC, but there exists an inverted volcano dependence for transferable oxygen during total methane oxidation with the *B* cation's electronegativity (Pauling scale). The global reaction between perovskite and methane can be represented as,

$$4\ ABO_3 + \delta\ CH_4 \rightarrow 4\ ABO_{3-\delta} + \delta\ CO_2 + 2\delta\ H_2O$$

Thus we can define oxygen storage capacity (OSC) in CLC as δ, which was measured by quantitative analysis of CO_2 in the fuel step. Figure 4.9a) shows the OSC (δ) over 50 CLC cycles in the fixed bed reactor and clearly indicates that all perovskites are stable OCs. The amount of CO_2 produced was quantified from the effluent in the fuel step, and carbon coking generated from methane thermal decomposition, the major side reaction, is measured by the CO_2 species in the air step. Shown in Figure 4.9b), we define CO_2 selectivity as:

$$\gamma_{CO_2} = \frac{n_{CO_2}}{n_C + n_{CO_2}}$$

where n_{CO2} are the number of moles detected in the fuel step and n_C the number of moles detected in the air step. All the perovskites expressed γ_{CO2} values higher than 95%, indicating their low coking ratio.[111]

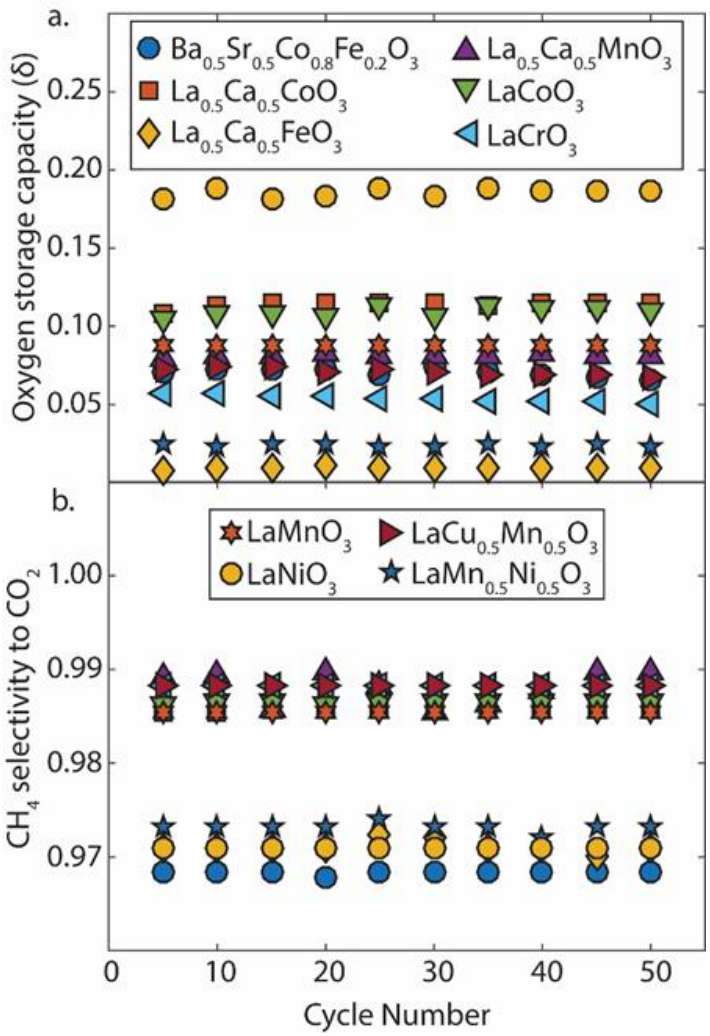

Figure 4.9. (a) OSC (δ) and (b) CH_4 selectivity to CO_2 of tested perovskites in 50 cycles with methane at 1023 K in a fixed-bed reactor.

In an attempt to provide some microscopic structural context to these results we show in Figure 4.10(a) the relationship between OSC and λ_B (*B* site electronegativity) on the Pauling Scale.[112] For the mixed *B* site samples, a simple molar average was used for λ_B. The resulting plot shows an inverted volcano behavior. Since the OSC's of the samples with mixed La and Ca occupancy on the *A* site showed negligible difference, we concluded that substituting Ca for La on the *A* site has a negligible effect of the OSC, which agrees with previous publications.[113,114,115,46a] This also makes sense considering that the *B* metal is the redox active center of the perovskite. For comparison, we also plotted the average occupancy of the so-called e_g orbital for the transition metal, as determined by Suntivich *et al.*,[113b] versus OSC in Figure 4.10b). Although true O_h symmetry is not present in all of these materials, the structural distortions are too minor to invert the basic crystal field splitting energies (i.e. make t_{2g}-derived states higher in energy than the e_g-derived ones). Therefore, we use e_g only as a convenient label across various perovskites in searching for broad trends in properties such as catalytic activity or oxygen storage capacity. In cases where two transition metals are present, only the more catalytically active element was considered. Here, the trend appears less obvious than for λ_B, although a volcano-type relationship does seem plausible. Overall, e_g occupancy does not appear to be as useful a descriptor as *B*-site electronegativity.

Utilizing a materials descriptor such as electronegativity provides a general understanding of OC design with ABO_3 perovskites given that the

underlying mechanisms are still unknown. Past studies have found that oxygen transport and mobility in perovskite structures are highly relevant to their other applications, thus considerable attention has been focused on partial substitutions for the *A* and *B* sites to find optimal combinations.[116,32a] Recently, Imanieh *et al.* explored the effect of substituted atom size on the reactivity of hydrocarbons with ABO_3 ($CaMnO_3$) perovskites in order to identify the optimal OC for CLC applications.[117] At high reaction temperature (>1123 K) favoring O_2 release, $CaMnO_3$ perovskite with ~10% Sr and Fe doped in the *A* and *B* sites, respectively, helps improve their oxygen storage capacity (OSC) due to higher crystalline distortion. X. Dai *et al.* found that compared to Nd, Eu substitution for La on the *A* site maintains a relatively high catalytic activity and structural stability during redox reactions.[118]

Since Bockris and Otagawa's work in 1980s, descriptors correlating 5-coordinate surface ions' electronic properties of perovskite oxides and their activities towards oxygen electrocatalysis have attracted a lot of interest.[113a] It has been reported that the filling of e_g manifold of the octahedral crystal field of the *B* cations, mainly related to the oxygen binding to the perovskite surface[13], can be used as an efficient descriptor for reactivity in oxygen evolution reaction (OER) in fuel cell applications employing perovskites[113b] and water-splitting reactions.[114] Thus e_g in perovskite, contributed to occupied valence band states, are responsible for the reactive states near Fermi level, could be used as an effective descriptor, consistent with Norskov's d-band theory. From our own

results, however, it appears that e_g occupancy is not as relevant for temperature-driven redox reactions.

The role of B-site electronegativity could be related to that of the B-O bond strength. Electronegativity, as defined by Mulliken, is the average of the ionization potential and the electron affinity. Therefore, the degree of hybridization between the *B d*-states and the O 2*p*-states would be dependent on electronegativity.

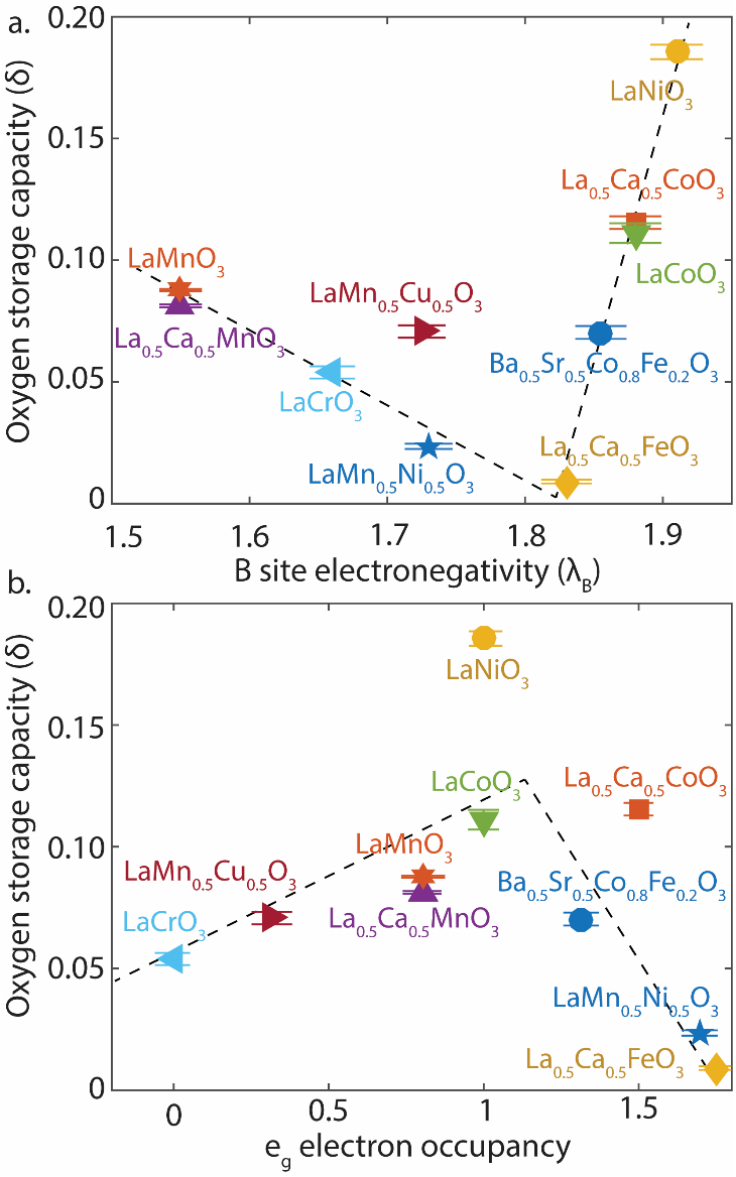

Figure 4.10. The relation of OSC (δ) and (a) the λ_B (B site electronegativity) in methane total oxidation and (b) the e_g electron occupancy.

While we have not found a direct correlation between electronegativity and oxide conductivity yet, other workers have found oxygen vacancy formation as a useful descriptor for electrochemical applications of perovskite oxides. Kitchin *et al.* used density function theory (DFT) calculations to correlate the decrease in the oxygen vacancy formation energy to increasing atomic numbers from Cr to Cu in La*B*O_3 and Sr*B*O_3, which were explored as anode materials in SOFC's.[119] Through DFT calculations, Carter *et al.* demonstrated that ion diffusion in the $La_{1-x}Sr_xBO_3$ family (*B* = Cr, Mn, Fe, Co) and $Sr_2Fe_{2-x}Mo_xO_6$ depends on two processes: oxygen vacancy formation and vacancy mediated oxygen migration, and found that oxygen vacancy formation energy could be used as a descriptor for oxide ion transport properties' evaluation.[116]

Yang *et al.* utilized X-ray Absorption Near Edge Structure (XANES) and fluorescence O K-edge to study the effects of the *B* and *A* site, respectively, on the electronic structure and found that changes in *A* site substitution have less of an effect relative to the *B*-site, and increasing the *B* site electron count can increase hybridization between the transition metal 3*d* and oxygen 2*p* states and therefore covalency.[115] Hong *et al.* reported that partial substitution of the *B* site could result in improved catalytic effects owing to lattice defects.[120] As to the reaction of perovskites with hydrocarbons, the activation of the C-H bond has been proposed to be important.[32a] For example, the reaction of oxides with methane can follow two pathways, the 4-centered (CH_3-B—H-O) transition state (σ-bond metathesis) and 3-centered (CH_3-B-H) transition state (dehydrogenation).[111,121] However, our studies are

not mechanistic in nature and we cannot propose any of these transition states in our oxides during CLC.

On the left side of the inverted plot (Figure 2a), the downward trend in the oxygen storage capacity includes *B* cations with relative low electronegativity. As the *B* site's electronegativity increases, transition metal-oxygen bond covalency increases due to the decreased difference in electronegativity between the *B* cation and oxygen anion. Previous computational studies on similar perovskites concluded that oxide vacancy formation is enhanced by weaker *B*—O bonds in La*B*O_3 perovskites.[116] Therefore, the less electronegative metals would enhance oxygen vacancy formation under CLC conditions.

Interestingly, as electronegativity increases, the OSC starts to rise again after iron. The previous argument that the B—O bond strength diminishes oxide vacancy formation seems to be less important for this part of the trend. It has been widely accepted that the catalytic performance of metals follows the Sabatier's principle (interactions between the catalyst and interface needs to be "just right")[122] and the *d*-band model (the existence of correlation between interaction energy and *d*-band center in transition metal catalysts).[123] Nwosu *et al.* claims that mixed metal ions from 3*d* transition metal whose average electronegativities are equivalent to those of noble metals should show similar catalytic performance.[110, 124] The study of catalysts for hydrocarbon cracking shows that metals with similar electronegativities would therefore lead to similar catalytic effects.[124,125] Therefore, it could be that the *d*-band center is influenced by the deeper ionization potentials of the *B* metals (which factors into λ_B) takes over as a more important parameter than B—O bond strength.

Considering the superior catalytic performance of $Ba_{0.5}Sr_{0.5}Co_{0.8}Fe_{0.2}O_3$ in OER[113b], we also prepared this perovskite to validate the inverted volcano plot with no lanthanum/calcium in *A* site. As indicated in Figure 2a, the OSC of $Ba_{0.5}Sr_{0.5}Co_{0.8}Fe_{0.2}O_3$ fits reasonably well in the inverted volcano plot, indicating that this behavior is more universal and applies to other *A* site OC perovskites with 3*d* transition metals on the *B* site.

4.4 Conclusions and Outlook

Our study concludes that 3*d* transition metal *B* site electronegativity could be used as a powerful descriptor in the OSC of perovskites with CH_4 total combustion. We found an inverted volcano plot relationship for the lanthanum/calcium perovskite, and while the choice for the *A* site (either La or Ca) has a negligible effect on the OSC, the choice of the *B* site is more relevant towards the design of optimal OC's. We propose that the limiting impactor of OSC in the total combustion of CH_4 by perovskite oxides is C-H bond activation. We propose that the inverted volcano plot is attributed to two different reaction mechanisms between the activation of C-H bond in methane in the series. This approach may offer a heuristic approach towards choosing and evaluating perovskite OC's and possibly other energy related applications.

Chapter 5: Thermal Decomposition and Kinetics of Poly (Lactic Acid) Sacrificial Polymer Catalyzed by Metal Oxide Nanoparticles

5.1 Introduction

Poly Lactic Acid (PLA) is an environmentally friendly polymer produced from plants (mainly from starch and sugar) including corn, potatoes and sugar-beets, and has attracted attention for its biocompatibility, biodegradability, and thermoplastic processability.[50] It has been reported that the greenhouse gas emission rate of PLA is approximately 1600 kg CO_2/metric ton, while that of polypropylene (PE), polystyrene (PS), polyethylene terephthalate (PET), and nylon are 1850, 2740, 4140, and 7150 kg CO_2/metric ton, respectively.[126] Further, PLA's low temperature of thermal degradation with minimal solid residue (gasified lactide) has made it an attractive candidate as a sacrificial component in polymer fabrication.[56, 126-127]

PLA is also one of the two major plastics explored as 3D printing inks (the other being Acrylonitrile Butadiene Styrene (ABS)) because of its thermoplastic properties.[52] Although ABS is currently the dominant 3D printing polymer, PLA offers the advantage of bio-compatibility. As a sacrificial component, PLA can be 3D printed to create complex-shaped molds[54, 128]. For example, White *et al.*[54] have

fabricated PLA as spheres (0D), fibers (1D), sheets (2D), and 3D printed sacrificial materials, leaving behind the reverse replica. Pitet *et al.*[129] have explored PLA as a sacrificial component in copolymers to create porous membranes for battery separators utilizing the fact that its decomposition temperature is about 200 K lower than thermally stable polymers such as polyimide (PI), epoxies, Poly(vinylidene fluoride-hexafluoropropylene) (PVDF-HFP), *etc.* The decomposition of neat PLA occurs above ~550K, which can lead to the thermal instability of other polymer blends in practical applications during prolonged heat treatment[54]. Therefore, alkali earth metal oxides[56], rare metal (scandium (III) triflates (CF_3SO_3-))[60], and tin-containing compounds[54, 61, 128b] were studied as catalysts for PLA thermal decomposition. Moore *et al.*[54, 128a] added Sn-based reactants to lower the decomposition temperature by 90 K to effectively remove sacrificial PLA at a lower temperature while avoiding thermal damage to the epoxy mold. It was found that the same amount of SnO_x additive works even better than tin (II) octoate to further reduce the total decomposition time at the same temperature.[54] Mori *et al.* reported similar results using Sn-based compounds and recognized that these catalysts could enhance the breakage of ester bonds in the polymer backbone, thus promoting the fragmented polymer ends to experience chain backbiting and transesterification reactions before further depolymerization.[61] Almost all of the previous studies used a high loading of more than 5 wt% catalyst.[54, 56, 60-61, 128-129]

Addition of catalysts into PLA is usually achieved by surface treatment (including impregnation or solvent swelling)[128a], solvent evaporation casting[54], or vane extruding.[130] Dong *et al.*[128a] utilized solvent swelling to immobilize metal ions

(tin (II) octoate solution) into PLA fibers. Later, Moore *et al.* used solvent evaporation to imbed SnO_x into PLA, further decreasing the decomposition temperature.[54] Solvent evaporation casting of PLA with specific viscosity was utilized by Guo *et al*. in a proposed 3D printing ink drying technique.[131] Zhang *et al.* utilized melt blending with a vane extruder with heating to get mono-dispersed PLA/TiO_2 nanocomposites.[130]

It is widely known that controlling the removal process of the sacrificial materials is extremely difficult, requiring carefully designed thermal conditions and perfect timing to fully eliminate the sacrificial material at minimal cost, while also keeping the host material undamaged.[132] Therefore, catalysts are added to increase the decomposition temperature difference between the sacrificial materials and host materials to maintain the integrity of the host polymer.[54, 56, 60-61, 128-129] Usually the removal time for even nano-scale channels are hours to days and are highly non-linear relative to different heating conditions, which makes the control process hard to predict.[54, 128a, 132a] The severity of this problem increases as larger and more complex geometries are required with the rapid development of 3D printing using such sacrificial materials.[131] MOs have not been studied extensively as catalysts for PLA, especially at small loadings (< 5%).

In this work, we employed 1 wt% MOs loading to study the catalytic effects of MOs. Bi_2O_3, CuO and Fe_2O_3 are synthesized by spray pyrolysis[76, 80, 133] and then uniformly embedded into PLA matrix using solvent evaporation casting. XRD and SEM are performed to verify the additives' crystallinity and homogenous dispersion in the PLA matrix. The thermal properties of PLA/MOs composites relative to neat

PLA are measured by TGA (Thermogravimetric Analyzer), DSC (Differential Scanning Calorimeter), and MCC (Microscale Combustion Calorimeter) to examine the MOs catalytic effect on the PLA's thermal degradation process and overall combustion heat. Thermal degradation simulations are performed to fit the experimental TGA curve with a number of first order chemical pyrolysis reaction models using a one dimensional pyrolysis model (-ThermaKin[134] running under thermally thin mode). This kinetic fitting work is preformed to reproduce the TGA data, which provides kinetic fundamentals to potentially further predict and control the removing process time and temperatures of PLA/MOs for different geometries or length scales in various heating environments in the future.

5.2 Experimental Approach

5.2.1 Catalyst synthesis

All metal oxide additives are in-house synthesized by aerosol spray pyrolysis.[76, 80, 133] The spray pyrolysis system consists of an atomizer (to produce aerosol droplets), a silica-gel diffusion drier (to remove solvent), an isothermal furnace (to decompose precursor droplets), and a stainless steel sample collector with 0.4 μm DTTP Millipore filter (to collect nanoparticles). The aerosol droplets of precursor solution are generated using a collision-type nebulizer with an initial droplet diameter of approximately 1μm, which is then desiccated by passing through the silica-gel diffusion dryer. The dehydrated aerosol precursors then decompose into the solid metal oxide particles in the tube furnace set at 873 K for Fe_2O_3 and CuO, or 1050^{o}C for Bi_2O_3, with a residence time of about 1 s. Particles exiting the aerosol reactor are then collected on a 0.4 μm pore size DTTP Millipore filter with 10%-20% porosity

(EMD Millipore). The precursors used for the Bi_2O_3, Fe_2O_3, and CuO are $Bi(NO_3)_3 \cdot 5H_2O$, $Fe(NO_3)_3 \cdot 9H_2O$ and $Cu(NO_3)_2 \cdot 3H_2O$ respectively, all from Sigma-Aldrich. A total precursor concentration of 0.200 M aqueous solution is used for MOs, and to dissolve $Bi(NO_3)_3 \cdot 5H_2O$, 1:5 concentrated nitric acid and water mixture is used as the solvent. The aerosol spray pyrolysis is a droplet to droplet method. Lognormal poly-dispersed spherical solid particles are generated e.g. the Fe_2O_3 particles are spherical particles with a lognormal distribution peak at 84nm.[133]

5.2.2 Incorporation of nano-catalysts into PLA

PLA (Rejuven8 Plus Spartech) is obtained from Nature Works and used as received. The PLA sheets are 0.7 mm thick and cut into small pieces for solvent evaporation casting. 1.000 g PLA is first dissolved in 100.0 mL CH_2Cl_2 with magnetic stirring for 30 mins. Then 10.0 mg (1 wt%) MO is added to the solution and ultra-sonicated for 1 h. The solutions are then poured onto a watch glass and dried in a 323 K convection oven to for 12 h. Thin films of neat PLA (baseline reference) and PLA/MO composites are obtained after solvent evaporation. Small pieces of the as prepared thin films were then used for the thermal tests.

5.2.3 Material characterizations

Crystal structures of metal oxides are characterized by XRD with a Bruker Smart1000 using Cu Kα radiation. SEM results were obtained by Hitachi SU-70 SEM. For cross-sectional SEM images, samples are first fractured in liquid nitrogen and then sputter-coated with carbon. Nitrogen (N_2) adsorption-desorption isotherms and Brunauer–Emmett–Teller (BET) surface were measured at 77 K with a Micromeritics ASAP

2020 Porosimeter.

A Netzsch F3 Jupiter Simultaneous Thermal Analyzer (STA), employed in the thermal stability study, combines a TGA equipped with a 1 μg-resolution microbalance and DSC heat flow measurement with a steel furnace. Thus the STA can measure the TGA and DSC signals simultaneously during a single experiment. The PLA/MOs films were stored in a desiccator for 48 hours prior to testing, and then cut and pressed into Platinum-Rhodium crucibles with ventilation lids with a sample mass of 6-7 mg. The thermal decomposition experiments were performed at a heating rate of 10 K min^{-1} from 313 K to 873 K under 99.999% (UHP) N_2 at a flow rate of 50 $cm^3 \cdot min^{-1}$. A microscale combustion calorimeter (MCC) with 3 mg samples was used to measure the heat release rate and total heat of combustion. The MCC combines a condensed phase pyrolyzer and gas phase combustor. The samples are first decomposed in 80 cm^3 min^{-1} UHP N_2 flow, 60 K min^{-1} heating rate from 348 to 873 K inside the pyrolyzer, which is similar to the STA furnace, and then transferred to the combustor where the gaseous fuel (decomposition products) was burned at 1223 K to ensure complete combustion mixing with additional 20 $cm^3 \cdot min^{-1}$ O_2. The entire experimental measurement of HRR (Heat Release Rate) followed ASTM standard ASTM D 7309-07.[135] The heat release rate is measured based on Thornton's rule by measuring the O_2 consumption rate of combustion.[136]

5.3 Results and Discussion

5.3.1 Material textural properties

Figure 5.1 shows the SEM micrographs of spray pyrolysis synthesized Bi_2O_3, Fe_2O_3 and CuO nanoparticles, which are solid spherical particles with diameters from 50 nm to 1 μm following a log normal distribution with a peak (Fe_2O_3 at 84 nm[133], CuO at 86 nm and Bi_2O_3 at 87 nm, shown in Figure 5.2. Figure 5.3 shows BET surface area results: Fe_2O_3-13 m^2/g, CuO-23 m^2/g, Bi_2O_3-4 m^2/g), with Bi_2O_3 surface area being the lowest, indicating that surface area does not explain the superior catalytic activity of Bi_2O_3. The crystal structures of oxides are investigated from XRD shown in Figure 5.4. All peaks in Fe_2O_3 can be indexed to γ-Fe_2O_3 phase (JCPDS card No.: 39-1346); Bi_2O_3 with JCPDS card No.: 27-0050, while CuO peaks corresponds to tenorite with JCPDS card No.: 48-1548.

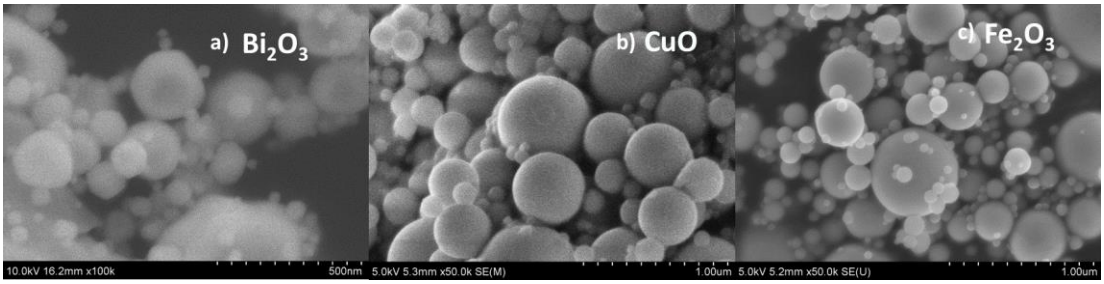

Figure 5.1. SEM of nanoparticles a) Bi_2O_3, b) CuO, c) Fe_2O_3, prepared from spray pyrolysis.

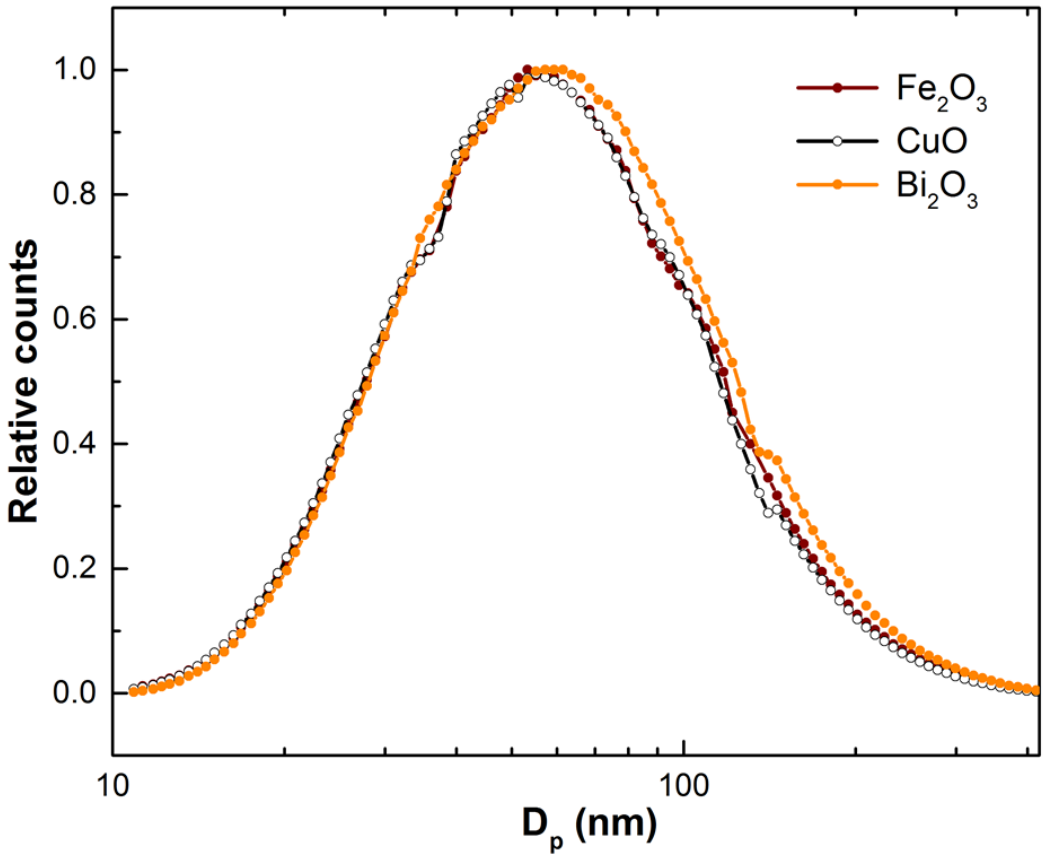

Figure 5.2. Particle-size distributions of Fe_2O_3, CuO, Bi_2O_3 as-synthesized by spray pyrolysis measured using a differential mobility analyzer (DMA) coupled with a condensation particle counter (CPC).

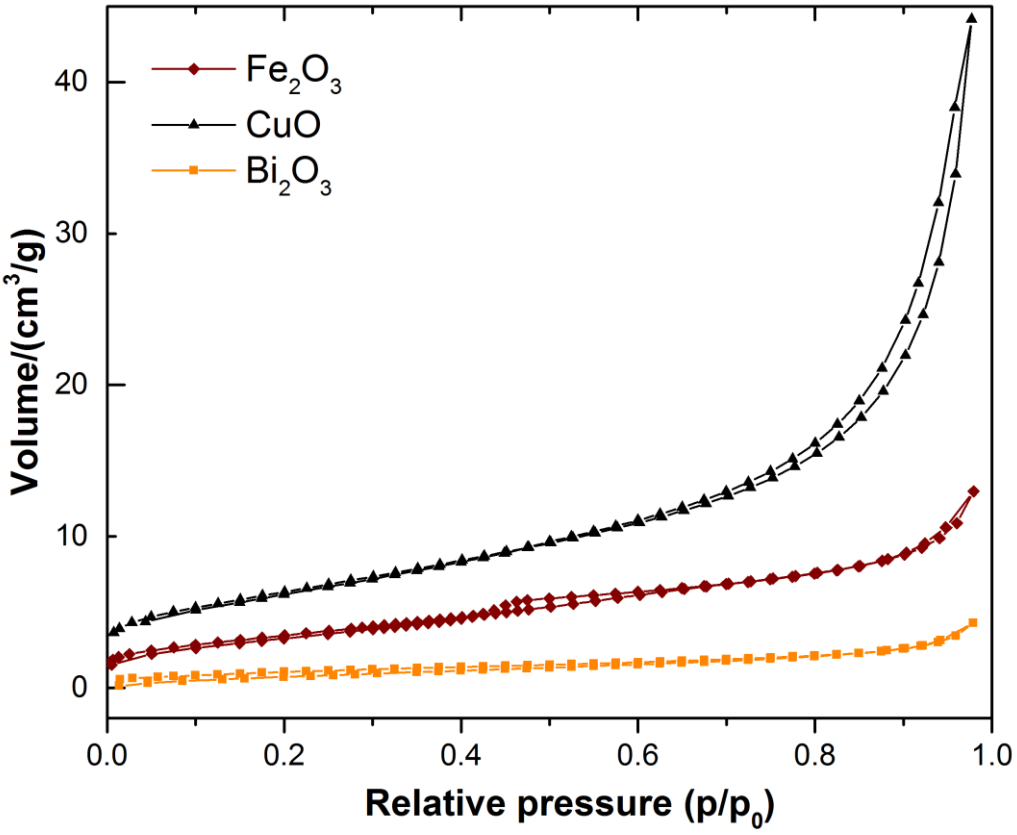

Figure 5.3. N_2 adsorption/desorption isotherms of Fe_2O_3, CuO, Bi_2O_3.

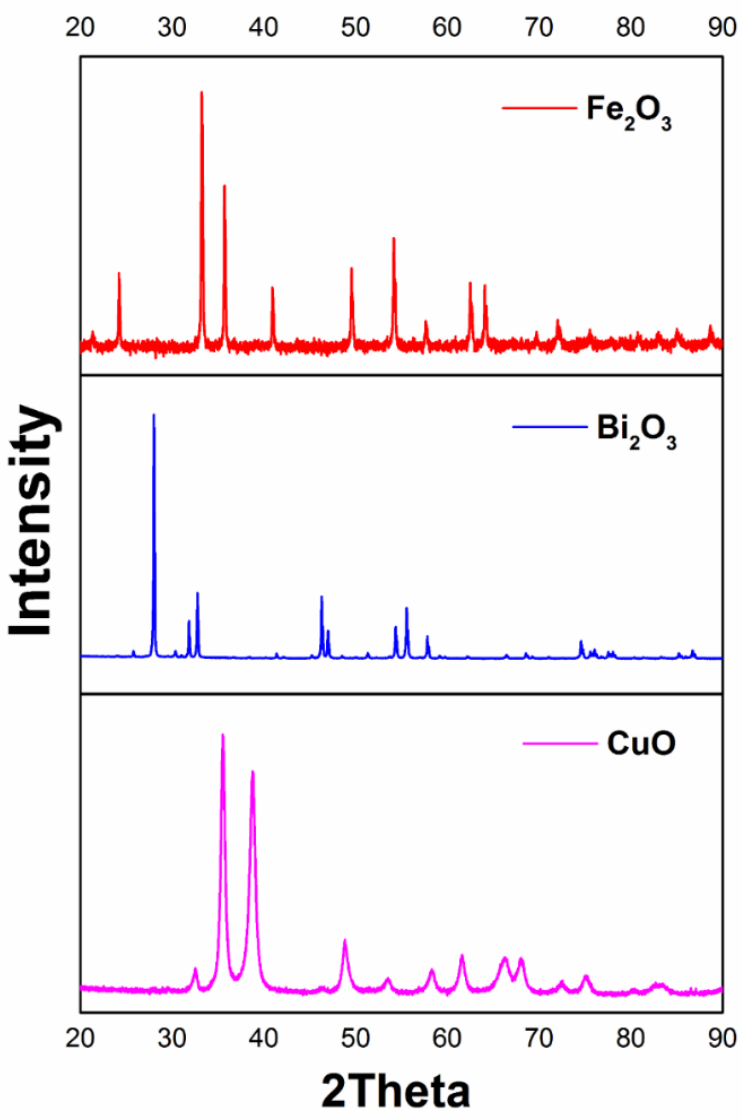

Figure 5.4. XRD of nanoparticles-Bi_2O_3, Fe_2O_3, CuO from spray pyrolysis.

It is widely known that the dispersion of nanoparticles in polymer will greatly influence the both chemical and physical properties of the PLA/MO composites. Homogeneous dispersion of MO nanoparticles will affect the thermal and mechanical behaviors of PLA, such as wettability, UV transmittance, strength and ductility, elasticity, viscosity, antibacterial property.[130]

Cross-sectional SEM images are taken to check the dispersion of MOs in the composites. PLA/MOs are first fractured in liquid nitrogen and then broken off for cross-sectional images. Figure 5.5a) and 5.5b) show neat PLA cross-sectional image without particles, while Figure 5.5c) and 5.5d) are PLA/Fe_2O_3, PLA/CuO films images. It is clear from these images that all nanoparticles are well dispersed in the PLA films. Figure 5.4 shows the cross-sectional PLA/Bi_2O_3 structure, and it is clear that spherical Bi_2O_3 are uniformly dispersed in PLA and un-aggregated. The film is about 50 μm thick, indicated by low magnification image of Figure 5.6a) and Figure 5.6b). Moreover, Figure 5.6c) and 5.6d) give a closer view of the cross-sections, all showing that particles are coated and/or connected by PLA while separated from other nanoparticles.

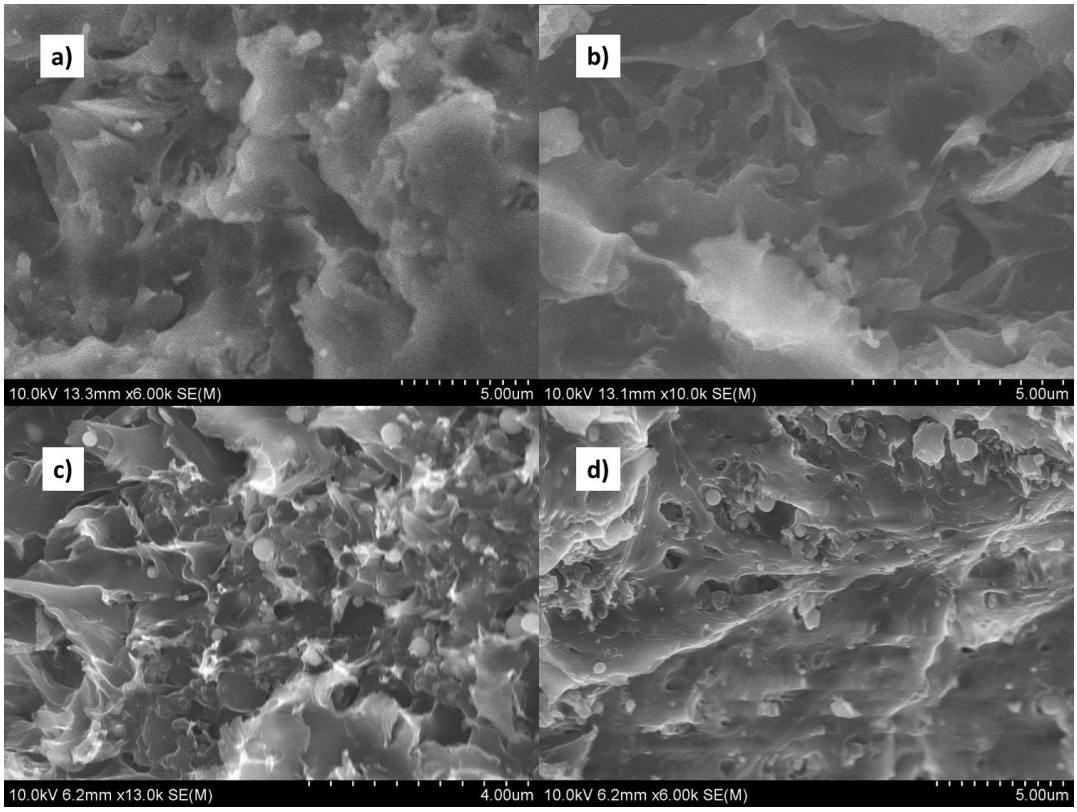

Figure 5.5. SEM of cross-sectioned a) and b) PLA, c) PLA/Fe_2O_3, d) PLA/CuO films.

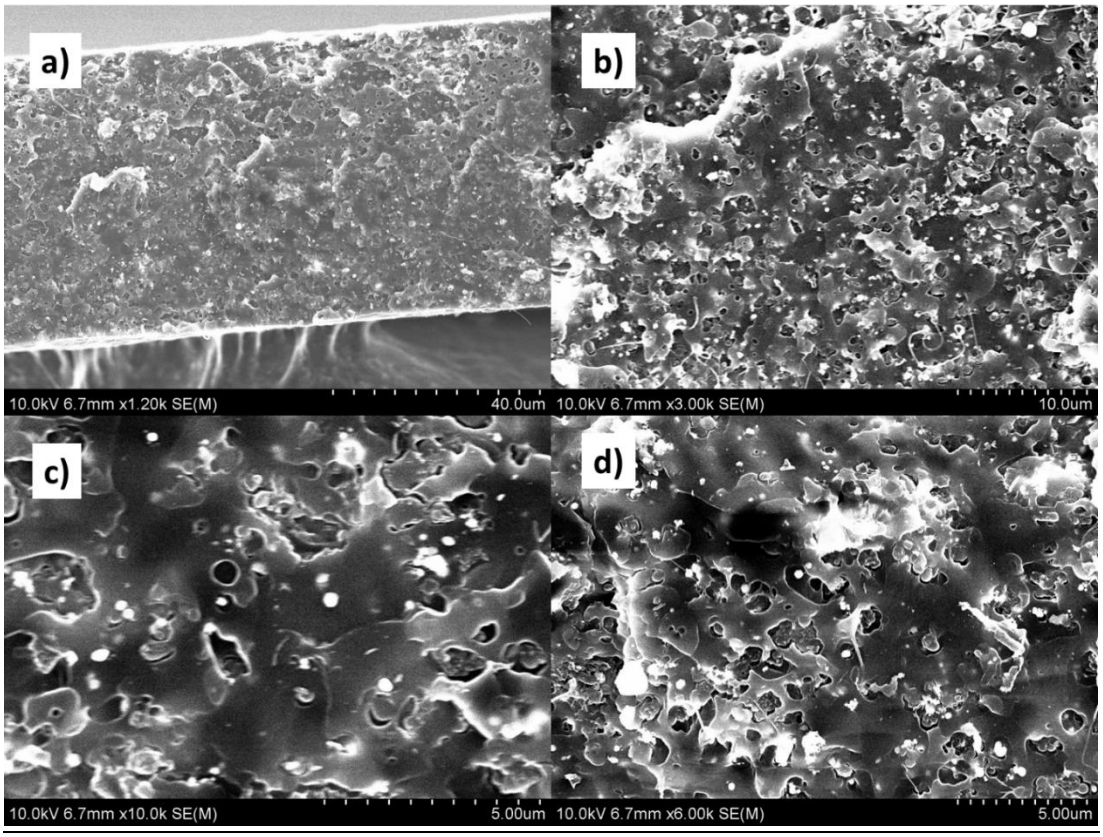

Figure 5.6. SEM of cross-sectioned PLA/Bi_2O_3 film.

5.3.2 Thermal tests and kinetic analysis

Figure 5.7 shows the TGA data of thermal decomposition mass loss under N_2 inert atmosphere. It is clear that the various types of MO additives affect the thermal stabilities of PLA/MOs differently, which can also be clearly seen in Figure 5.8 from Derivative Thermogravimetry (DTG) experimental curves (dotted lines). Specifically, the onset thermal degradation temperature for neat PLA as a reference is approximately $T_{5\%} \approx 580$ K. For PLA/Bi_2O_3, this temperature is 75 K lower ($T_{5\%} \approx$ 505 K), while the effect of Fe_2O_3 is about 30 K decrease ($T_{5\%} \approx 550$ K) compared to neat PLA; CuO shows no noticeable effect. The thermal degradation temperatures at maximum weight loss (T_{max}), are 536 K (614 K for the second peak), 573 K, 634 K and 635 K for PLA/Bi_2O_3, PLA/ Fe_2O_3, PLA/CuO and neat PLA respectively. These results show that the catalytic properties trend as: Bi_2O_3>Fe_2O_3>CuO. While the DSC signals reveal notable differences at the stage of decomposition, the addition of MOs does not significantly affect the melting point ~ 425 K or the heat of melting (as seen in DSC Figure 5.9). The heats of melting (the first peak integrals) are within 4% difference of their mean.

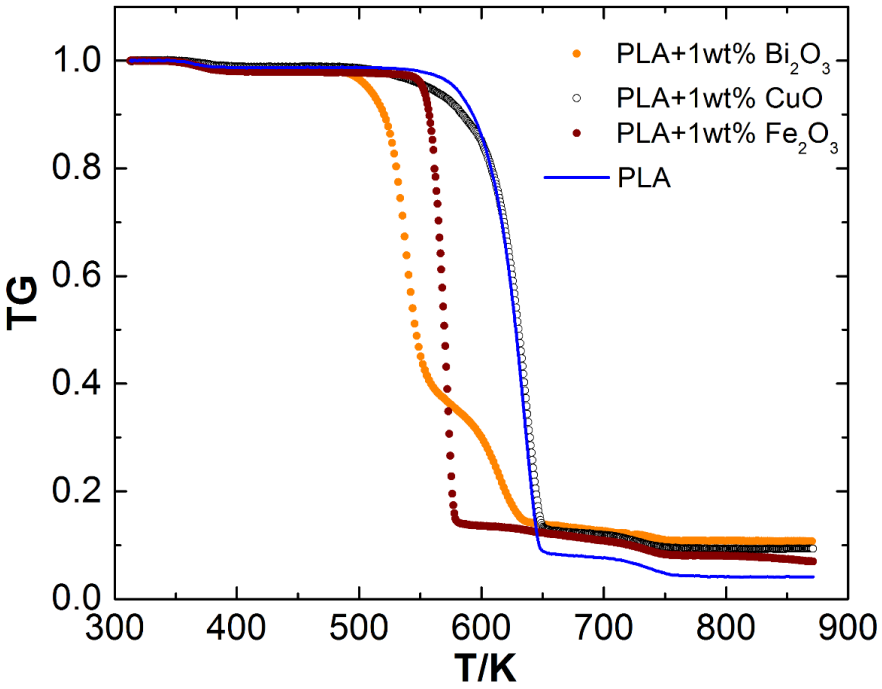

Figure 5.7. TGA of PLA and PLA/MOs.

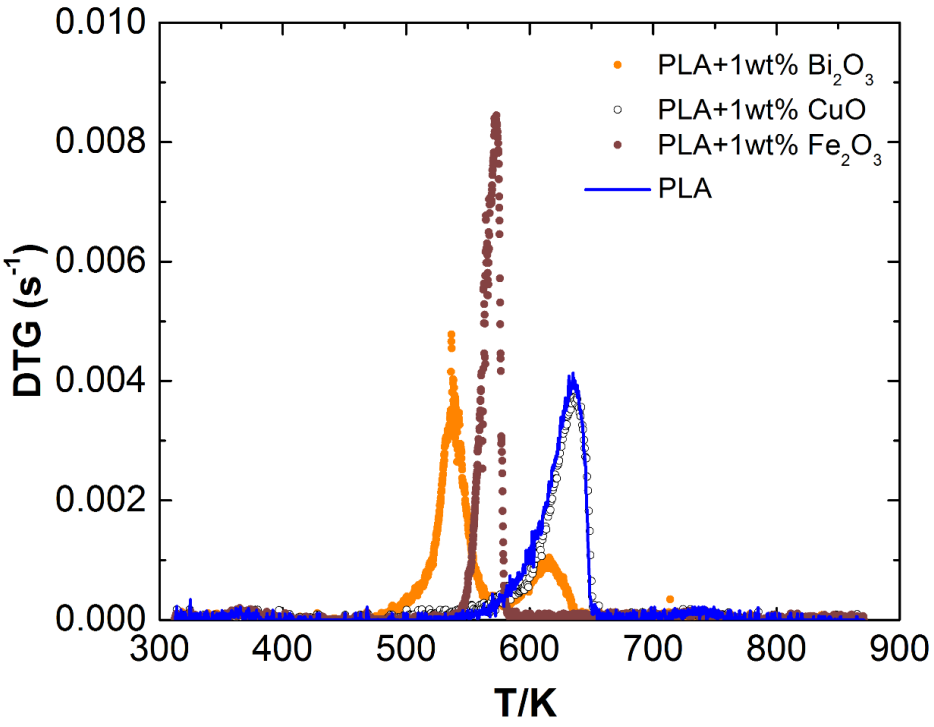

Figure 5.8. DTG plots of PLA and PLA/MOs.

To better evaluate the decomposition kinetics at various heating conditions and scales, which are necessary as fundamentals to predict the catalytic effects of the MOs on the PLA decomposition, we have extracted phenomenological rate parameters using a numerical pyrolysis software - ThermaKin.[134] ThermaKin solves the mass and energy conservation equations numerically for one or two-dimensional objects exposed to external (convective and/or radiative) heat. In this study, we use the thermally thin mode to simulate the thermal degradation processes inside the STA furnace. The material of the object (sample) is described by multiple components, which may interact chemically and physically. The neat PLA and PLA/MOs kinetics were characterized using the methodology reported in our recent publications.[137] This methodology has been successfully applied to reproduce TGA and DSC signals of 15 non-charring and charring polymers.[23,24] The resulting kinetic parameters were also shown to predict gasification or burning rates of these polymers at a wide range of thermal conditions.[137-138] The results of this characterization is shown in Figure 5.10.

In the previous study, neat PLA was tested using STA and the kinetics of its decomposition was modeled using two consecutive first order reactions.[137] One more reaction was employed to describe melting (T_{melt} = 425 K). This was done to use a minimum number of parameters to describe the entire time-resolved TGA and DSC curves. The kinetics of those reactions are parameterized with Arrhenius parameters (A_x, E_x represent decomposition reaction x; while A_m, E_m represent the melting) listed in Table 5.1. The value of the θ_x is calculated by the instantaneous mass (at the end stage of the reaction x) over its initial mass. Note that the θ_x, obtained directly from the TGA experiments, corresponds to the remaining condensed phase residue yielded

in the reaction x. Those parameters are initially estimated using simple analytical expressions[139] and then changed in small increments following the rules summarized in the previous studies until agreements with the experiment is reached (based on preset coefficient of determination and visual comparison). Each model reaction corresponds to tens or, perhaps, hundreds of elementary chemical processes operating within the same range of temperatures.

The MOs do not affect the phase transition as evident from DSC curves in Figure 5.9 (enlarged temperature range in the left corner). The kinetic parameters describing the melting were reported previously[137]. For all the PLA composites, MOs are found to affect the thermal degradation process significantly, which is apparent in both the TGA and DSC measurements. The impact of MOs on the kinetics of decomposition is quantified through changes in the parameters of the first (major) reaction. The kinetic parameters are summarized in Table 5.1. With the exception of PLA/Bi_2O_3, the decomposition of all composites can be described by two consecutive reactions. The kinetics of the second reaction remain unaffected by the addition of MOs. In the case of PLA/Bi_2O_3, the thermal decomposition process consists of three consecutive reactions reflecting a more complex DTG signal. It has been widely concluded that the thermal decomposition of pure PLA is a one-stage reaction that involves the loss of ester groups in pure nitrogen and air,[7,11] consistent with our observations for neat PLA and PLA/CuO in this study. Other researchers have also observed multiple reaction steps with the addition of other catalysts[6], although little information on mechanism is available. Our speculation for the existing second peak is that part of the PLA remains unaffected by the catalytic Bi_2O_3 during the first

decomposition step, and it decomposes as neat PLA at a higher temperature to form the second peak. Further investigation is required to validate this hypothesis.

For all the materials, the solid lines in Figure 5.9 represent the numerical simulation results from the ThermaKin. All the simulation results fit the experimental data well and the calculated coefficients of determination of the experimental data and the fitted curves are all above 0.9.

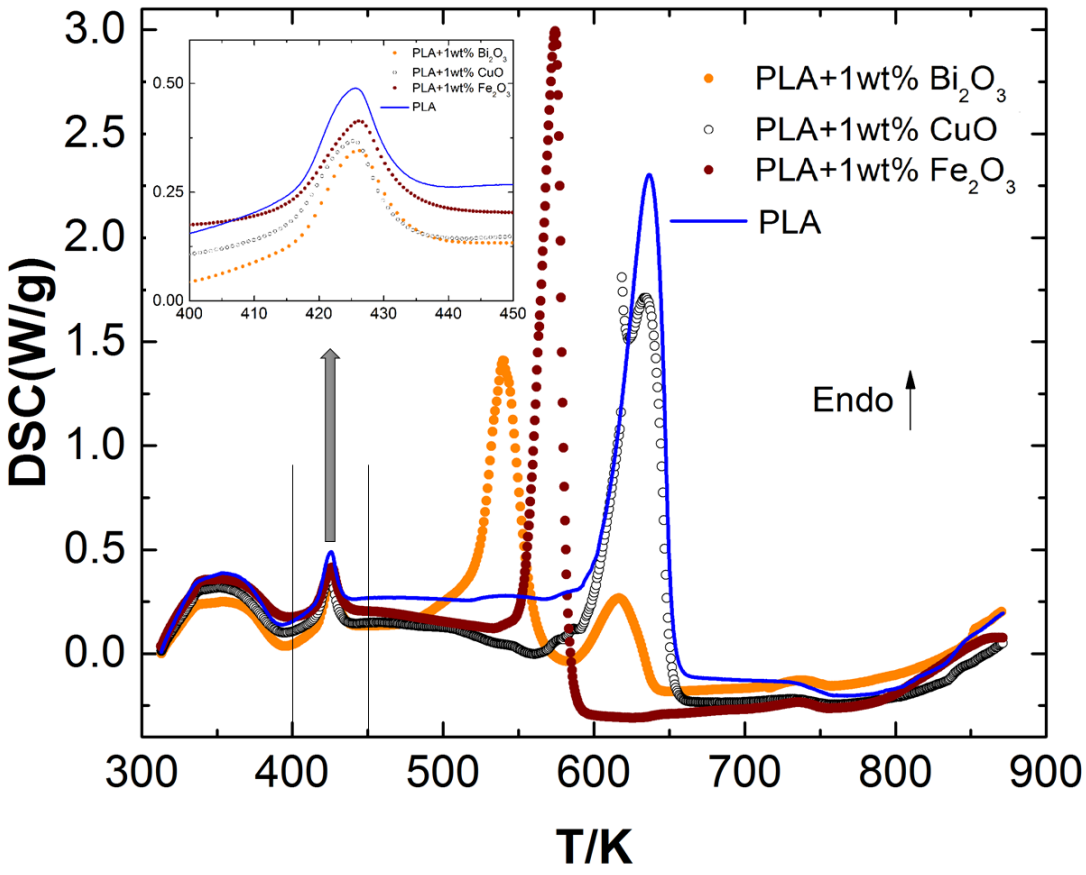

Figure 5.9. DSC test of PLA and PLA/MOs.

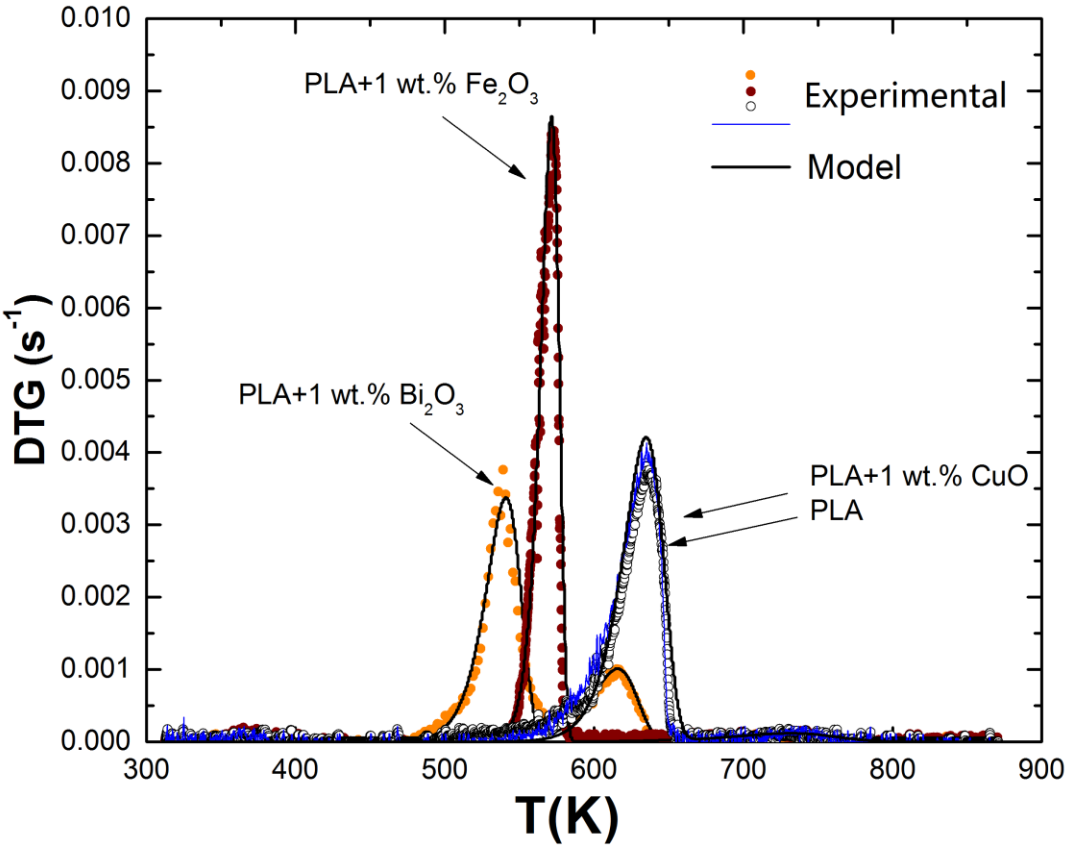

Figure 5.10. Experimental and simulated DTG of PLA & PLA/MO composites at 10 K min^{-1}.

Table 5.2 Kinetic parameters for PLA, PLA/Fe_2O_3, PLA/Bi_2O_3 and PLA/CuO.

Samples	A_1 (s^{-1})	E_1 (kJ mol^{-1})	θ_1	A_2 (s^{-1})	E_2 (kJ mol^{-1})	θ_2	A_3 (s^{-1})	E_3 (kJ mol^{-1})	θ_3	A_m (s^{-1})	E_m (kJ mol^{-1})
PLA	1.68E18	245	0.1	4.58E6	126	0.4	N/A	N/A	N/A	6.0E40	355
PLA+ Fe_2O_3	1.80E38	436	0.14	4.58E6	126	0.5	N/A	N/A	N/A	6.0E40	355
PLA+ Bi_2O_3	1.34E18	207	0.38	2.85E15	205.5	0.37	4.58E6	126	0.72	6.0E40	355
PLA+ CuO	1.68E18	245	0.1	4.58E6	126	0.4	N/A	N/A	N/A	6.0E40	355

The Heat Release Rate (HRR) is measured by MCC, as shown in the Figure 5.11. The heat release rate curves for all the PLA/MOs composites match the reaction peaks of TGA and DSC qualitatively but not quantitatively with respect to their peak temperatures. The corresponding heat release rate peaks in Figure 5.11 for all the samples shift to a higher temperature by approximately 27 ~ 28 K compared to the TGA and DSC results in Figures 5.7 & 5.9.

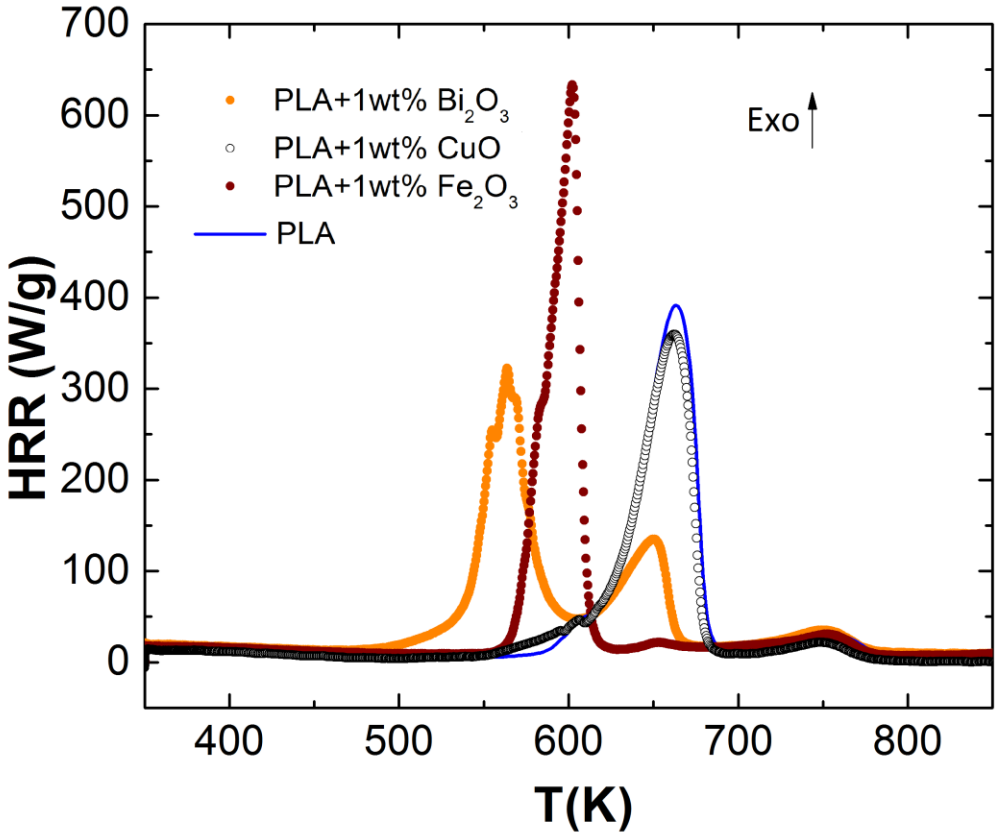

Figure 5.11. HRR of PLA, PLA/Fe_2O_3, PLA/Bi_2O_3 and PLA/CuO.

This temperature difference is caused by the relatively higher heating rate (60 K min^{-1}) utilized in the MCC compared to the heating rate (10 K min^{-1}) in the STA test. The integral of the heat release rate, which accounts for the heat of combustion of the gaseous decomposition products, is approximately equal for all tested samples yielding 19.5±0.8 kJ/g. Therefore, all of the these three types of 1wt% PLA/MOs affect the thermal degradation processes only in the condensed phase but have no effect on the heat of combustion.

5.4 Conclusions and Outlook

In this work, we offer a facile method to incorporate metal oxide additives and evaluate their catalytic effects on PLA thermal decomposition. More specifically, we have explored Bi_2O_3, CuO and Fe_2O_3 nanoparticles as catalysts for PLA thermal decomposition. Bi_2O_3 is shown to be a highly effective catalyst for PLA thermal decomposition. With only 1wt% loading, it lowered the onset decomposition temperature ($T_{5\%}$) by 75 K and the decomposition temperature at the maximum weight loss (T_{max}) by approximate 100 K, comparable to the most effective catalysts studied so far. The same amount of Fe_2O_3 and CuO nanoparticles have moderate and negligible effects on PLA thermal decomposition processes respectively. The overall catalytic effects of the three metal oxides trend as: $Bi_2O_3 > Fe_2O_3 > CuO \approx$ inert material.

The complete heats of combustion for the PLA/MOs composites have been measured by MCC, in which 1wt% MO additive catalyzes the thermal degradation processes differently in the condensed phase, and moreover, have negligible effect on the complete combustion heat in the gas phase as expected. PLA/MOs decomposition

was then quantatatively analysed to extract Arrhenious parameters for the decomposition kinetics, which offers possible explanations and predictions to evaluate thermal decompostion kinetics at other heating rate conditions.

Chapter 6: Conclusions and Future Work

6.1 Conclusions

This dissertation addressed the applications of nanostructured materials as oxygen carriers (OCs) and catalysts in poly lactic acid (PLA) thermal decomposition. The stability and cyclibility of metal oxides and supported metal oxides as OCs were evaluated in an isothermal fixed bed reactor at different temperatures for 50 cycles with methane as fuel, up to 15h while their structural, physical and chemical properties were identified using XRD, SEM, TEM, BET, XPS and Ar/H_2-TPR.

In chapter 2, alkaline (K-, Na-, and Cs-) doped iron oxide and alumina supported iron oxides were synthesized from on step aerosol spray pyrolysis and tested as OCs in fixed bed reactor with methane as fuel. We found that alkaline (K-, Na-) doped iron oxide and alumina supported iron oxides offers better stability and faster reduction kinetics as OCs in CLC reaction. The potassium doping promotes its reactivity most efficiently by binding the alumina support and iron oxide in the high temperature reactor and also offers less coking formation during reduction.

In chapter 3, silicalite-1 has been explored as the supporting material for iron oxide as OCs for the first time. Two kinds of structures, including Fe_2O_3@Si core-shell and Fe_2O_3@Si composite, are evaluated in the fixed bed reactor at both 1023 K and 1223 K. Both structures showed stable cyclic reactivity with no degradation in transferrable oxygen amount at both testing temperatures. At 1023 K, both OCs exhibited little morphological change after 15 h tests while at 1223 K, the core shell structure collapsed, with zeolite decomposed into SiO_2 and showed severe sintering;

the composite structure stayed both chemically and physically stable. Therefore, the composite structure worked as a better supporting material, offering both less coking and no sintering.

Perovskite oxides, chemical formulated as ABO_3, has been studied as novel OCs in CLC due to its thermal stability and faster reaction kinetics. In chapter 4, ten perovskite type OCs, $La_xCa_{1-x}B$(Cr-, Mn-, Fe-, Co-, Ni-)O_3 were synthesized from spray pyrolysis and tested with methane as fuel in the fixed bed reactor at 1023 K. It has been found that the oxygen storage capacity (OSC) has negligible change with changing A site from Ca to La while there exists an inverted volcano shaped relationship between OSC and B site electronegativity. Thus 3*d* transition metal *B* site electronegativity could be used as a powerful descriptor in the OSC of perovskites with CH_4 total combustion thus could provide useful design rule in choosing perovskite type OCs in CLC and might also provide some design insight for other energy related applications of perovskites.

Also we explored Bi_2O_3, CuO and Fe_2O_3 nanoparticles synthesized from spray pyrolysis, as catalysts for PLA thermal decomposition in chapter 5. The overall catalytic effects of the three metal oxides trend as: Bi_2O_3 > Fe_2O_3 > CuO ≈ inert material. Bi_2O_3 is shown to be a highly effective catalyst for PLA thermal decomposition. With only 1wt% loading, it lowered the onset decomposition temperature ($T_{5\%}$) by 75 K and the decomposition temperature at the maximum weight loss (T_{max}) by approximate 100 K, comparable to the most effective catalysts studied so far. The same amount of Fe_2O_3 and CuO nanoparticles have moderate and negligible effects on PLA thermal decomposition processes respectively.

6.2 Future Work

6.2.1 Develop kinetic models for alkaline additives added OCs and zeolite supported OCs

Kinetic reaction models and mechanisms between metal oxides and fuel in CLC is an indispensable stage in order to design a CLC reactor. The main goal of kinetic study is to obtain the concentration change of a reactant or product as a function of time. TGA could be used as a useful tool for the kinetic study, providing the exact mass and heat change vs time. By changing the reaction temperature systematically, detailed reaction kinetics data (E_a & A) between metal oxides and fuel could be achieved.

6.2.2 Study the effectiveness of alkaline or alkaline earth ions' addition to Cu-, Mn-, Ni- based OCs.

In chapter 2, it has been validated that the addition of alkaline ions to Fe-based OCs could effectively improve its reaction rate and support stability, as well as reducing coking formation. Those benefits may be applicable to other type OCs, such as Cu-, Mn- and Ni- based ones.

6.2.3 Study the effectiveness of zeolite support to Cu-, Mn-, Ni- based OCs.

In chapter 3, zeolite was explored as an effective novel support for Fe_2O_3 OC. It is worth studying its working conditions to other type OCs, such as Cu-, Mn- and Ni-based

6.2.4 Extend the 3d electronegativity rule of transition metal to other energy related applications

In chapter 4, it has been shown that there exists an inverted volcano plot between 3d transition metal B site electronegativity and OSC of perovskite type OCs, which could provide useful insights in perovskite type OC selection. This rule may be applicable to other energy related applications of perovskites, such as chemical looping methane reforming/water splitting or energetic materials.

6.2.5 Study the catalytic effects of other aerosol synthesized metal oxides to bio-degradable polymers

In chapter 5, aerosol synthesized Bi_2O_3 was found to be a useful catalyst in thermal PLA decomposition, which could lower the on-set decomposition temperature by ~75 T. The developed study protocol could be applied to various metal oxides and polymers to study their catalytic thermal decompositions as well.

Chapter 7: References

1. Ehrlich, P. R.; Kareiva, P. M.; Daily, G. C., Securing natural capital and expanding equity to rescale civilization. *Nature* **2012,** *486* (7401), 68-73.

2. Aleklett, K.; Höök, M.; Jakobsson, K.; Lardelli, M.; Snowden, S.; Söderbergh, B., The Peak of the Oil Age – Analyzing the world oil production Reference Scenario in World Energy Outlook 2008. *Energ Policy* **2010,** *38* (3), 1398-1414.

3. *Annual Energy Outlook* 2016. US Energy Inf. Adm. **2016.**

4. NRC, N. R. C., *Advancing the Science of Climate Change*. The National Academies Press: Washington, DC, USA., **2010.**

5. Padurean, A.; Cormos, C.-C.; Agachi, P.-S., Pre-combustion carbon dioxide capture by gas–liquid absorption for Integrated Gasification Combined Cycle power plants. *Int J Greenh Gas Con* **2012,** *7*, 1-11.

6. Kanniche, M.; Gros-Bonnivard, R.; Jaud, P.; Valle-Marcos, J.; Amann, J.-M.; Bouallou, C., Pre-combustion, post-combustion and oxy-combustion in thermal power plant for CO2 capture. *Appl Therm Eng* **2010,** *30* (1), 53-62.

7. Fujimori, T.; Yamada, T., Realization of oxyfuel combustion for near zero emission power generation. *Proceedings of the Combustion Institute* **2013,** *34* (2), 2111-2130.

8. Ishida, M.; Zheng, D.; Akehata, T., Evaluation of a Chemical-Looping-Combustion Power-Generation System by Graphic Exergy Analysis. *Energy* **1987,** *12* (2), 147-154.

9. Programme, I. G. G. R. D., Barriers implementation CCS capacity constraints. **2012**.

10. Boles, M. A.; Ling, D.; Hyeon, T.; Talapin, D. V., The surface science of nanocrystals. *Nature materials* **2016,** *15* (2), 141-153.

11. Lai, S. L.; Guo, J. Y.; Petrova, V.; Ramanath, G.; Allen, L. H., Size-Dependent Melting Properties of Small Tin Particles: Nanocalorimetric Measurements. *Phys Rev Lett* **1996,** *77* (1), 99-102.

12. Schmidt, M.; Kusche, R.; von Issendorff, B.; Haberland, H., Irregular variations in the melting point of size-selected atomic clusters. *Nature* **1998,** *393* (6682), 238-240.

13. Pluis, B.; van der Gon, A. W. D.; Frenken, J. W. M.; van der Veen, J. F., Crystal-Face Dependence of Surface Melting. *Phys Rev Lett* **1987,** *59* (23), 2678-2681.

14. Wang, Z. L.; Petroski, J. M.; Green, T. C.; El-Sayed, M. A., Shape Transformation and Surface Melting of Cubic and Tetrahedral Platinum Nanocrystals. *The Journal of Physical Chemistry B* **1998,** *102* (32), 6145-6151.

15. Nanda, K. K.; Kruis, F. E.; Fissan, H., Evaporation of Free PbS Nanoparticles: Evidence of the Kelvin Effect. *Phys Rev Lett* **2002,** *89* (25), 256103.

16. Arico, A. S.; Bruce, P.; Scrosati, B.; Tarascon, J.-M.; van Schalkwijk, W., Nanostructured materials for advanced energy conversion and storage devices. *Nature materials* **2005,** *4* (5), 366-377.

17. T.T. Kodas, M. J. H.-S., *Aerosol processing of materials*. 6th ed.; Wiley-VCH: New York, US, **1999.**

18. Zhang, S.-H.; Seifeld, J. H.; Flagan, R. C., Determination of Particle Vapor Pressures Using the Tandem Differential Mobility Analyzer. *Aerosol Science and Technology* **1993,** *19* (1), 3-14.

19. Teoh, W. Y.; Amal, R.; Madler, L., Flame spray pyrolysis: An enabling technology for nanoparticles design and fabrication. *Nanoscale* **2010,** *2* (8), 1324-1347.

20. Suh, W. H.; Jang, A. R.; Suh, Y. H.; Suslick, K. S., Porous, hollow, and ball-in-ball metal oxide microspheres: Preparation, endocytosis, and cytotoxicity. *Advanced materials* **2006,** *18* (14), 1832-+.

21. Skrabalak, S. E.; Suslick, K. S., Porous MoS2 synthesized by ultrasonic spray pyrolysis. *Journal of the American Chemical Society* **2005,** *127* (28), 9990-9991.

22. Zhou, W. B.; DeLisio, J. B.; Li, X. Y.; Liu, L.; Zachariah, M. R., Persulfate salt as an oxidizer for biocidal energetic nano-thermites. *Journal of Materials Chemistry A* **2015,** *3* (22), 11838-11846.

23. Fortunato, M. E.; Rostam-Abadi, M.; Suslick, K. S., Nanostructured Carbons Prepared by Ultrasonic Spray Pyrolysis. *Chemistry of Materials* **2010,** *22* (5), 1610-1612.

24. Luo, S.; Zeng, L.; Fan, L. S., Chemical Looping Technology: Oxygen Carrier Characteristics. *Annual review of chemical and biomolecular engineering* **2015,** *6*, 53-75.

25. Chuang, S. Y.; Dennis, J. S.; Hayhurst, A. N.; Scott, S. A., Development and performance of Cu-based oxygen carriers for chemical-looping combustion. *Combustion and Flame* **2008,** *154* (1-2), 109-121.

26. Johansson, M.; Mattisson, T.; Lyngfelt, A.; Abad, A., Using continuous and pulse experiments to compare two promising nickel-based oxygen carriers for use in chemical-looping technologies. *Fuel* **2008,** *87* (6), 988-1001.

27. Bayham, S. C.; Kim, H. R.; Wang, D. W.; Tong, A.; Zeng, L.; McGiveron, O.; Kathe, M. V.; Chung, E.; Wang, W.; Wang, A. N.; Majumder, A.; Fan, L. S., Iron-Based Coal Direct Chemical Looping Combustion Process: 200-h Continuous Operation of a 25-kW(th) Subpilot Unit. *Energy & Fuels* **2013,** *27* (3), 1347-1356.

28. Kim, H. R.; Wang, D. W.; Zeng, L.; Bayham, S.; Tong, A.; Chung, E.; Kathe, M. V.; Luo, S. W.; McGiveron, O.; Wang, A. N.; Sun, Z. C.; Chen, D.; Fan, L. S., Coal direct chemical looping combustion process: Design and operation of a 25-kW(th) sub-pilot unit. *Fuel* **2013,** *108*, 370-384.

29. Tong, A.; Sridhar, D.; Sun, Z. C.; Kim, H. R.; Zeng, L.; Wang, F.; Wang, D. W.; Kathe, M. V.; Luo, S. W.; Sun, Y. H.; Fan, L. S., Continuous high purity hydrogen generation from a syngas chemical looping 25 kW(th) sub-pilot unit with 100% carbon capture. *Fuel* **2013,** *103*, 495-505.

30. Kim, C. H.; Qi, G.; Dahlberg, K.; Li, W., Perovskites Rival Platinum Catalysts for Treating NO_x in Simulated Diesel Exhaust. *Science* **2010,** *327* (5973), 1624-1627.

31. Huang, Y. H.; Dass, R. I.; Xing, Z. L.; Goodenough, J. B., Double perovskites as anode materials for solid-oxide fuel cells. *Science* **2006,** *312* (5771), 254-7.

32. (a) Zhu, H.; Zhang, P.; Dai, S., Recent Advances of Lanthanum-Based Perovskite Oxides for Catalysis. *ACS Catalysis* **2015,** *5* (11), 6370-6385; (b) Sarshar, Z.; Kleitz, F.; Kaliaguine, S., Novel oxygen carriers for chemical looping

combustion: La1−xCexBO3 (B = Co, Mn) perovskites synthesized by reactive grinding and nanocasting. *Energy & Environmental Science* **2011,** *4* (10), 4258.

33. Abad, A.; García-Labiano, F.; Gayán, P.; de Diego, L. F.; Adánez, J., Redox kinetics of CaMg0.1Ti0.125Mn0.775O2.9−δ for Chemical Looping Combustion (CLC) and Chemical Looping with Oxygen Uncoupling (CLOU). *Chemical Engineering Journal* **2015,** *269*, 67-81.

34. Arjmand, M.; Keller, M.; Leion, H.; Mattisson, T.; Lyngfelt, A., Oxygen Release and Oxidation Rates of MgAl2O4-Supported CuO Oxygen Carrier for Chemical-Looping Combustion with Oxygen Uncoupling (CLOU). *Energy & Fuels* **2012,** *26* (11), 6528-6539.

35. Fan, L.-S.; Zeng, L.; Wang, W.; Luo, S., Chemical looping processes for CO2 capture and carbonaceous fuel conversion - prospect and opportunity. *Energy & Environmental Science* **2012,** *5* (6), 7254-7280.

36. Zhang, Y. X.; Doroodchi, E.; Moghtaderi, B., Chemical looping combustion of ultra low concentration of methane with Fe2O3/Al2O3 and CuO/SiO2. *Applied Energy* **2014,** *113*, 1916-1923.

37. Li, F.; Luo, S.; Sun, Z.; Bao, X.; Fan, L.-S., Role of metal oxide support in redox reactions of iron oxide for chemical looping applications: experiments and density functional theory calculations. *Energy & Environmental Science* **2011,** *4* (9), 3661-3667.

38. Song, H.; Doroodchi, E.; Moghtaderi, B., Redox Characteristics of Fe–Ni/SiO2Bimetallic Oxygen Carriers in CO under Conditions Pertinent to Chemical Looping Combustion. *Energy & Fuels* **2012,** *26* (1), 75-84.

39. Mattisson, T.; Johansson, M.; Lyngfelt, A., Multicycle Reduction and Oxidation of Different Types of Iron Oxide ParticlesApplication to Chemical-Looping Combustion. *Energy & Fuels* **2004,** *18* (3), 628-637.

40. (a) Cho, P.; Mattisson, T.; Lyngfelt, A., Defluidization Conditions for a Fluidized Bed of Iron Oxide-, Nickel Oxide-, and Manganese Oxide-Containing Oxygen Carriers for Chemical-Looping Combustion. *Industrial & Engineering Chemistry Research* **2006,** *45* (3), 968-977; (b) Rydén, M.; Cleverstam, E.; Johansson, M.; Lyngfelt, A.; Mattisson, T., Fe2O3 on Ce-, Ca-, or Mg-stabilized ZrO2 as oxygen carrier for chemical-looping combustion using NiO as additive. *AIChE Journal* **2010,** *56* (8), 2211-2220.

41. BOLT; #160; H., P.; HABRAKEN; #160; M., F. H. P.; GEUS; #160; W., J., *Formation of nickel, cobalt, copper, and iron aluminates from α- and γ-alumina-supported oxides : A comparative study*. Elsevier: Amsterdam, PAYS-BAS, 1998; Vol. 135.

42. Zafar, Q.; Mattisson, T.; Gevert, B., Integrated Hydrogen and Power Production with CO2 Capture Using Chemical-Looping ReformingRedox Reactivity of Particles of CuO, Mn2O3, NiO, and Fe2O3 Using SiO2 as a Support. *Industrial & Engineering Chemistry Research* **2005,** *44* (10), 3485-3496.

43. Zafar, Q.; Abad, A.; Mattisson, T.; Gevert, B.; Strand, M., Reduction and oxidation kinetics of Mn3O4/Mg–ZrO2 oxygen carrier particles for chemical-looping combustion. *Chemical Engineering Science* **2007,** *62* (23), 6556-6567.

44. Jin, H.; Okamoto, T.; Ishida, M., Development of a Novel Chemical-Looping Combustion: Synthesis of a Looping Material with a Double Metal Oxide of CoO−NiO. *Energy & Fuels* **1998,** *12* (6), 1272-1277.

45. Ishida, M.; Jin, H.; Okamoto, T., Kinetic Behavior of Solid Particle in Chemical-Looping Combustion: Suppressing Carbon Deposition in Reduction. *Energy & Fuels* **1998,** *12* (2), 223-229.

46. (a) Bhavsar, S.; Veser, G., Reducible Supports for Ni-based Oxygen Carriers in Chemical Looping Combustion. *Energy & Fuels* **2013,** *27* (4), 2073-2084; (b) Bhavsar, S.; Isenberg, N.; More, A.; Veser, G., Lanthana-doped ceria as active support for oxygen carriers in chemical looping combustion. *Applied Energy* **2016,** *168*, 236-247.

47. Hu, W.; Donat, F.; Scott, S. A.; Dennis, J. S., Kinetics of oxygen uncoupling of a copper based oxygen carrier. *Applied Energy* **2016,** *161*, 92-100.

48. Siriwardane, R.; Tian, H.; Miller, D.; Richards, G., Fluidized bed testing of commercially prepared MgO-promoted hematite and CuO–Fe2O3 mixed metal oxide oxygen carriers for methane and coal chemical looping combustion. *Applied Energy* **2015,** *157*, 348-357.

49. Berezina, N.; Martelli, S. M., CHAPTER 1 Bio-based Polymers and Materials. In *Renewable Resources for Biorefineries*, The Royal Society of Chemistry: 2014; pp 1-28.

50. Drumright, R. E.; Gruber, P. R.; Henton, D. E., Polylactic Acid Technology. *Advanced materials* **2000,** *12* (23), 1841-1846.

51. Gupta, B.; Revagade, N.; Hilborn, J., Poly(lactic acid) fiber: An overview. *Progress in Polymer Science* **2007,** *32* (4), 455-482.

52. Kreiger, M.; Pearce, J. M., Environmental Life Cycle Analysis of Distributed Three-Dimensional Printing and Conventional Manufacturing of Polymer Products. *ACS Sustainable Chemistry & Engineering* **2013,** *1* (12), 1511-1519.

53. Dong, H.; Esser-Kahn, A. P.; Thakre, P. R.; Patrick, J. F.; Sottos, N. R.; White, S. R.; Moore, J. S., Chemical treatment of poly(lactic acid) fibers to enhance the rate of thermal depolymerization. *ACS applied materials & interfaces* **2012,** *4* (2), 503-9.

54. Gergely, R. C. R.; Pety, S. J.; Krull, B. P.; Patrick, J. F.; Doan, T. Q.; Coppola, A. M.; Thakre, P. R.; Sottos, N. R.; Moore, J. S.; White, S. R., Multidimensional Vascularized Polymers using Degradable Sacrificial Templates. *Advanced Functional Materials* **2015,** *25* (7), 1043-1052.

55. Carrasco, F.; Pagès, P.; Gámez-Pérez, J.; Santana, O. O.; Maspoch, M. L., Kinetics of the thermal decomposition of processed poly(lactic acid). *Polymer Degradation and Stability* **2010,** *95* (12), 2508-2514.

56. Fan, Y.; Nishida, H.; Mori, T.; Shirai, Y.; Endo, T., Thermal degradation of poly(l-lactide): effect of alkali earth metal oxides for selective l,l-lactide formation. *Polymer* **2004,** *45* (4), 1197-1205.

57. Gonzalez, M. A.; Smith, R. L., A methodology to evaluate process sustainability. *Environmental Progress* **2003,** *22* (4), 269-276.

58. Zhang, H.; Yu, X.; Braun, P. V., Three-dimensional bicontinuous ultrafast-charge and -discharge bulk battery electrodes. *Nat Nano* **2011,** *6* (5), 277-281.

59. Arora, P.; Zhang, Z., Battery Separators. *Chemical reviews* **2004,** *104* (10), 4419-4462.

60. Coope, T. S.; Mayer, U. F. J.; Wass, D. F.; Trask, R. S.; Bond, I. P., Self-Healing of an Epoxy Resin Using Scandium(III) Triflate as a Catalytic Curing Agent. *Advanced Functional Materials* **2011,** *21* (24), 4624-4631.

61. Mori, T.; Nishida, H.; Shirai, Y.; Endo, T., Effects of chain end structures on pyrolysis of poly(l-lactic acid) containing tin atoms. *Polymer Degradation and Stability* **2004,** *84* (2), 243-251.

62. Zhang, H.; Huang, J.; Yang, L.; Chen, R.; Zou, W.; Lin, X.; Qu, J., Preparation, characterization and properties of PLA/TiO2nanocomposites based on a novel vane extruder. *RSC Adv.* **2015,** *5* (6), 4639-4647.

63. Richter, H. J.; Knoche, K. F., Reversibility of Combustion Processes. In *Efficiency and Costing*, AMERICAN CHEMICAL SOCIETY: 1983; Vol. 235, pp 71-85.

64. Bolhàr-Nordenkampf, J.; Pröll, T.; Kolbitsch, P.; Hofbauer, H., Comprehensive Modeling Tool for Chemical Looping Based Processes. *Chemical Engineering & Technology* **2009,** *32* (3), 410-417.

65. Lyngfelt, A.; Leckner, B.; Mattisson, T., A fluidized-bed combustion process with inherent CO2 separation; application of chemical-looping combustion. *Chemical Engineering Science* **2001,** *56* (10), 3101-3113.

66. Zafar, Q.; Mattisson, T.; Gevert, B., Redox Investigation of Some Oxides of Transition-State Metals Ni, Cu, Fe, and Mn Supported on SiO2 and MgAl2O4. *Energy & Fuels* **2006,** *20* (1), 34-44.

67. Yang, S.; Kim, K.; Baek, J.-I.; Kim, J.-W.; Lee, J. B.; Ryu, C. K.; Lee, G., Spinel Ni(Al,Fe)2O4 Solid Solution as an Oxygen Carrier for Chemical Looping Combustion. *Energy & Fuels* **2012,** *26* (7), 4617-4622.

68. Cho, P.; Mattisson, T.; Lyngfelt, A., Comparison of iron-, nickel-, copper- and manganese-based oxygen carriers for chemical-looping combustion. *Fuel* **2004,** *83* (9), 1215-1225.

69. Abad, A.; García-Labiano, F.; de Diego, L. F.; Gayán, P.; Adánez, J., Reduction Kinetics of Cu-, Ni-, and Fe-Based Oxygen Carriers Using Syngas (CO + H2) for Chemical-Looping Combustion. *Energy & Fuels* **2007,** *21* (4), 1843-1853.

70. Jerndal, E.; Mattisson, T.; Lyngfelt, A., Thermal Analysis of Chemical-Looping Combustion. *Chemical Engineering Research and Design* **2006,** *84* (9), 795-806.

71. Jiang, D. E.; Carter, E. A., Diffusion of interstitial hydrogen into and through bcc Fe from first principles. *Physical Review B* **2004,** *70* (6), 064102.

72. Huo, C.-F.; Wu, B.-S.; Gao, P.; Yang, Y.; Li, Y.-W.; Jiao, H., The Mechanism of Potassium Promoter: Enhancing the Stability of Active Surfaces. *Angewandte Chemie International Edition* **2011,** *50* (32), 7403-7406.

73. Figueiredo, R. T.; Santos, M. S.; Andrade, H. M. C.; Fierro, J. L. G., Effect of alkali cations on the CuZnOAl2O3 low temperature water gas-shift catalyst. *Catalysis Today* **2011,** *172* (1), 166-170.

74. Wu, J.; Saito, M., Improvement of Stability of a Cu/ZnO/Al2O3 Catalyst for the CO Shift Reaction. *Journal of Catalysis* **2000,** *195* (2), 420-422.

75. Mross, W. D., Alkali Doping in Heterogeneous Catalysis. *Catalysis Reviews* **1983,** *25* (4), 591-637.

76. Wu, C.; Sullivan, K.; Chowdhury, S.; Jian, G.; Zhou, L.; Zachariah, M. R., Encapsulation of Perchlorate Salts within Metal Oxides for Application as Nanoenergetic Oxidizers. *Advanced Functional Materials* **2012,** *22* (1), 78-85.

77. Noorman, S.; van Sint Annaland, M.; Kuipers, Packed Bed Reactor Technology for Chemical-Looping Combustion. *Industrial & Engineering Chemistry Research* **2007,** *46* (12), 4212-4220.

78. Noorman, S.; van Sint Annaland, M.; Kuipers, J. A. M., Experimental validation of packed bed chemical-looping combustion. *Chemical Engineering Science* **2010,** *65* (1), 92-97.

79. Corbella, B. M.; de Diego, L.; García-Labiano, F.; Adánez, J.; Palacios, J. M., Characterization and Performance in a Multicycle Test in a Fixed-Bed Reactor of Silica-Supported Copper Oxide as Oxygen Carrier for Chemical-Looping Combustion of Methane. *Energy & Fuels* **2006,** *20* (1), 148-154.

80. Jian, G.; Liu, L.; Zachariah, M. R., Facile Aerosol Route to Hollow CuO Spheres and its Superior Performance as an Oxidizer in Nanoenergetic Gas Generators. *Advanced Functional Materials* **2013,** *23* (10), 1341-1346.

81. Corbella, B. M.; De Diego, L.; García, F.; Adánez, J.; Palacios, J. M., The Performance in a Fixed Bed Reactor of Copper-Based Oxides on Titania as Oxygen Carriers for Chemical Looping Combustion of Methane. *Energy & Fuels* **2005,** *19* (2), 433-441.

82. Wang, H.; Jian, G.; Yan, S.; DeLisio, J. B.; Huang, C.; Zachariah, M. R., Electrospray Formation of Gelled Nano-Aluminum Microspheres with Superior Reactivity. *ACS applied materials & interfaces* **2013,** *5* (15), 6797-6801.

83. Khawam, A.; Flanagan, D. R., Solid-State Kinetic Models: Basics and Mathematical Fundamentals. *The Journal of Physical Chemistry B* **2006,** *110* (35), 17315-17328.

84. Tian, H.; Chaudhari, K.; Simonyi, T.; Poston, J.; Liu, T.; Sanders, T.; Veser, G.; Siriwardane, R., Chemical-looping Combustion of Coal-derived Synthesis Gas Over Copper Oxide Oxygen Carriers. *Energy & Fuels* **2008,** *22* (6), 3744-3755.

85. Gupta, P.; Li, F.; Velázquez-Vargas, L.; Sridhar, D.; Iyer, M.; Ramkumar, S.; Fan, L. S.; Fan, L.-S., Chemical Looping Particles. In *Chemical Looping Systems for Fossil Energy Conversions*, John Wiley & Sons, Inc.: 2010; pp 57-142.

86. Gu, H.; Shen, L.; Xiao, J.; Zhang, S.; Song, T., Chemical Looping Combustion of Biomass/Coal with Natural Iron Ore as Oxygen Carrier in a Continuous Reactor. *Energy & Fuels* **2011,** *25* (1), 446-455.

87. Yu, Z.; Li, C.; Fang, Y.; Huang, J.; Wang, Z., Reduction Rate Enhancements for Coal Direct Chemical Looping Combustion with an Iron Oxide Oxygen Carrier. *Energy & Fuels* **2012,** *26* (4), 2505-2511.

88. Lee, S. B.; Weiss, M.; Ertl, G., Adsorption of potassium on iron. *Surface Science* **1981,** *108* (2), 357-367.

89. Rohmund, F.; Falk, L. K. L.; Campbell, E. E. B., Iron catalyzed growth of carbon nanotubes. *AIP Conference Proceedings* **2000,** *544* (1), 234-237.

90. Bao, J.; Li, Z.; Cai, N., Promoting the Reduction Reactivity of Ilmenite by Introducing Foreign Ions in Chemical Looping Combustion. *Industrial & Engineering Chemistry Research* **2013,** *52* (18), 6119-6128.

91. Kotsionopoulos, N.; Bebelis, S., Electrochemical characterization of the Pt/ β′′ − Al2O3 system under conditions of in situ electrochemical modification of catalytic activity for propane combustion. *Journal of Applied Electrochemistry* **2010,** *40* (10), 1883-1891.

92. Padurean, A.; Cormos, C. C.; Agachi, P. S., Pre-combustion carbon dioxide capture by gas-liquid absorption for Integrated Gasification Combined Cycle power plants. *Int J Greenh Gas Con* **2012,** *7*, 1-11.

93. Adanez, J.; Abad, A.; Garcia-Labiano, F.; Gayan, P.; de Diego, L. F., Progress in Chemical-Looping Combustion and Reforming technologies. *Progress in Energy and Combustion Science* **2012,** *38* (2), 215-282.

94. Liu, L.; Zachariah, M. R., Enhanced Performance of Alkali Metal Doped Fe2O3and Fe2O3/Al2O3Composites As Oxygen Carrier Material in Chemical Looping Combustion. *Energy & Fuels* **2013,** *27* (8), 4977-4983.

95. Arjmand, M.; Azad, A.-M.; Leion, H.; Lyngfelt, A.; Mattisson, T., Prospects of Al2O3 and MgAl2O4-Supported CuO Oxygen Carriers in Chemical-Looping Combustion (CLC) and Chemical-Looping with Oxygen Uncoupling (CLOU). *Energy & Fuels* **2011,** *25* (11), 5493-5502.

96. García-Lario, A. L.; Martínez, I.; Murillo, R.; Grasa, G.; Fernández, J. R.; Abanades, J. C., Reduction Kinetics of a High Load Cu-based Pellet Suitable for

Ca/Cu Chemical Loops. *Industrial & Engineering Chemistry Research* **2013,** *52* (4), 1481-1490.

97. Chen, Y. G.; Galinsky, N.; Wang, Z. R.; Li, F. X., Investigation of perovskite supported composite oxides, for chemical looping conversion of syngas. *Fuel* **2014,** *134*, 521-530.

98. Kokotailo, G. T.; Lawton, S. L.; Olson, D. H.; Olson, D. H.; Meier, W. M., Structure of Synthetic Zeolite Zsm-5. *Nature* **1978,** *272* (5652), 437-438.

99. Flanigen, E. M.; Bennett, J. M.; Grose, R. W.; Cohen, J. P.; Patton, R. L.; Kirchner, R. M.; Smith, J. V., Silicalite, a New Hydrophobic Crystalline Silica Molecular-Sieve. *Nature* **1978,** *271* (5645), 512-516.

100. Huang, L. H.; Zhu, D.; Chen, Y. G.; Wu, C. L.; Sun, H. B.; Yang, H., Synthesis of monodisperse alpha-Fe2O3 deep-submicron spheres and its application in Li-ion batteries. *Materials Letters* **2012,** *74*, 37-39.

101. Khan, E. A.; Hu, E. P.; Lai, Z. P., Preparation of metal oxide/zeolite core-shell nanostructures. *Microporous and Mesoporous Materials* **2009,** *118* (1-3), 210-217.

102. Deng, Y.; Deng, C.; Qi, D.; Liu, C.; Liu, J.; Zhang, X.; Zhao, D., Synthesis of Core/Shell Colloidal Magnetic Zeolite Microspheres for the Immobilization of Trypsin. *Advanced materials* **2009,** *21* (13), 1377-1382.

103. Luisa Ojeda, M.; Marcos Esparza, J.; Campero, A.; Cordero, S.; Kornhauser, I.; Rojas, F., On comparing BJH and NLDFT pore-size distributions determined from N2 sorption on SBA-15 substrata. *Physical Chemistry Chemical Physics* **2003,** *5* (9), 1859-1866.

104. Wu, Y. Q.; Emdadi, L.; Oh, S. C.; Sakbodin, M.; Liu, D. X., Spatial distribution and catalytic performance of metal-acid sites in Mo/MFI catalysts with tunable meso-/microporous lamellar zeolite structures. *Journal of Catalysis* **2015,** *323*, 100-111.

105. Thommes, M.; Mitchell, S.; Pérez-Ramírez, J., Surface and Pore Structure Assessment of Hierarchical MFI Zeolites by Advanced Water and Argon Sorption Studies. *The Journal of Physical Chemistry C* **2012,** *116* (35), 18816-18823.

106. Nakai, K.; Sonoda, J.; Yoshida, M.; Hakuman, M.; Naono, H., High resolution adsorption isotherms of N-2 and Ar for nonporous silicas and MFI zeolites. *Adsorption* **2007,** *13* (3-4), 351-356.

107. Llewellyn, P. L.; Coulomb, J. P.; Grillet, Y.; Patarin, J.; Andre, G.; Rouquerol, J., Adsorption by MFI-type zeolites examined by isothermal microcalorimetry and neutron diffraction. 2. Nitrogen and carbon monoxide. *Langmuir : the ACS journal of surfaces and colloids* **1993,** *9* (7), 1852-1856.

108. Richter, H. J.; Knoche, K. F., Reversibility of Combustion Processes. *Acs Sym Ser* **1983,** *235*, 71-85.

109. Cheary, R. W.; Coelho, A., A fundamental parameters approach to X-ray line-profile fitting. *Journal of Applied Crystallography* **1992,** *25* (2), 109-121.

110. Nwosu, C., *J. Tech. Sci. Tech.* **2012,** *1*, 25-28.

111. Chin, Y.-H.; Buda, C.; Neurock, M.; Iglesia, E., Reactivity of Chemisorbed Oxygen Atoms and Their Catalytic Consequences during CH4–O2 Catalysis on Supported Pt Clusters. *Journal of the American Chemical Society* **2011,** *133* (40), 15958-15978.

112. Pauling, L., *Nature of the Chemical bond*. Cornell University Press: 1960.

113. (a) Bockris, J. O.; Otagawa, T., The Electrocatalysis of Oxygen Evolution on Perovskites. *J Electrochem Soc* **1984,** *131* (2), 290-302; (b) Suntivich, J.; May, K. J.; Gasteiger, H. A.; Goodenough, J. B.; Shao-Horn, Y., A perovskite oxide optimized for oxygen evolution catalysis from molecular orbital principles. *Science* **2011,** *334* (6061), 1383-5.

114. Vojvodic, A.; Norskov, J. K., Chemistry. Optimizing perovskites for the water-splitting reaction. *Science* **2011,** *334* (6061), 1355-6.

115. Hong, W. T.; Risch, M.; Stoerzinger, K. A.; Grimaud, A.; Suntivich, J.; Shao-Horn, Y., Toward the rational design of non-precious transition metal oxides for oxygen electrocatalysis. *Energy Environ. Sci.* **2015,** *8* (5), 1404-1427.

116. Munoz-Garcia, A. B.; Ritzmann, A. M.; Pavone, M.; Keith, J. A.; Carter, E. A., Oxygen transport in perovskite-type solid oxide fuel cell materials: insights from quantum mechanics. *Accounts of chemical research* **2014,** *47* (11), 3340-8.

117. Imanieh, M. H.; Rad, M. H.; Nadarajah, A.; González-Platas, J.; Rivera-López, F.; Martín, I. R., Novel perovskite ceramics for chemical looping combustion application. *Journal of CO2 Utilization* **2016,** *13*, 95-104.

118. Dai, X. P.; Li, R. J.; Yu, C. C.; Hao, Z. P., Unsteady-State Direct Partial Oxidation of Methane to Synthesis Gas in a Fixed-Bed Reactor Using AFeO3 (A = La, Nd, Eu) Perovskite-Type Oxides as Oxygen Storage. *The Journal of Physical Chemistry B* **2006,** *110* (45), 22525-22531.

119. Curnan, M. T.; Kitchin, J. R., Effects of Concentration, Crystal Structure, Magnetism, and Electronic Structure Method on First-Principles Oxygen Vacancy

Formation Energy Trends in Perovskites. *The Journal of Physical Chemistry C* **2014,** *118* (49), 28776-28790.

120. Carter, S.; Selcuk, A.; Chater, R. J.; Kajda, J.; Kilner, J. A.; Steele, B. C. H., Oxygen transport in selected nonstoichiometric perovskite-structure oxides. *Solid State Ionics* **1992,** *53*, 597-605.

121. Ponce, S.; Peña, M. A.; Fierro, J. L. G., Surface properties and catalytic performance in methane combustion of Sr-substituted lanthanum manganites. *Applied Catalysis B: Environmental* **2000,** *24* (3–4), 193-205.

122. Deutschmann, O.; Knözinger, H.; Kochloefl, K.; Turekin, T., Ullmann's Encyclopedia of Industrial Chemistry. Wiley-VCH Verlag: 2009.

123. Norskov, J. K.; Bligaard, T.; Rossmeisl, J.; Christensen, C. H., Towards the computational design of solid catalysts. *Nat Chem* **2009,** *1* (1), 37-46.

124. Plummer, M. A., Cracking process catalyst selection based on cation electronegativity. Google Patents: 1985.

125. Al Alwan, B.; Salley, S. O.; Ng, K. Y. S., Hydrocracking of DDGS corn oil over transition metal carbides supported on Al-SBA-15: Effect of fractional sum of metal electronegativities. *Applied Catalysis A: General* **2014,** *485*, 58-66.

126. Fan, Y.; Nishida, H.; Shirai, Y.; Tokiwa, Y.; Endo, T., Thermal degradation behaviour of poly(lactic acid) stereocomplex. *Polymer Degradation and Stability* **2004,** *86* (2), 197-208.

127. Gottschalk, C.; Frey, H., Hyperbranched Polylactide Copolymers. *Macromolecules* **2006,** *39* (5), 1719-1723.

128. (a) Dong, H.; Esser-Kahn, A. P.; Thakre, P. R.; Patrick, J. F.; Sottos, N. R.; White, S. R.; Moore, J. S., Chemical Treatment of Poly(lactic acid) Fibers to Enhance the Rate of Thermal Depolymerization. *ACS Applied Materials & Interfaces* **2012,** *4* (2), 503-509; (b) Carrasco, F.; Pagès, P.; Gámez-Pérez, J.; Santana, O. O.; Maspoch, M. L., Processing of poly(lactic acid): Characterization of chemical structure, thermal stability and mechanical properties. *Polymer Degradation and Stability* **2010,** *95* (2), 116-125.

129. Pitet, L. M.; Amendt, M. A.; Hillmyer, M. A., Nanoporous Linear Polyethylene from a Block Polymer Precursor. *J Am Chem Soc* **2010,** *132* (24), 8230-8231.

130. Zhang, H.; Huang, J.; Yang, L.; Chen, R.; Zou, W.; Lin, X.; Qu, J., Preparation, characterization and properties of PLA/TiO2 nanocomposites based on a novel vane extruder. *RSC Advances* **2015,** *5* (6), 4639-4647.

131. (a) Guo, S.-Z.; Gosselin, F.; Guerin, N.; Lanouette, A.-M.; Heuzey, M.-C.; Therriault, D., Solvent-Cast Three-Dimensional Printing of Multifunctional Microsystems. *Small* **2013,** *9* (24), 4118-4122; (b) Guo, S.-z.; Yang, X.; Heuzey, M.-C.; Therriault, D., 3D printing of a multifunctional nanocomposite helical liquid sensor. *Nanoscale* **2015,** *7* (15), 6451-6456.

132. (a) Reed, H. A.; White, C. E.; Rao, V.; Ann, S.; Allen, B.; Henderson, C. L.; Kohl, P. A., Fabrication of microchannels using polycarbonates as sacrificial materials. *J. Micromech. Microeng.* **2001,** *11* (6), 733-737; (b) Metz, S.; Jiguet, S.; Bertsch, A.; Renaud, P., Polyimide and SU-8 microfluidic devices manufactured by

heat-depolymerizable sacrificial material technique. *Lab on a Chip* **2004,** *4* (2), 114-120.

133. Liu, L.; Zachariah, M. R., Enhanced Performance of Alkali Metal Doped Fe2O3 and Fe2O3/Al2O3 Composites As Oxygen Carrier Material in Chemical Looping Combustion. *Energy & Fuels* **2013,** *27* (8), 4977-4983.

134. Stoliarov, S. I.; Lyon, R. E. *Thermo-Kinetic Model of Burning*; Federal Aviation Administration Technical Note: 2008.

135. ASTM(D7309-13) *Standard Test Method for Determining Flammability Characteristics of Plastics and Other Solid Materials Using Microscale Combustion Calorimetry*; 7309; 2013.

136. Thornton, W., The relation of oxygen to the heat of combustion of organic compounds. Philos. Mag. J. Sci., 1917, 33, 196-203 *Philosophical Magazine and J. of Science* **1917,** *33*, 196-203.

137. Li, J.; Stoliarov, S. I., Measurement of kinetics and thermodynamics of the thermal degradation for non-charring polymers. *Combustion and Flame* **2013,** *160* (7), 1287-1297.

138. (a) Li, J.; Gong, J.; Stoliarov, S. I., Gasification Experiments for Pyrolysis Model Parameterization and Validation. *Int J Heat Mass Tran* **2014,** *77*, 738-744; (b) Li, J.; Stoliarov, S. I., Measurement of kinetics and thermodynamics of the thermal degradation for charring polymers *Polymer Degradation and Stability* **2014,** *106*, 2-15; (c) Li, J.; Gong, J.; Stoliarov, S. I., Development of pyrolysis models for charring polymers. *Polymer Degradation and Stability* **2015,** *115* (0), 138-152.

139. Lyon, R. E.; N.Walters, R.; Stoliarov, S. I., A Thermal Analysis Method for Measuring Polymer Flammability. *Journal of ASTM International* **2006,** *3* (4), 1-18.